Acta Universitatis Sapientiae

Electrical and Mechanical Engineering

Volume 4, 2012

Sapientia Hungarian University of Transylvania
Scientia Publishing House

Antal Bege
(1962 – 2012)

Our colleague, friend, editor-in-chief of Acta Universitatis Sapientiae, associate professor Antal Bege passed away unexpectedly on March 22, 2012. He was only 49.

After finishing his studies in Mathematics at Babeş-Bolyai University in Cluj he became a teacher in his former school in Miercurea Ciuc. After the regime change in 1989 he joined the Faculty of Mathematics and Computer Science, at Babeş-Bolyai University. He worked there for almost two decades, then went over to Sapientia Hungarian University of Transylvania, Department of Mathematics and Informatics in Târgu-Mureş in 2008. This is where he became
the head of the department and the editor-in-chief of the academic journal Acta Universitatis Sapientiae. Naturally, he did his best in all these qualities.

Among his research interests we can mention Number Theory (arithmetical functions), Nonlinear Analysis and Discrete Mathematics. He published 13 textbooks and monographs both in Hungarian and Romanian, as well as a lot of scientific papers.

He was extremely evenhanded person, appreciated by all his colleagues and students, a man of poise and an eternal stayer. With a terrible feeling of pain and loss, we say goodbye to our friend. We shall treasure his memory.

Editorial Board

Contents

Acta Universitatis Sapientiae
Electrical and Mechanical Engineering, 4 (2012) 5-32

Cluster Formation in Wireless Mesh Networks

Dezső GÁBOS, Mihály VARGA

Communications Department,
Faculty of Electronics, Telecommunications and Information Technology,
Technical University of Cluj-Napoca,
e-mail: dezsogabos@gmail.com, Mihaly.Varga@com.utcluj.ro

Manuscript received November 1, 2013; revised January 13, 2014.

Abstract: Cluster formation in wireless mesh networks simplifies the maintenance of the entire network and allows the usage of decentralized routing algorithms. The defining factors in choosing the routing algorithm is the type of the network (MANET or WSN) and the node density. This paper consists of the description of a simulation platform for cluster formation in cooperative networks, which permits analysis and evaluation of different routing algorithms in such networks. The generic cluster formation algorithm was implemented in such a way, that each node has information only on neighbouring nodes. A couple of simple algorithms are presented which may be applied to the generated clusters (routing and data processing) to demonstrate the simulation capabilities offered by this platform. These algorithms include: maximum flow minimum cut of Ford Fulkerson combined with Dijkstra's routing algorithm.

Keywords: Ford Fulkerson, graph theory, wireless mesh networks

1. Introduction

Communications are evolving more and more in the direction of ad-hoc networks. The reason why these networks are gaining ground is because they do not require a well-defined infrastructure (base stations, routers, cables) and can be reconfigured at any time, adding or eliminating terminals or nodes (sensors, user terminals). A wireless ad-hoc network consists of a collection of autonomous nodes or terminals which communicate among themselves and form multi-hop radio networks maintaining connection in a decentralized manner. These types of networks are commonly used in areas where the fixed infrastructure has been destroyed or it is missing [1]. For example, a class of

students has to interact during a lecture, friends or business partners meet at an airport and need to exchange files, or an intervention team has to create connection with the outside of the affected area. In these situations a collection of mobile hosts with wireless network interfaces can create a provisory network without an existing infrastructure or centralized administration. This type of network is called an ad-hoc network [2].

Ad-hoc networks are based on ideas like reconfigurability, self-organization, dynamics, omnipresence and most importantly are centred around the needs of the user [3]. These are the main characteristics of next generation communications. An amazing development has taken place in the domain of wireless sensor networks, personal networks, wireless mesh networks, multi-hop communications and their integration in cellular systems. A multi-hop, multi-cluster system requires the capability to dynamically adapt to constant changes in the network. With the cluster formation algorithm the mobile nodes are divided in groups called clusters. The nodes in a certain cluster can be a gateway, simple nodes or the root of the cluster (called cluster head). Cluster heads (CH) are responsible for coordination of operations in the cluster, forming of new clusters and topology maintenance. Furthermore they have the responsibility of parting resources between members of a cluster.

In these types of networks the reconfiguration of the cluster heads is a necessity. The algorithm should not change the cluster configuration frequently. The most important advantages of these systems are: the scattered usage of applications, the possibility of routing optimization, efficient treatment of mobility, a better usage of bandwidth, aggregation of topology based information and minimization of necessary storage for information [3].

In a wireless ad-hoc network each node has the capability of forwarding messages from other nodes in the network. The route to the destination is determined by the connectivity of the whole system. The main characteristics of an ad-hoc network are: minimal configuration requirements and fast implementation. To maintain connections between nodes, each and every node has to be a router in itself. Each node functions both as a host and a router, and the control over the topology of the system are distributed between them. The topology of the network becomes dynamic because the connections between the nodes vary due to the addition and elimination of nodes in the system and due to their mobile nature. This is why the necessity of new routing protocols appeared. The two main types of ad-hoc networks are Mobile ad-hoc networks (MANET) [4] and wireless sensor networks (WSN) [5].

These systems need to possess the capability of self-organization on the physical layer. In the absence of a fixed infrastructure, a fully functional network can be achieved only through the possibility of cooperation between the nodes [6]. The topology changes are random, the connections between the

nodes have variable available bandwidths, so the need for decentralized routing algorithms appeared [7]. The discovery of the new topology and the delivery of data packets becomes the nodes' responsibility. In fixed networks the main algorithm is based on the cost function (shortest path), but this cannot be implemented in ad-hoc networks. The main problems are: free space pathloss and fading, interference, power consumption, topology changes [8]. The network is able to counter these effects by adaptive routing [9].

Each node or mobile device is equipped with a transmitter and a receiver, so without a set of rules the topology becomes arbitrary. A packet can arrive to the destination directly or through other intermediary nodes, which forward the packet. The decisions when building the topology and self-discovery mechanisms are key elements for a well-functioning ad-hoc network. The optimization and standardization cannot be restricted to a single layer [10] [11].

This paper approaches the problem of routing and cluster formation in wireless ad-hoc networks, by studying hierarchical structures, and well known cluster formations. Cluster formation is a method for constructing and maintaining hierarchical structures in a mobile ad-hoc network. The main parameters are: connectivity, stability of connections, bandwidth (quality of the connection). In a network based on clusters, the nodes can form any hierarchical structure. The most important advantage of an approach based on cluster formation is the improvement of routing efficiency, scalability and the minimization of power consumption. The dynamic forming of clusters help reduce the complexity of the nodes, packet length and help the multi-path routing. Because the size of an ad-hoc network is unlimited, partitioning it in clusters makes it manageable.

2. Routing and cluster formation in wireless ad-hoc networks

Cluster forming transforms a physical network in a virtual network, which contains interconnected clusters, or groups of mobile nodes [12]. Even with the nodes being identical in their capabilities, some nodes can be chosen to form the backbone of the network. These nodes become gateways and *cluster heads* (CH). The cluster heads are the nodes which are responsible of routing the messages to all the nodes in their cluster [13]. The gateway nodes are the nodes at the extremities of the cluster, and usually communicate with the gateway nodes from other clusters. The backbone of the wireless network can be used for routing packets, broadcasting routing packets or both in the same time. Due to the mobility of the nodes this backbone needs the capability of being reconstructed fast, as the nodes enter or leave the coverage area of the CH.

Routing protocols are divided into two categories based on how and when routes are discovered, but both find the shortest path to the destination.

Proactive routing protocols are table-driven protocols, they always maintain current up-to-date routing information by sending control messages periodically between the hosts which update their routing tables. When there are changes in the structure then the updates are propagated throughout the network. The proactive routing protocols use link-state routing algorithms which frequently flood the link information about its neighbours.

Other routing protocols are on-demand routing protocols, in other words reactive ones, which create routes when they are needed by the source host and these routes are maintained while they are needed. Such protocols use distance-vector routing algorithms [14], they have vectors containing information about the cost and the path to the destination. When nodes exchange vectors of information, each host modifies its own routing information when needed. The ad hoc routing protocols are usually classified as a pure proactive or a pure reactive protocol, but there are also hybrid protocols. This only concerns flat routing protocols, but there are also hierarchical and graphic position assisted routing protocols [15].

The main routing and cluster formation algorithm presented on literature are: CBLARHM (Cluster Based Location-Aware Routing Protocol for Large Scale Heterogeneous Mobile Ad-Hoc Networks), CBMPR (Cluster Based Multipoint Relay Protocol), CRAM (Cluster head based Routing Algorithm), SCRAM (Scenario Based Routing Algorithm), LEACH (Low Energy Adaptive Clustering Hierarchy), HEED (Hybrid, energy efficient, distributed clustering), PEGASIS (Power efficient gathering in sensor information systems), ERA (Energy Residue Aware), PEBECS (Partition Energy Balanced and Efficient Clustering Scheme), RCSDN (Distributed Balanced Routing Algorithm with Optimized Distribution), and many more.

There are two important mechanisms used in the *Cluster Based Location-Aware Routing Protocol for Large Scale Heterogeneous Mobile Ad-Hoc Network* (CBLARHM) [16] to improve the MANET performance. Node clustering is an efficient technique to mitigate the topology changes in MANET. It stabilizes the end-to-end communication paths and improves the networks scalability so that the routing overhead does not become tremendous in large scale MANET. Another key challenge is controlling the total number of nodes involved in a routing establishment process so as to reduce the total routing overhead of the MANET. The mechanism used is to use the geographical location information provided by global positioning systems (GPS) to assist in routing. Instead of searching the route in the entire network blindly, position-based routing protocol uses the location information of mobile nodes to confine the route searching space into a smaller estimated range. Simulation results have shown that CBLARHM outperforms other protocols significantly in route setup time, routing overhead and collision, and simultaneously maintains a low

average end-to-end delay, as well as low route discovery frequency [16].

The *Optimized Link State Routing* (OLSR) [17] protocol is a proactive routing protocol. The key concept used in the protocol is that of multipoint relays (MPRs). MPRs refer to selected routers that can forward broadcast messages during the flooding process. The idea of multipoint relays is to minimize the flooding of broadcast packets in the network by reducing duplicate retransmissions in the same region. Although OLSR provides a path from source to destination, it is not necessarily the shortest path, because every route involves forwarding through a MPR node. A further disadvantage is that OLSR also has routing delays and bandwidth overhead at the MPR nodes as they act as localized forwarding routers.

The Dynamic Source Routing (DSR) [15] protocol is a reactive routing protocol for MANETs. The key feature of DSR is the use of source routing, which means the sender knows the complete hop-by-hop route to the destination. A complete list of intermediate nodes to the destination kept in the header of each data packet. Scalability and poor performance in high mobility and heavy traffic loads are disadvantage of DSR, because DSR relies on blind broadcasts to discover routes. AODV [17] is essentially a combination of both DSR and DSDV. It borrows the basic on-demand mechanism of Route Discovery and Route Maintenance from DSR, plus the use of hop-by-hop routing, sequence numbers, and periodic beacons from DSDV. AODV is loop-free due to the destination sequence numbers associated with routes. It creates routes only on-demand, which greatly reduces the periodic control message overhead associated with proactive routing protocols. Similar to DSR, poor scalability is a disadvantage of AODV. Bypass-AODV, an extension of AODV, uses a specific strategy of cross-layer MAC-interaction to identify mobility-related link breaks, and then setup a bypass between the broken link end nodes via an alternative node. [18]

Low Energy Adaptive Clustering Hierarchy (LEACH) [19] is a hierarchical protocol in which most nodes transmit to cluster heads, and the cluster heads aggregate and compress the data and forward it to the base station(sink). Each node uses a stochastic algorithm at each round to determine whether it will become a cluster head in this round. LEACH assumes that each node has a radio powerful enough to directly reach the base station or the nearest cluster head, but that using this radio at full power all the time would waste energy.

Nodes that have been cluster heads cannot become cluster heads again for P rounds, where P is the desired percentage of cluster heads. Thereafter, each node has a $1/P$ probability of becoming a cluster head in each round. At the end of each round, each node that is not a cluster head selects the closest cluster head and joins that cluster. The cluster head then creates a schedule for each node in its cluster to transmit its data.

All nodes that are not cluster heads only communicate with the cluster head in a TDMA fashion, according to the schedule created by the cluster head. They do so using the minimum energy needed to reach the cluster head, and only need to keep their radios on during their time slot.

Power efficient gathering in sensor information systems PEGASIS [21]- sensor webs consisting of nodes with limited battery power and wireless communications are deployed to collect useful information from the field. Gathering sensed information in an energy efficient manner is critical to operate the sensor network for a long period of time. In a data collection problem is defined where, in a round of communication, each sensor node has a packet to be sent to the distant base station. If each node transmits its sensed data directly to the base station then it will deplete its power quickly. The LEACH protocol presented in is an elegant solution where clusters are formed to fuse data before transmitting to the base station. By randomizing the cluster heads chosen to transmit to the base station, LEACH achieves a factor of 8 improvement compared to direct transmissions, as measured in terms of when nodes die. In PEGASIS, each node communicates only with a close neighbour and takes turns transmitting to the base station, thus reducing the amount of energy spent per round. Simulation results show that PEGASIS performs better than LEACH by about 100 to 300% when 1%, 20%, 50%, and 100% of nodes die for different network sizes and topologies [21].

These algorithms are mostly about choosing a cluster head (CH), which take care of the routing between the clusters. Most of them concentrate on the power management, and try to find a method to minimize the overhead, to reduce the power consumption, to prolong the life of a node, to extend the system duration by finding a balance in the node usage. In the case studied by us, we do not need these algorithms, because we assume that the nodes are connected to a power source, and power consumption is not a problem.

In this paper we consider that a cluster consist from the set of nodes which can communicate together without using an external communication channel, i.e. there exist at least one route between any two elements of the cluster with capacity higher than zero. The problem is finding a route, on which we can transmit with the highest transfer rate. We can find this, by applying the Maximum spanning tree algorithm, because our edges are defined by transfer rates. The novelty brought to this algorithm is the method of solving this graph theory problem in a decentralized way. Each and every node makes decisions based on the information known to it, and has no access to information about the whole system.

A. Ford Fulkerson algorithm

A commonly met question in networks is: "How much is the maximum data transfer rate between two nodes?" A good example would be the maximum number of phone calls between two cities, or the maximum number of cars that can travel between two cities. An infinite transfer rate is impossible, because the telephone lines or roads have a limited capacity. On the other hand, there are more routes on which you can arrive at your destination. Finding the maximum flow between two points means the analysis of all the routes between these two nodes [22]. When the system is a network, the edges represent the channels with limited capacity. To find the maximum flow, each edge needs to be used at maximum capacity. Another possible problem can be the asymmetry of these edges (difference in capacity between directions). In the following figures, it will illustrate the principle of this algorithm, step by step.

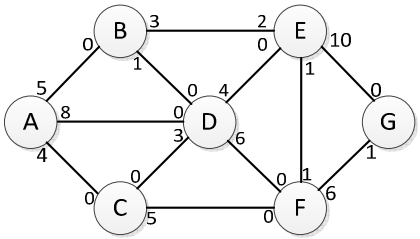

Figure 1: Undirected graph with asymmetric capacities.

Between points A and G there is a transfer rate of 4 on the A-D-E-G route, a transfer rate of 3 on the A-B-E-G route and a transfer rate of 4 on the A-C-F-G route. The bottleneck is the edge with the smallest transfer rate on a given route. This set of routes sum up to a total transfer rate of 11 from A to G, but this is not the maximum flow. There are unused edges between the two nodes. We need a better algorithm, to calculate the maximum flow, and we will implement it with the Ford Fulkerson method. The basic idea of this algorithm is the manipulation of the assigned data flows to the different routes from the source node to the destination. The main steps of the algorithm are:

1. Finding any of the possible routes from the source node to the destination, with a positive flow. If there are no more routes, the algorithm ends.

2. The determination of f, the maximum flow along this route, which equals the smallest edge capacity from the routes edges.

3. Decreasing all edge capacity values from the routes' edges with the value of *f*, on the direct route and adding it to the edge capacities on the inverse route.

4. Repeating from step 1.

At the end of the algorithm, the sum of the flows along the routes found at step 1 gives us the maximum flow between the source and destination.

B. Step by step implementation of the Ford Fulkerson algorithm

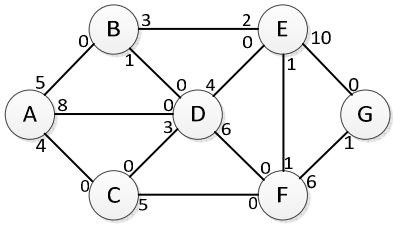

Figure 2: Original Graph.

The original graph contains nodes and edges; and we define a capacity on each edge. These capacities do not have to be symmetric. A good example would be a road between two cities. The number of car strips in one direction must not always be equal to the car strips in the other direction. This principle can also be applied with radio transmissions. The channel's characteristics in point A is not identical with the channel characteristics from point B. This way, we can define different capacities on the same edge in different directions.

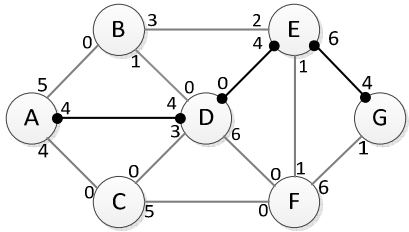

Figure 3: Graph illustrating the first route.

We chose the A-D-E-G route. The bottleneck will be the D-E edge, which has the capacity of 4. This capacity is subtracted from all edges on the direct route between A and G, and it is added to the inverse route. This way the capacity between A-D becomes 4 from 8, on D-E it becomes 0 from 4, and on E-G it becomes 6 from 10. On the inverse route, D-A becomes 4 from 0, E-D becomes 4 from 0 and G-E becomes 4 from 0.

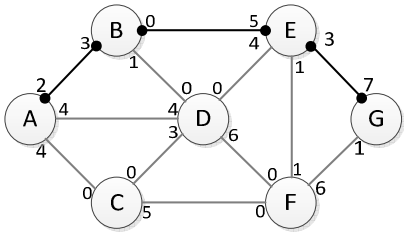

Figure 4: Graph illustrating the second route.

We chose the A-B-E-G route. The bottleneck is the B-E edge, with the capacity of 3. This capacity is subtracted on the direct route, so the A-B capacity becomes 2 from 5, the B-E capacity becomes 0 from 3 and the capacity of E-G edge becomes 3 from 6. On the inverse route G-E becomes 7 from 4, E-B becomes 5 from 2 and B-A becomes 3 from 0.

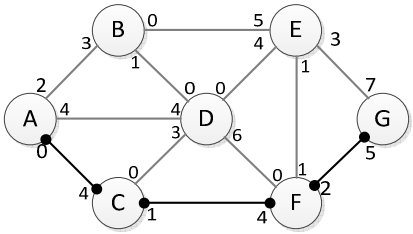

Figure 5: Graph illustrating the third route.

We chose the A-C-F-G route. The bottleneck is the A-C edge with the capacity of 4. On the direct route the A-C capacity becomes 0 from 4, the C-F capacity becomes 1 from 5, and between F-G the capacity becomes 2 from 6. On the inverse route C-A becomes 4 from 0, F-C becomes 4 from 0 and G-F becomes 5 from 1.

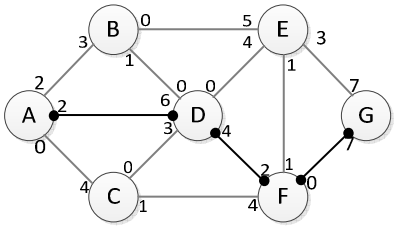

Figure 6: Graph illustrating the fourth route.

We chose the A-D-F-G path. The bottleneck is the F-G edge, with the capacity of 2. On the direct route A-D becomes 2 from 4, D-F becomes 4 from 6, and F-G becomes 0 from 2. On the inverse route the capacity of G-F becomes 7 from 5, F-D becomes 2 from 0 and D-A becomes 6 from 4.

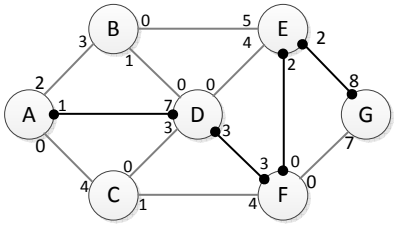

Figure 7: Graph illustrating the fifth route.

We chose the A-D-F-E-G route. The bottleneck is the F-E edge with the capacity of 1. On the direct route, A-D becomes 1 from 2, D-F becomes 3 from 4, F-E becomes 0 from 1, E-G becomes 2 from 3. On the inverse route G-E becomes 8 from 7, E-F becomes 2 from 1, F-D becomes 3 from 2, D-A becomes 7 from 6.

As we can see, we have no positive flows left between nodes A and G. The algorithm ends. After finishing the algorithm, the maximum flow between node A and node G will be the sum of the 5 flows on the 5 different routes. This way, the maximum flow becomes 4+3+4+2+1=14.

The question is, how much flow should there be on each edge, and in what direction? We find the answer looking at the difference between the initial capacity and final capacity. A positive difference shows us a flow in association with the direct route, a negative difference is ignored. We can observe the principle of flow conservation at a node. For example, the flows entering in node F equal the sum of the flows exiting node F, and equal to 7.

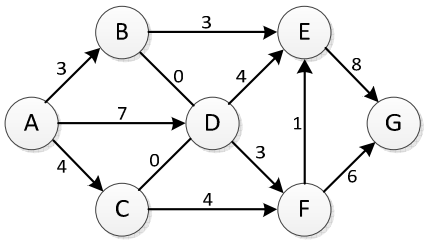

Figure 8: Final fluxes.

As we can see, it becomes harder and harder to find a positive flow, as the algorithm progresses, and the easily identifiable routes disappear.

This in fact is not a problem, because the next route can be found with algorithms like depth-first and breadth first. The remaining question is: why do we need to change the edge capacities on the inverse route? The answer is simple: the edge capacities on the inverse route can be seen as a convention for indicating a restorable flows if it is needed.

The problem of maximum flow is in direct association with the problem of minimum cut. A cut is a set of directional edges, which contains at least one edge from all routes between the source node and destination node. In other words, if the edges are eliminated, the flow from the source node to the destination node is completely cut off. The value of the cut is the sum of the edge capacities on the source-destination direction on the edges present in the cut. The problem is finding the cut in a way, that it has the smallest value from all possible values. An inefficient method would be finding the values of all cuts, and choosing the one with the smallest value. The number of these cuts is very large, so it is almost impossible to find all possibilities in a larger network,

even with nodes with a high computational power. A better idea is using the max-flow/min-cut theorem: for any network having only one source and one destination, the maximum flow from the source to the destination equals the value of minimum cut for all the cuts in the network.

A lot of applications use this theorem, including the search for congested nodes in traffic, in telecommunication networks, production lines and so on. Other algorithms with more complex implementations and better efficiency are the Goldberg algorithm and Edmons-Karp algorithm.

3. Simulation platform

The flow chart of the implemented simulation platform is presented in Fig. 9.

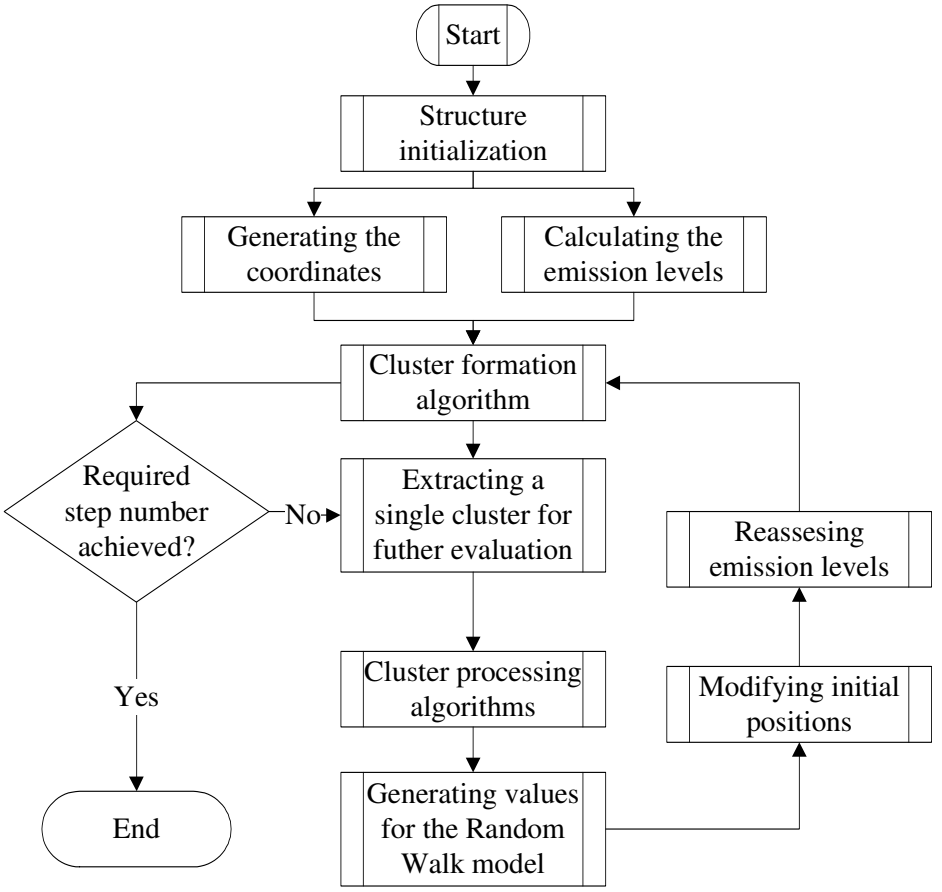

Figure 9: Flow chart for the simulation platform implementation.

The initialization of structures are based on an algorithm which generates random coordinates (x and y separately), and saves them in a structure with an equal length with the number of users. The coordinates are generated in accordance with the surface on which we plan to implement the algorithm. After calculating the necessary power level, based on the distance (so that we can still use a modulation at the edge of the coverage area), we apply the cluster formation algorithm. These algorithms do not take in consideration the frequency usage, and minimization of interference, but based on node density and number of nodes form groups which are delimited only by their own power. For example a node can be from a corner of the network, and another one from the other corner, and between the two nodes we can find other clusters, which make it possible for our two nodes to communicate.

After the clusters are formed, we delimit a single cluster, on which we apply our algorithms, to evaluate its behaviour and characteristics. In our case we chose the Maximum Spanning Tree algorithm, and an improved implementation of Ford Fulkersons algorithm for maximum cut/minimum flow. These algorithms can be anything, including routing algorithms (as demonstration, the Dijkstra's algorithm is also implemented). When we are finished working with the cluster, we can proceed to the next cluster, or we can work with more clusters in parallel. We chose to work with only one cluster, as it is sufficient to demonstrate the capabilities of this simulation platform, and visualize these processes by creating animations, which illustrate the algorithm step-by-step.

After this, we generate a random value for speed and a random value for direction. These two values are defined between a maximum and minimum value, so that the node speed would not influence the transmission rates. The speeds are relatively small (a Random Walk model is used, so the influence of Doppler effect can be neglected). As we generate these values, we transform from polar coordinates to Cartesian coordinates, and add the values to the initial position of the nodes. We apply algorithms to find the neighbouring nodes, and delimit the new clusters. They can be totally different from the initial clusters, because a node which belonged initially to another cluster gets close to a second clusters, and the node becomes a sort of point of connection, which makes the communication between the two clusters possible. There are nodes which do not belong to any clusters, due to the distance from other clusters, or the small power of emission.

After each cycle we save the data which will be processed, and an image which will become a frame in the final animation. There are two final animations, one to illustrate the random walk algorithm together with the cluster formation, and an animation which illustrates the intermediary processing of clusters, in this case, the Ford Fulkerson algorithm

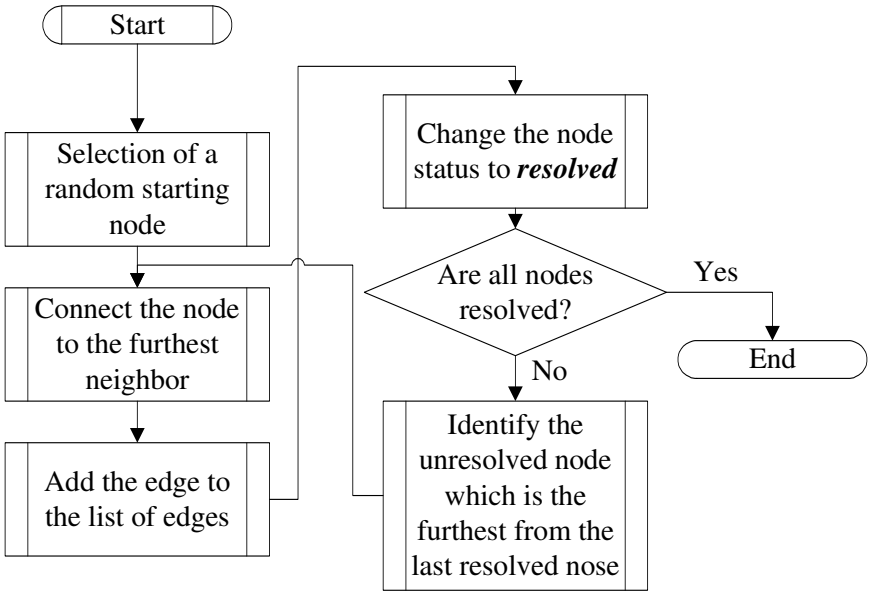

Figure 10: Flow-chart for maximum spanning tree

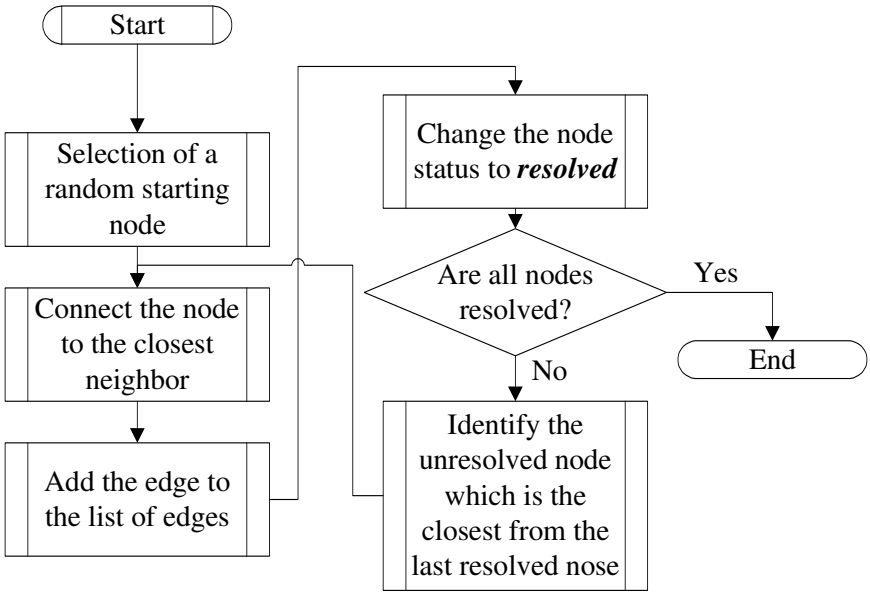

Figure 11: Flow-chart for minimum spanning tree.

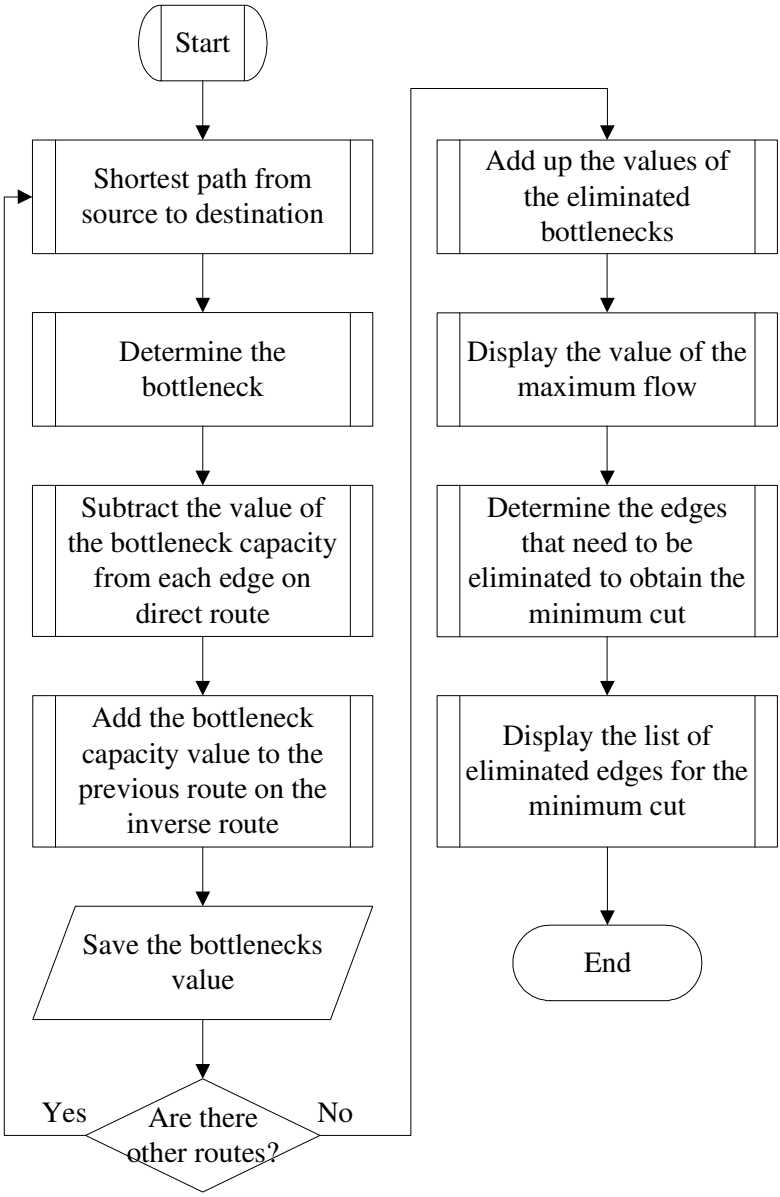

Figure 12: The improved Ford-Fulkerson algorithm.

After each cycle we save the data which will be processed, and an image which will become a frame in the final animation. There are two final animations, one to illustrate the random walk algorithm together with the cluster information, and an animation which illustrates the intermediary processing of

clusters, in this case, the Ford Fulkerson algorithm. This algorithm usually uses depth-first and breadth first algorithms. Here it is improved by applying Dijkstra's algorithm [20] for the shortest path. When routes are eliminated, the routing table is updated, and there is no need to reapply a depth first algorithm. The cluster information algorithm is a personal implementation. It uses the information saved in structures associated with each node in particular. The basic structure is the following:

```
vecin=struct('vec_nr',{},'vec_list',{},'head_list',{}
,'pwr_list',{});
util=struct('x',{},'y',{},'vecin',{},'ni',{},'clust_num',{}
,'flag',{});
clusters=struct('node',{},'elements',{});
```

Based on these informations, we can group nodes in clusters. The structure will contain the *x* and the *y* coordinates of the node, the *vecin* structure contains a list with the nodes neighbours, *ni* is a helping index, *clust_num* is the index of the cluster to which the current node belongs, and *flag* is a Boolean variable, helping in the algorithm. The structure *vecin* contains the number of neighbours, a list of the neighbours, a list with roots when the clusters are formed and a list of maximum transfer rates on all the edges associated with the current node. These maximum transfer rates were defined by the Euclidean distances between the nodes. The distance is calculated between the node and all of his neighbours, and from the distance the free space path loss is determined. This attenuation is subtracted from the emission power of the source node. From this SNR value we can determine with the help of the Hartley Shannon theorem the maximum transfer rate that can be achieved over this channel. The maximum transfer rates are used only in the cluster processing algorithms, and not in the cluster formation algorithms. The cluster formation algorithms are based only on distances and emission powers.

Fig. 13 illustrates the complexity of the structures we work with. Each element from the structure contains a list of Neighbour structures. This allows us to the dynamic change of the implementation: with the change of a single variable, all the structures change, and the necessary data is updated, so there are no contradictory information in the tables and structures.

When we work with data associated to a cluster, we can easily extract all the needed information. To do this, we simply use the indexing and the cluster number. When we extract the information from the structures, an adiecency matrix of the extracted cluster is created.

The structure Clusters will be containing all the formed clusters, and each element of the structure contains the number of nodes, and their indexes. This structure is created to exemplify the data extraction process [23]. From the

initial structure we can extract any variable and any structure. This information can be used for a different number of applications and simulations.

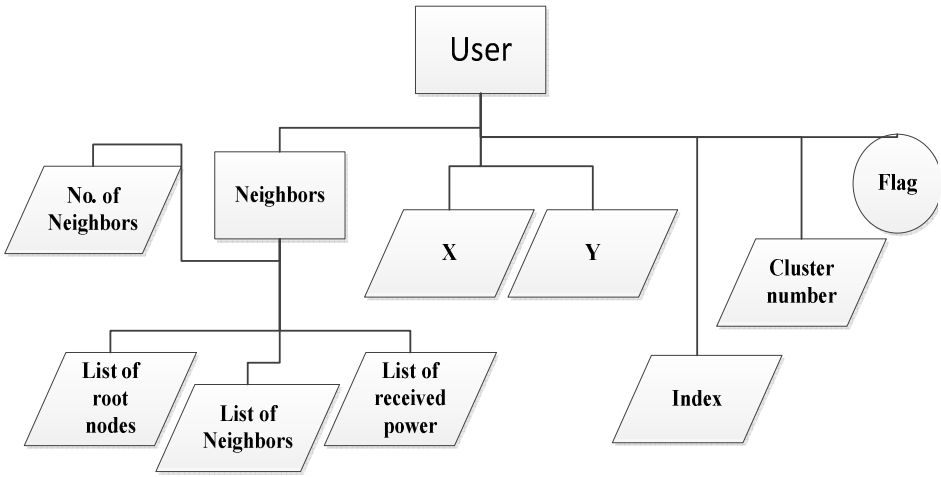

Figure 13: Data structure associated with one node.

4. Numerical results

We decided to compare the band of 2.4 GHz with the band of 5.25 GHz from the point of view of attenuation. (802.11a and 802.11b)[24]. Path gain is the inverse of the free space path loss function (*Fig. 14*).

We decided to use the 2.4 GHz band in this simulation. MANET-s uses both frequencies, so in our implementation can be changed at any time. In the case of WSN the used frequencies are lower, because their power consumption needs to be reduced to prolong the life of the nodes. Today, the frequencies used in wireless sensor networks include 315 MHz, 433 MHz, 868 MHz (in Europe) and 915 MHz in North America, and 2.45 GHz in the medical industry. This leads to the coverage of larger areas with the same number of mobile nodes, but meanwhile leads to greater interferences, due to the usage of the same bands by other applications. The interference signals can be analogical TV signals in the band of 400 MHz, GSM signals in the band of 900 MHz, Bluetooth signals from the GHz domain and interference from other electrical devices such as microwave oven, electro motors, etc. At small frequencies the free space path loss is not the most significant parameter. However, small frequencies require larger antennas. If the node density would allow distances of a couple of meters, and the users would not have antenna size constraints, a low frequency

implementation is the best solution. Frequencies of 70 MHz are used in some cases of wireless sensor networks.

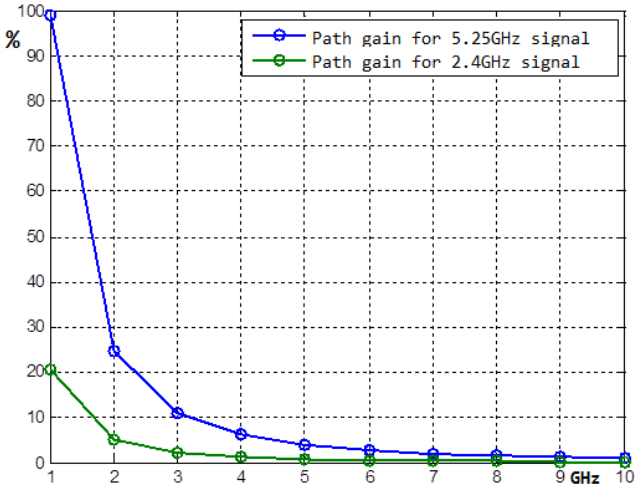

Figure 14: Free space path gain

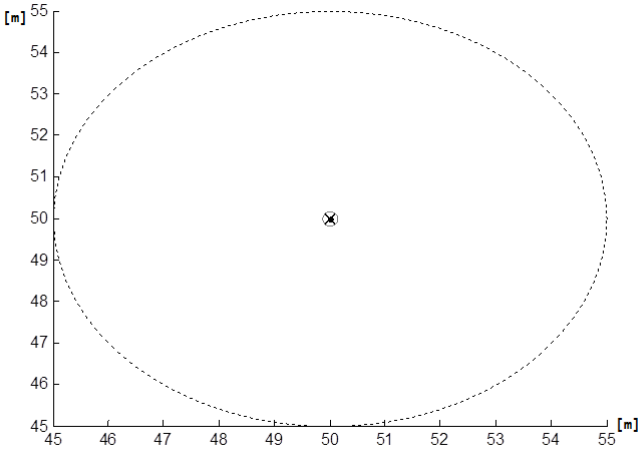

Figure 15: The coverage area of a node

We decided to set the emission power of a node in such a way, that at the border of the coverage area we can still use a modulation with a minimum number of phases (2PSK). This modulation requires a signal noise ratio of 9.5dB. On a distance of 100 m the expression of the free space pathloss is:

$$FSPL = 10\log_{10}\left(\frac{3\cdot 10^8}{4\pi\cdot 100\cdot 2.4\cdot 10^9}\right) \quad (1)$$

The result is 16dB. So we set the power of emission to 9.5dB+16dB = 25.5dB. The coordinates of the users are randomly generated on a finite surface with a Gaussian distribution.

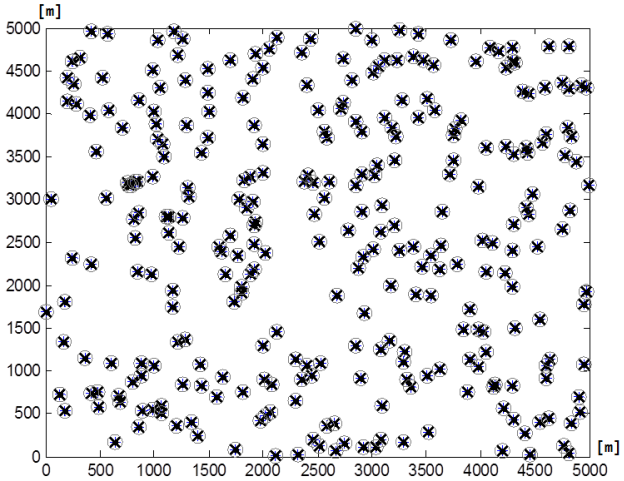

Figure 16: Surface with distributed nodes

We generated the x and y coordinates separately, and created structures containing all the necessary information related to the node. Initially they contain only the node coordinates. The chosen surface is a surface of 5000×5000 square meters and the user/node number is 300.

After establishing the range of all the nodes, we applied an algorithm which calculates all the Euclidian distances to all the neighbouring nodes delimited by this range.

$$d = \sqrt{(x - x_0)^2 + (y - y_0)^2} \quad (2)$$

So to the initial structure was completed with a list of neighbours containing the index of the neighbouring nodes, so we can obtain their coordinates at any given time. This was necessary, because in a system with nodes, there is not even one node which has knowledge about the whole network, they only communicate directly with neighbouring nodes. We decided that the cost function associated to the edges between the nodes to not be the Euclidian distance, but maximum transfer rates. As long as we have information about the

neighbours, we can apply the Hartley-Shannon theorem, which defines the maximum possible transfer rate on a channel with noise.

$$C = B\log_2\left(1+\frac{S}{N}\right) \tag{3}$$

We consider that B is 1 Hz (we evaluate spectral efficiency), and the signal noise ratio is defined by the difference between the emission power level of the node and free space path loss between the node and his neighbour, in other words the effective distance between the two nodes.

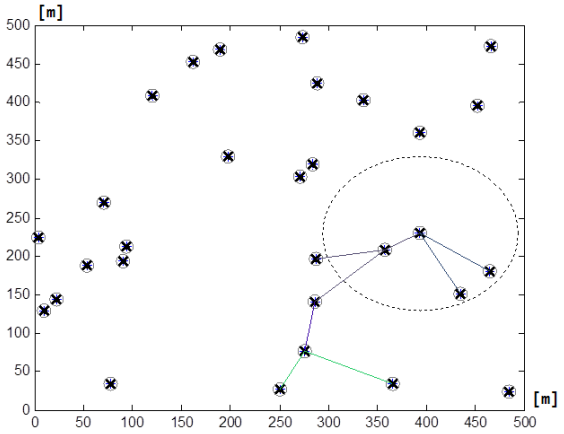

Figure 17: Determined grades of vicinity.

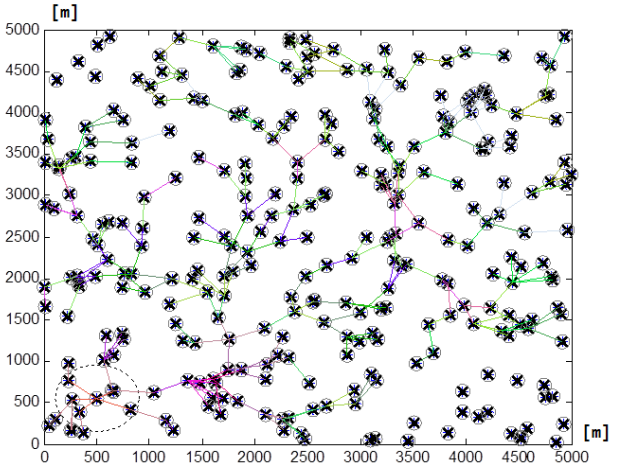

Figure 18: Generating the vicinity level map with a high user density.

If we want a walk on the graph, if we start from the information stored in one node, we can arrive to all the nodes calculated as neighbours, and defined as 1st grade neighbours. From them we can arrive at the neighbours of the neighbours, which are 2nd grade neighbours to the initial node. With this algorithm we can form a spanning tree, which contains information about the maximum transfer rates on the edges. When the node density is too small, the graph will not include all the nodes, but form a cluster instead with a small number of nodes. The users inside a cluster can communicate, and all that we have to do is to apply an inter-cluster routing algorithm, to connect all the formed clusters

We decided to apply the algorithm deciding the vicinity levels to a network with larger user density, and observed that by defining a power level above a certain limit, the whole network will be interconnected. We chose a random source node and a random destination, and illustrated this vecinity level map with different colours.

The figures illustrate that in these networks, where the node density is high, communication can be accomplished between any two nodes, moreover there is a large number of possible routes between them. We decided to demonstrate with the Ford-Fulkerson algorithm, that these transfer rates are limited because of the bottlenecks, which appear due to the large distances. The simplest way to put this is: on a route from node A to node B the maximum transfer rate is limited by the minimum transfer rate on one of the edges on this route.

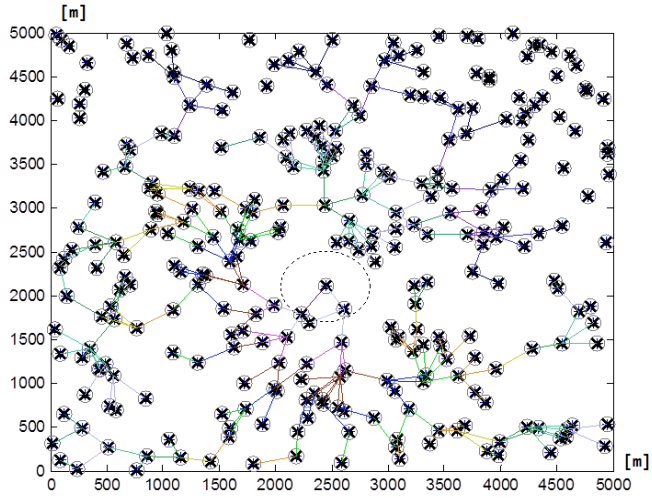

Figure 19: Generating the vicinity level map with a high user density with a random source and random destination node.

As a next step, we reduced the density of the nodes by reducing the total number of nodes on the defined surface. We can arrive at the same results, if we reduce the emission power of the nodes. As we can clearly see, not all nodes are connected to a graph. We applied an algorithm which groups the nodes which can communicate with each other into clusters.

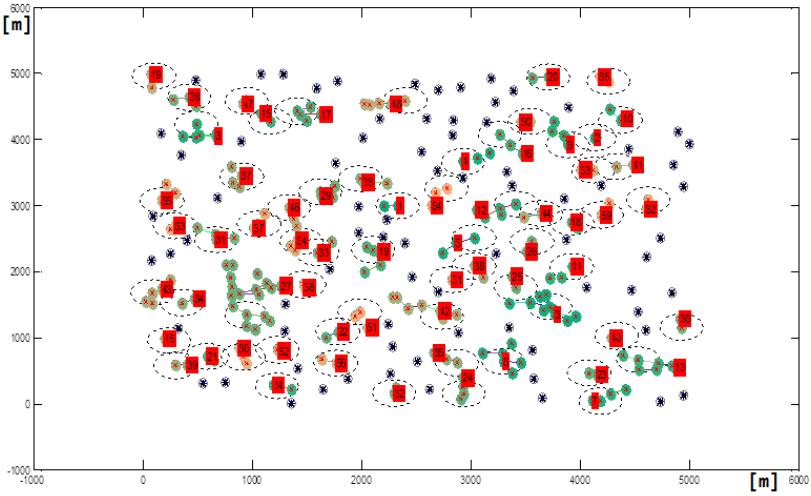

Figure 20: Cluster formation.

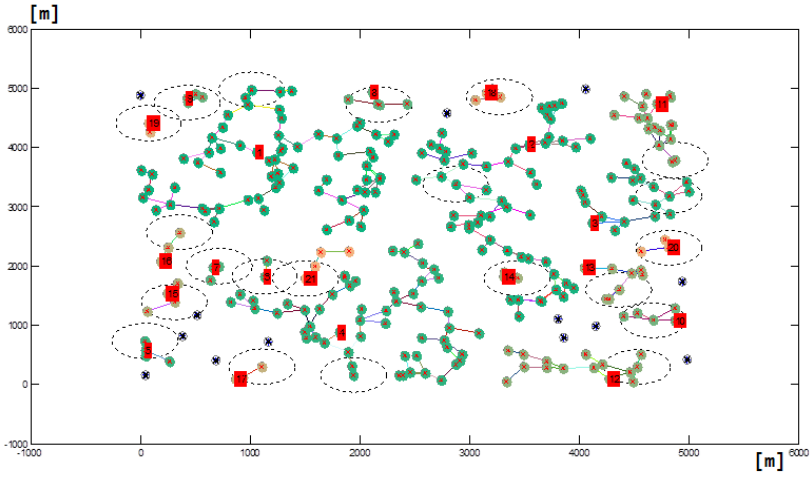

Figure 21: Cluster formation with an improved coverage area.

As we can see, the coverage area of the nodes influences the number of clusters that will form. These new clusters are structures which make the communication among them possible. For a more detailed analysis of these formed clusters, we took the first cluster, and applied a set of different algorithms to it.

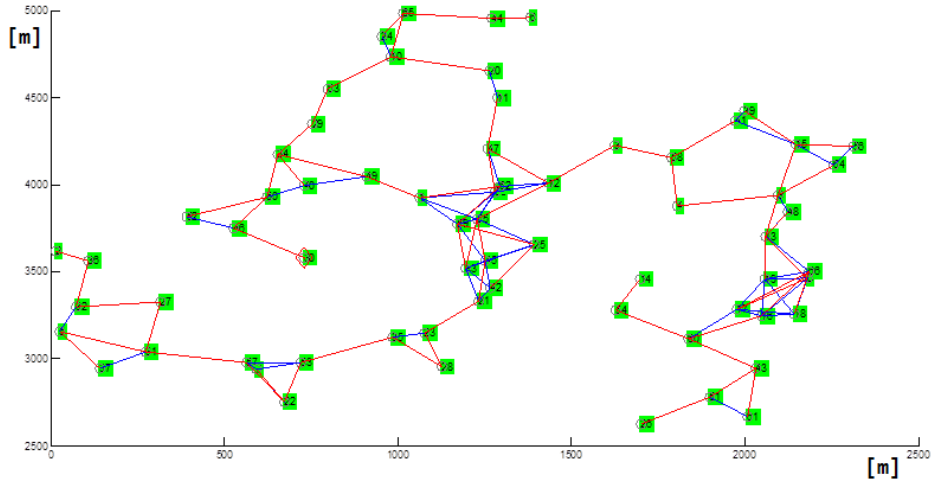

Figure 22: Implementation of Maximum Spanning Tree on a cluster.

We took the cluster with the number 1 index from the previous figure, and made a map with all the possible connections between the nodes with blue lines. Based on these connections, we applied the Maximum spanning tree algorithm, and redrew the edges being part of this spanning tree with red. The source node can be chosen arbitrary. The trees formed by this algorithm are always full trees, because they were interconnected in the first place, and the graph contains all nodes of the system.

Application of the Ford Fulkerson algorithm:

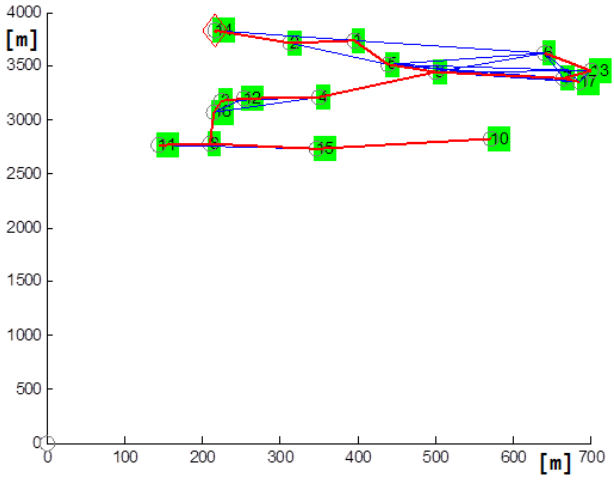

Figure 23: Spanning Tree of the cluster that will be processed.

In the theoretical part we described the algorithm step-by-step. In our simulations it looks the following way:

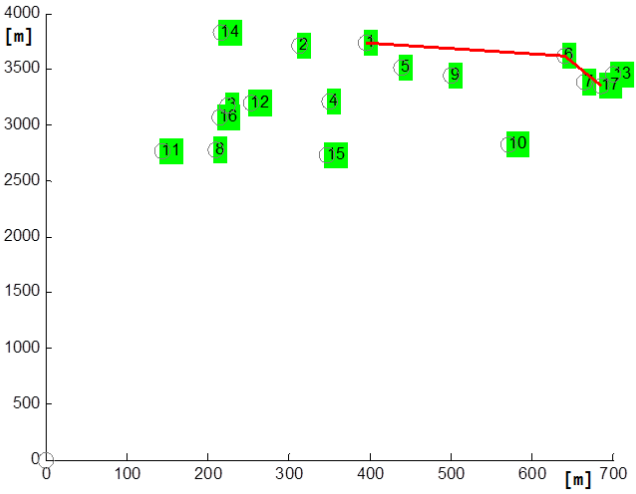

Figure 24: First route found by Dijkstra's algorithm between node 1 and 17.

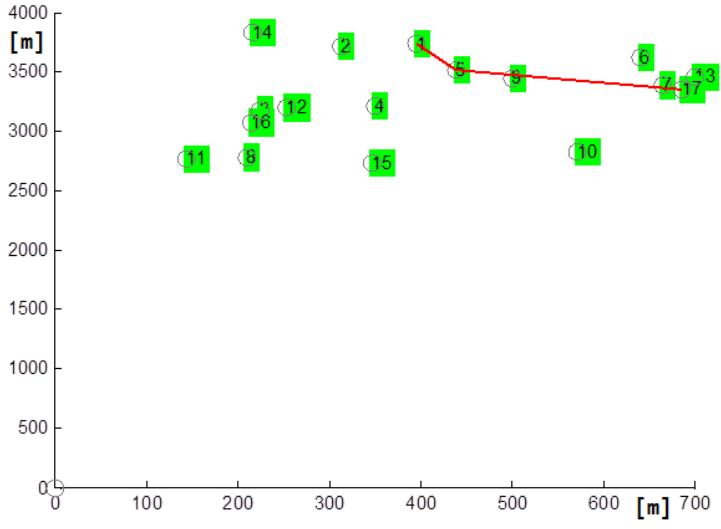

Figure 25: Second route found after an edge was eliminated.

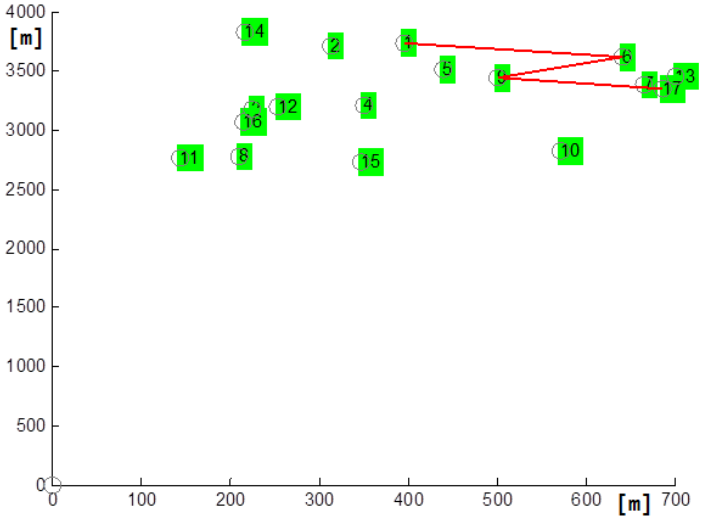

Figure 26: Third path after another edge was eliminated.

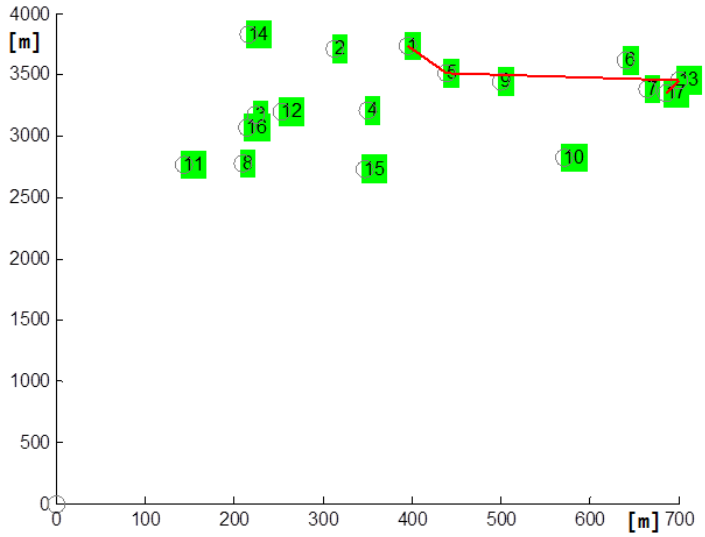

Figure 27: Fourth path after another edge was eliminated.

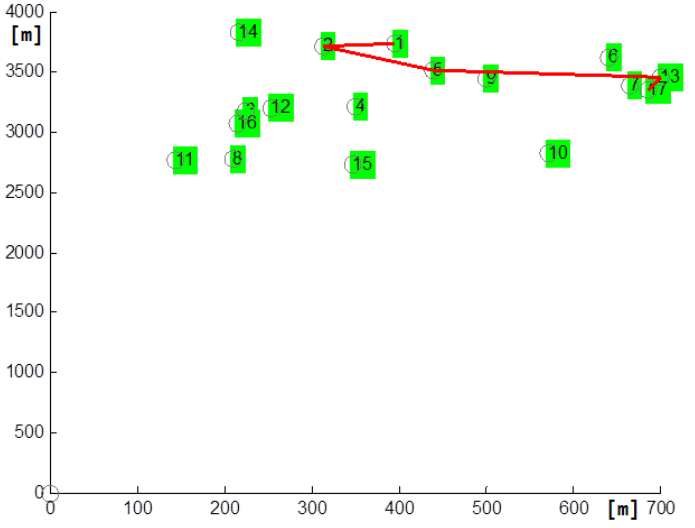

Figure 28: Last possible path, after eliminating the last possible edge.

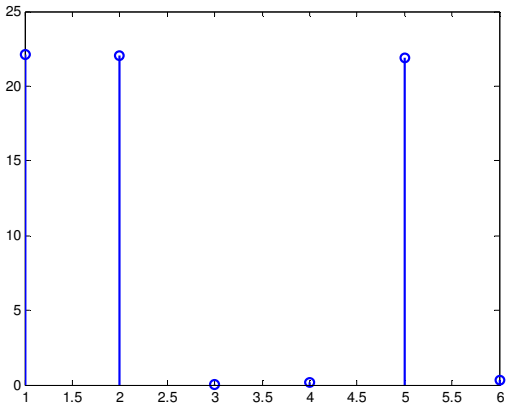

Figure 29: Graph of cuts.

The sum of the cuts gives us the minimum cut, or the maximum flow between the two nodes.

Their sum in the previous example is:

$$22.12 + 22.06 + 0.0093 + 0.21 + 21.92 + 0.3507 = 66.67 \quad (4)$$

The improvement brought to the Ford-Fulkerson algorithm was Dijkstra's algorithm. Instead of depth-first or breadth-first we used the data already obtained with the shortest path algorithm. After eliminating an edge with each step, we updated the tables from the previous Dijkstra algorithm. When we ran out of possible paths, the algorithm ended, and we added up the flows we cut in each step, so we arrived at the maximum flow between the two nodes. To be noted: this transfer rate is a maximum theoretical transfer rate between the two.

We decided to finalize the simulation by adding mobility to the nodes. At this step, we needed to change the position of the nodes. The random speed and random direction was achieved by generating two random numbers, one being the speed and the other the direction. These variables were transformed from polar coordinates to Cartesian coordinates, and added to the initial position. This way we updated all node positions from our system, after which we can reapply the cluster formation algorithms and the cluster processing algorithms.

6. Conclusion

In this paper we proposed the creation of a software platform, that allows the study of the behaviour of nodes in a wireless ad-hoc network, and allows the analysis of these systems by adding new elements to the initial data structures

associated with a node (position, emission power, vicinity list, index of cluster), and with the possibility of choosing the node density of the system, adding new nodes, eliminating nodes or changing the emission power.

After applying the cluster formation algorithm, we applied cluster processing algorithms to the obtained graphs, like: minimum spanning tree, maximum spanning tree, shortest path algorithms, and the minimum cut maximum flow of Ford Fulkerson.

Given the current rate of development in wireless ad-hoc networks, in the future there will be a need for simulation platforms which allow us the study of the behaviour of the network elements, allow us to experiment with routing algorithms, and allow us the analysis of protocols used in these types of systems, networks.

Even if these networks have the capacity to develop in the next few years, they have only acquired attention in the last couple of years. Because of the improvement of technology, the user terminals are getting smaller and smaller and the transfer rates are improving by the day due to system improvements. This branch of communications will meet a great demand in the next couple of years.

As a continuation of this paper, we can consider the possibility of the analysis of routing protocols used in wireless mobile ad-hoc networks (both WSN and MANET), with the help of this platform, from the routing efficiencies point of view. Improvement to the cluster formation algorithms can be made by using more complex algorithms, currently studied by the companies who implement solutions for WSN. Other improvements can be brought by the study of the physical layer, by adding frequency reutilizations schemes to the simulation, and resolving the interference issues in these systems. This aspect was not approached in our simulation platform.

References

[1] Prasad, R., Mihovska, A., "New Horizons in Mobile and Wireless Communications", Artech House Universal Personal Communications series, vol. 4, 2009.

[2] Johnson, D., "Dynamic Source Routing in Ad Hoc Wireless Networks", C*hapter of Mobile Computing, Kluwer Academic Publishers*, 1996, pp. 153-181.

[3] Özcan, A., Zizka, J., Nagamalai, D., "Recent Trends in Wireless and Mobile Networks", Springer Communications in Computer and Information Science series, vol. 162 ISBN: 978-3-642-21936-8, June, 2011.

[4] Anandamoy, S., "Swarm Intelligence based optimization Of MANET cluster formation", *Ms. C. Thesis,* Faculty of Electrical and Computer Engineering, University of Arizona, 2006.

[5] Delavar, A. G., Artin, J., Tajari, M. M., "PRWSN: A Hybrid Routing Algorithm with Special Parameters in Wireless Sensor Network", in *Proc. of Third International Conferences, WiMo 2011 and CoNeCo 2011, Ankara, Turkey*, June 26-28, 2011, pp. 145-158.

[6] Luo, J., Xinxing, G., Tong, Z., Wei, Y., "MI-VANET: A New Mobile Infrastructure Based VANET Architecture for Urban Environment", in *Proc. of IEEE 72nd Vehicular Technology Conference Fall* (*VTC 2010-Fall*), 6-9, Sept. 2010, pp. 1-5.

[7] Lauer, G., "Packet-radio routing", in *Routing in Communications Networks, edited by Martha E. SteenStrup*, chapter 11, pp 55-76, Prentice-Hall, Englewood Cliffs, New Jersey, 1995.

[8] Clausen, T., "A MANET Architecture Model", *Systemes communicants Projects Hipercom*, January 2007, http://hal.inria.fr/inria-00136862.

[9] Hedrick, C., "Routing Information Protocol", Rutgers University RFC 1058, June 1988.

[10] International Standards Organization. "Intermediate system to intermediate system intra-domain routing exchange protocol for use in conjunction with the protocol for providing the connectionless-mode network service (ISO 8473)". ISO DP 10589, February 1990.

[11] Jubin, J., Tornow, J. D. "The DARPA packet radio network protocols", *Proceedings of the IEEE*, vol. 75 Issue 1, pp. 21-32, Jan. 1987.

[12] Perkins, C., "Ad Hoc Networking", Addison Wesley 2001.

[13] Jiang, M., Li, J., Tay, Y. C., "Cluster Based Routing Protocol(CBRP)", National University of Singapore, 14 August 1999, http://tools.ietf.org/html/draft-ietf-manet-cbrp-spec-01.

[14] Perkins, C., "Ad-hoc On-Demand Distance Vector Routing", in *proc. of Second IEEE Workshop on Mobile Computing Systems and Applications WMCSA '99.*, *New Orleans, USA,* 1999. pp. 90-100.

[15] Hong, X., Xu, K., Gerla, M., "Scalable Routing Protocols for Mobile Ad Hoc Networks." *IEEE Networks,* vol. 16. no. 4, pp. 11-21, Jul/Aug 2002.

[16] Wang, Y., Chen, H., Yang, X., Zhang, D., "Cluster based location-aware routing protocol for large scale heterogeneous MANET", in *Proc. of Second International Multi-Symposiums on Computer and Computational Sciences, 2007. IMSCCS 2007.*, *Iowa City, USA,* 13-15 Aug. 2007 pp. 366-373.

[17] Clausen, T., Jacquet, P., "Optimized Link State Routing Protocol (OLSR)." RFC 3626, IETF Network Working Group, October 2003.

[18] Ramanathan, S., "Scheduling Algorithms for Multihop Radio Networks," *in IEEE/ACM Transactions on Networking,* vol. 1, No. 2, 1993, pp. 166-177.

[19] Handy, M. J., Haase, M., Timmermann, D., "Low energy adaptive clustering hierarchy with deterministic cluster-head selection", *4th International Workshop on Mobile and Wireless Communications Network*, 2002. pp. 368-372.

[20] Dijkstra, E., "A discipline of Programming", Prentice Hall, 1976.

[21] Lindsey, S. Raghavendra, C. S., "PEGASIS: Power-Efficient GAthering in Sensor Information Systems", *IEEE Aerospace Conference Proceedings*, vol. 3, pp. 1125-1130, 2002.

[22] Ford, L. R., Fulkerson, D. R., "Flows in Networks", Princeton University Press, 1962.

[23] Chinneck, J., "Practical Optimization: A gentle introduction", textbook Systems and Computer Engineering, Carleton University, 2000, http://www.sce.carleton.ca/faculty/chinneck/po.html.

[24] Cheung, D., Prettie, C., "A Path Loss Comparison Between the 5 GHz UNII Band (802.11a) and the 2.4 GHz ISM Band (802.11b)", January 2002, http://paginadellatecnica.xoom.it/paginadellatecnica/802_11a-vs-b_report.pdf.

Acta Universitatis Sapientiae
Electrical and Mechanical Engineering, 4 (2012) 33-44

Dynamic Pressure Control in Reactive Sputtering Process

Albert-Zsombor FEKETE, László JAKAB-FARKAS,
Sándor PAPP, Tibor-Csongor BALOGH

Department of Electrical Engineering,
Faculty of Technical and Human Sciences,
Sapientia Hungarian University of Transylvania, Tg. Mureş,
e-mail: {zsombor.fekete; csongor. balogh}@tetronic.ro
{jflaci; spapp}@ms.sapientia.ro

Manuscript received March 15, 2013; revised June 15, 2013

Abstract: Reactive magnetron sputtering is used to create TiN_y and TiO_xN_y wear resistant nanostructure thin film coatings. In order to achieve a successful sputtering process which can be reproduced at any time, it is important to develop control units for the interdependent parameters of the system.

The purpose of this paper is to present the effect of the dynamic pressure upon the sputtering process and the design curs of the embedded pressure controller unit. The unit features a dual DSP microcontroller architecture in order to handle the defined tasks. There is a study on the analytical modeling process, which is based on the ideal gas law. With proper deduction and by introducing into the equation the gas flow rate and the pumping efficiency we managed to obtain a dynamic model. After conducting several tests we concluded that the obtained model has a global error less then 2%. The process is non-linear, but because throughout the sputtering process the value of the dynamic pressure varies in a relatively small and linear interval (1205 $\cdot 10^{-3}$ and 3 $\cdot 10^{-3}$ Torr), we managed to design, tune, fine-tune and implement a PID regulator. Based on simulation results we identified the need for a "*combined PID control algorithm*" which operates with different sets of parameters in function of the error, improving the quality of the control. In conclusion we can state that the developed embedded system fulfills all the requirements.

Keywords: reactive sputtering, thin film coatings, partial pressures, analytical model, embedded dynamic pressure controller, PID control algorithm.

1. Introduction

One of the most widely used physical vapor deposition (PVD) method for creating useful compound thin film coatings is the reactive sputtering [8]. At the International Physics Laboratory DC reactive magnetron sputtering is used to create titanium nitride (TiN_y) and titanium oxynitride (TiO_xN_y) wear resistant nanostructure thin film coatings with the use of argon inert gas, oxygen and nitrogen reactive gases and titanium target. These coatings are produced and studied with the aim to be used in different industrial applications exploiting their versatile properties.

It is important to emphasize that in order to perform a successful reactive sputtering process which can be reproduced at any time, due to the complexity of the process we need a controlled environment. This implies designing and implementing a series of control algorithms for the interdependent factors and parameters that influence the sputtering, such as the dynamic and partial pressures inside the vacuum chamber [1].

The purpose of this article is to present the process thru which we developed a controller for the dynamic pressure. This process includes the design of the hardware and software elements of the embedded system, the analytical modeling process with additional Matlab applications to tune and simulate the system and to verify the correctness of the non-linear mathematical model which played an essential role in designing, tuning and simulating the controller algorithm. The developed pressure controller unit due to the methodology and the Matlab applications can be used for other reactive sputtering systems as well with similar construction [1].

2. Concept of the dynamic pressure

In the sputtering process the argon inert gas has the role of bombarding the titanium metallic target without reacting with it. The oxygen and nitrogen gases on the other hand react with the sputtered material forming a stoichiometric compound. As an unwanted side effect oxygen or nitrogen coatings may be deposited on the surface of the target, process known as target poisoning. This phenomenon has a massive negative effect on the efficiency of the sputtering process and structure of the thin film coating. As a direct consequence the cathode gets electrically isolated, which means that it goes from metallic state to nitrated state [3] [5] [8]. In order to eliminate the presented side effect and to maintain the system in a desired operating point, it is necessary to design and develop a pressure controller unit.

Based on the simplified schematic (*Fig. 1.*) of the experimental equipment used at the International Physics Laboratory, it can be easily identified that the

dynamic pressure is determined by the flow rate of the gases and the pumping speed of the turbomolecular pump. We can also state that the sum of the partial pressures produced by the inert and reactive gases introduced into the vacuum chamber is equal with the dynamic pressure [1] [5]. The pumping speed of the turbomolecular pump is constant, but it can be modified with the butterfly valve mounted directly in the evacuating duct. In order to perform a reactive sputtering process, inert and reactive gases need to be introduced into the vacuum chamber. This implies that these gases have to be introduced in a controlled way. For this task we used three independent mass flow controllers (MFC) with the help of which we can determine not only the desired flow rate, but we can measure it as well. These values are indispensable in the modeling process and they can be used also to verify if the MFC units are working properly.

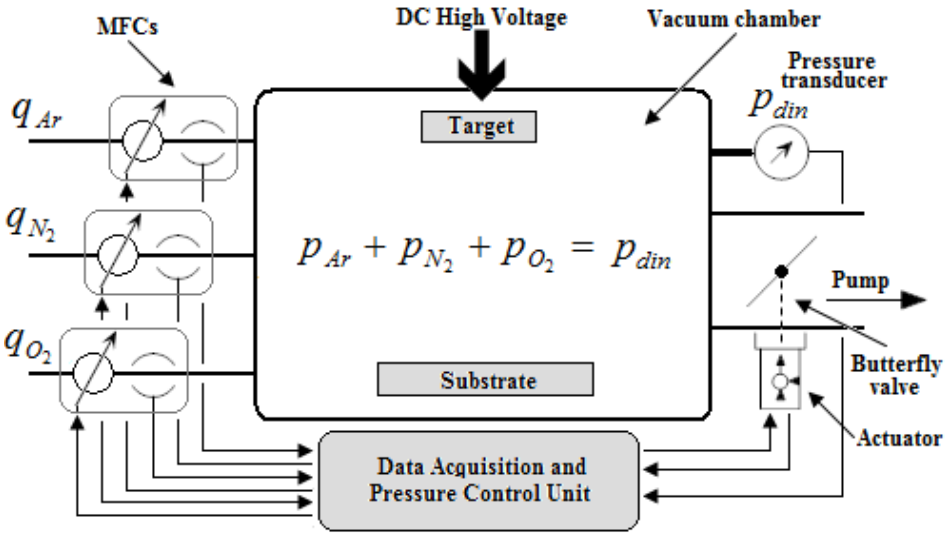

Figure 1: Simplified schematic of the experimental equipment [1].

3. Designing the embedded system

The first task was the development of an independent embedded system, also known as Data Acquisition and Pressure Control Unit. Based on the simplified schematic (*Fig. 1.*) we can identify the 5 measured analog inputs (the value of the dynamic pressure, the actual position of the butterfly valve and the three gas flow rate values) and 4 outputs (set point values for the mass flow controllers and for the actuator). All the inputs and some of the outputs are analog signals

and because we are using numeric embedded system, we need to include analog to digital converters with different resolutions. For the flow controllers we are using 12bit MCP4921 digital to analog and integrated analog to digital converters.

When using two or more gases, we no longer can measure the values of the partial pressures, only the value of the dynamic pressure. For this task we opted for an analog Pfeiffer Vacuum capacitive transducer. The analog signal provided by the unit is digitalized with a 16bit external AD7705 sigma-delta analog to digital converter. We opted for this component, because it has good noise rejection, accuracy of ± 0.003%, low rms noise (< 600nV) and integrated self-calibration options, which eliminate endpoint errors. In order to achieve the desired pressure control accuracy, the converter functions only in the working interval of the pressure scale. The obtained resolution is $3.5 \cdot 10^{-7}$ Torr resolutions, which is adequate for our application.

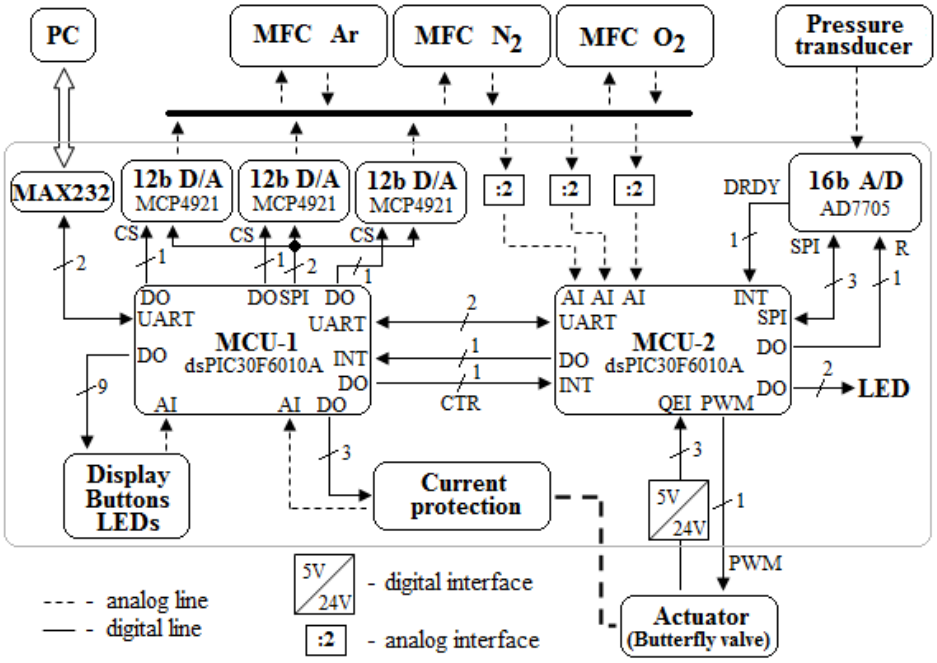

Figure 2: Bloc schematic of the embedded system.

The bloc schematic of the embedded system can be seen on *Fig. 2*. The Unit is based on two dsPIC30F6010A DSP microcontrollers with well defined

functions and tasks. Because the computing capacity for all the tasks implemented (executing the control algorithm, operating the Human Machine Interface, data logging, communication, etc.) on the system exceeded the capacity of a single controller, we decided to divide the tasks between two DSPs, which exchange data via serial communication. The first unit controls the Human Machine Interface (the LCD display, the button cluster, LEDs and the potentiometer for manual control of the butterfly valve), generates the set point values for the MFCs and establishes communication with the second unit and the central computer. The second microcontroller is basically reserved for the pressure control task. From the pressure controllers point of view it is very advantageous that this unit directly measures all the gas flow rates, the dynamic pressure, the valve angle, runs the control algorithm (PID) and generates the control signal for the actuator.

The actuator assembly for the butterfly valve is based on a Futaba S3152 digital high speed and high torque RC servo unit and a Hengstler RI41 rotary encoder. A detailed study revealed that the unit has a maximum resolution of 0.15° and a global error less then 10%.

4. Modeling process - Methodology

One of the key features of this work is the analytical modeling process of the dynamic pressure. In order to simulate a control structure it is necessary to develop a dynamic model which is suitable for our experimental equipment. We obtained three separate dynamic models for the three gases, the sum of which is equal with the dynamic pressure [1] [4]. In the following we will present a generalized modeling process for one gas. The final equation is derived from the ideal gas law (1):

$$pV = nRT \tag{1}$$

From the ideal gas law we obtain a dynamic model by replacing the number of moles (n) with the ratio between the mass of the gas (m) and the molar mass (M) [1] [4]:

$$pV = \frac{m}{M}RT \quad \Rightarrow \quad \frac{dm}{dt} = \frac{MV}{RT} \cdot \frac{dp}{dt} \tag{2}$$

where:

$$\frac{dm}{dt} = q_{in} - q_{out} \tag{3}$$

The variation speed of the mass of the gas is equal with the difference between the introduced and evacuated gas flow rates (3). In this equation we have an unknown member, the value of the gas flow rate evacuated, because we do not have the possibility to measure it. This way it is assumed that q_{out} (4) is equal with the product of the pressure and the pumping efficiency which is a function of the valve angle alpha [1] [4].

$$q_{out} = p \cdot S(\alpha) \tag{4}$$

Based on butterfly valve geometry, the pumping efficiency has the following form:

$$S(\alpha) = K \cdot (S_1 + S_2 \cdot (1 - \cos(\alpha))) \tag{5}$$

Equation (5) can be simplified by merging the K constant with the two areas (S_1 and S_2) (6). This way the K_1 and K_2 constants can be identified based on real measurements.

$$S(\alpha) = K_1 + K_2 \cdot (1 - \cos(\alpha)) \tag{6}$$

In order to determine automatically the values of the constants, we developed different Matlab applications, which basically processed a series of measured values obtained with the help of the embedded system. The results showed that equation (6) isn't accurate enough. In order to rectify the problem, we observed that the K_2 is a linear function of the butterfly valve angle alpha [1]. We modified equation (6) and rerun the constant identifier application.

A. Result of the modeling process

As a result of the methodology presented in the previous chapter and with proper deduction we managed to obtain a non-linear analytical model for the three gases used (7).

$$\frac{dp}{dt} = \frac{RT}{MV} \cdot q_{in} - \frac{RT}{MV} \cdot p \cdot (K_1 + (a \cdot \alpha + b) \cdot (1 - \cos(\alpha))) \tag{7}$$

We conducted several test to verify the correctness of the principals, methodology and the obtained non-linear differential equation (7). The significant results are presented in *Fig. 3*. First we confirmed that the sum of the measured partial pressures (*Fig. 3a* argon – red dotted line, nitrogen – green dotted line, sum – red line) is equal with the measured dynamic pressure (*Fig. 3a* blue line) [1].

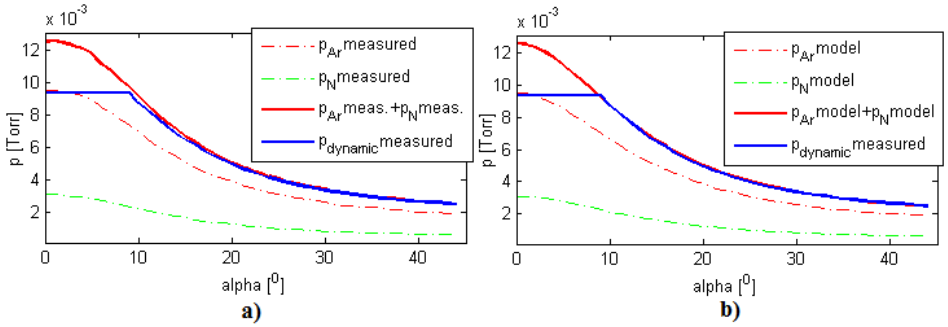

Figure 3: a) measured dynamic and partial pressures b) measured and simulated dynamic pressures and simulated partial pressures (argon and nitrogen) [1].

Because we can not measure pressure values greater then $9.5 \cdot 10^{-3}$ Torr, on both figures we can see a saturation at this threshold. Taking into consideration that throughout the sputtering process the value of the dynamic pressure is between $2.5 \cdot 10^{-3}$ and $3 \cdot 10^{-3}$ Torr, the upper threshold mentioned before does not interfere with the control process.

After the second test we concluded that the sum of the simulated partial pressures (*Fig. 3 b*) argon – red dotted line, nitrogen – green dotted line, sum – red line) is equal with the measured dynamic pressure (*Fig. 3 b*) blue line). The global error between the measured and simulated dynamic pressure is less then 2% [1].

5. Control algorithm

The numeric embedded system presented in the first part of the paper features two DSP microcontrollers. In order to implement a PID control algorithm it is necessary to use a discrete form (9) instead of the continuous one (8) [6] [7].

$$H_{PID}(s) = \frac{U(s)}{\varepsilon(s)} = K_p \cdot \left(1 + \frac{1}{T_i \cdot s} + T_D \cdot s\right) \tag{8}$$

Starting from this equation with backward (9) method and with proper deduction we obtained the discrete form (10) of the PID control algorithm.

$$s = \frac{z-1}{T \cdot z} \tag{9}$$

$$H_{PID}(z^{-1}) = \frac{q_0 + q_1 z^{-1} + q_2 z^{-2}}{1 - z^{-1}} \tag{10}$$

where:

$$q_0 = K_p\left(1+\frac{T}{T_i}+\frac{T_D}{T}\right)$$
$$q_1 = -K_p\left(1+\frac{2T_D}{T}\right) \quad (11)$$
$$q_2 = K_p\frac{T_D}{T}$$

From equation (10) we can obtain the discrete control signal, which has the following form:

$$u[k] = u[k-1] + q_0 \cdot \varepsilon[k] + q_1 \cdot \varepsilon[k-1] + q_2 \cdot \varepsilon[k-2] \quad (12)$$

The parameters present in the equation (11) need to be calculated only once or whenever the regulator parameters (K_p, T_i, T_d) are modified. The discrete control signal (12) is based on two basic operations and can be easily implemented on the microcontroller [6] [7]. To generate the T_s=*200 ms* sampling time we used a Timer and an interrupt routine.

As presented before the process is non-linear, but because throughout the sputtering process the value of the dynamic pressure varies in a relatively small interval ($2.5 \cdot 10^{-3}$ and $3 10^{-3}$ Torr), we managed to found a set of regulator parameters with which the control algorithm functions well within the prescribed interval.

For tuning the Ziegler-Nichols method was used. At first we obtained a regulator which had unsatisfying results because the overshot and the response time at perturbation exceeded the maximum allowed values (*Fig.5* – blue line, *Table 1*). By increasing the proportional coefficient, at set value modification an overshoot appeared, but at perturbation both the overshoot and the response time were within the maximum allowed limits (*Fig. 5* – red line, *Table 1*). Based on these simulation results we identified the need of a "*combined PID control algorithm*" which merges the positive qualities of the two set of regulator parameters. The results are collected in *Table 1*.

The parameter switching mechanism can be seen of *Fig. 4*.

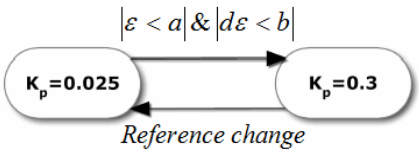

Figure 4: The parameter switching mechanism for the "*combined PID algorithm*".

By default the regulator uses the quick set of parameters. When there is a reference change (set value change) automatically the algorithm exchanges the two set of parameters. When the pressure stabilizes (the value of the error is less then "*a*" and the variation of the error is less then "*b*") then the mechanism changes back to the quick regulator. The values "*a*" and "*b*" were determined experimentally.

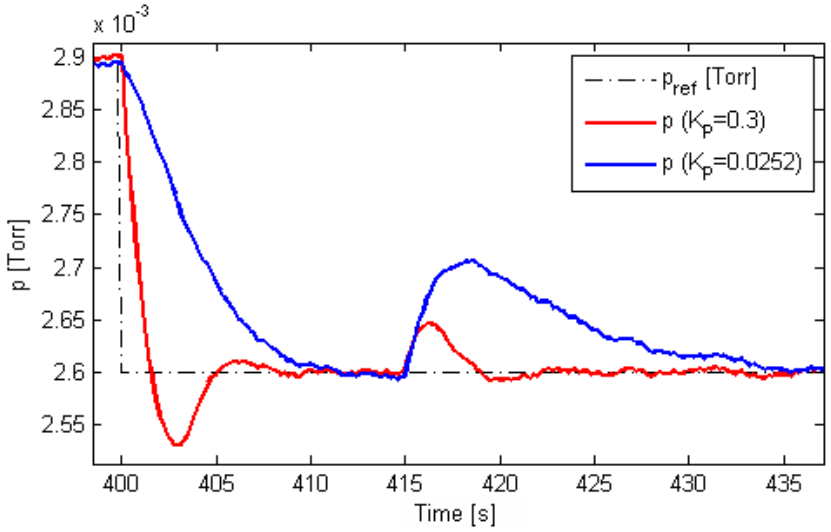

Figure 5: System response with PID control algorithm at set value modification and perturbation

Table 1: Simulation results for PID control algorithms

		Max. value	$K_p = 0.0252$	$K_p = 0.3$	*"Combined PID"*
Overshoot	σ [%]	3.46	-	2.65	-
Response time	t [s]	20	11.5	9	*11.5*
Overshoot and response time at perturbation	σ [%]	3.46	4.03	1.8	*1.8*
	t [s]	20	21.5	7	*7*

Based on the systems dynamic model we constructed a control loop (*Fig. 6*) in Simulink environment in order to tune the pressure control algorithm and to carry out the simulations presented before. Our main objective was to create a structure which functions as the real system, with a variation as little as possible. In order to achieve this, we conducted several tests and measurements

on the experimental equipment and integrated the results into Simulink subroutines. We studied the characteristics of the mass flow controllers, the capacitive pressure transducers, the sputtering systems and based on this knowledge we introduced noises, saturations, different perturbations for pressure and flow rates.

During the sputtering process an unwanted phenomenon occurs which modifies significantly the structure of the deposited thin film. This phenomenon is the disruptions of the plasma. When this occurs, it is important to reignite the plasma in the shortest time possible. This can be achieved by increasing the dynamic pressure inside the vacuum chamber till the point where the plasma can reignite or by increasing the high voltage. We opted for the first solution. The "Control signals" (*Fig. 6*) subroutine contains a structure with the help of which we can simulate the interruption of the plasma and the reigniting procedure. This routine was created using real measurements and knowledge gained from different tests. When the plasma is disrupted, the algorithm automatically suspends the function of the pressure regulator and fully closes the butterfly valve in order increase the pressure. When the plasma reignites, the algorithm reopens the valve to his previous position and when the pressure decreases to its controlled value, the pressure controller is enabled. Based on these simulations we integrated this function into the embedded system as well.

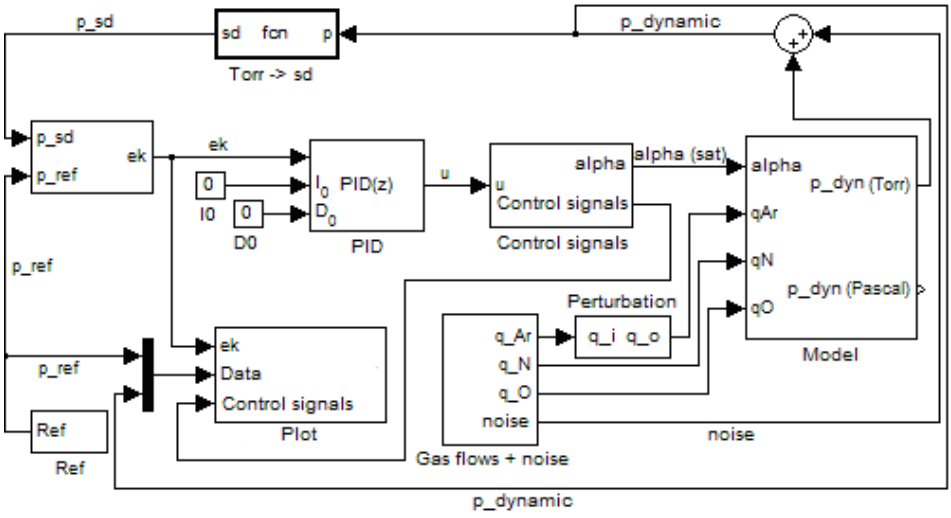

Figure 6: Control loop in Simulink environment.

After implementing the pressure controller and all the presented algorithms on the embedded system, we conducted tests to fine-tune the system and to verify the correct functioning. The benefits of using the "*combined PID control algorithm*"

over the regular one are clearly shown on *Fig. 7*. There is no overshoot and the response time is shorter with four seconds.

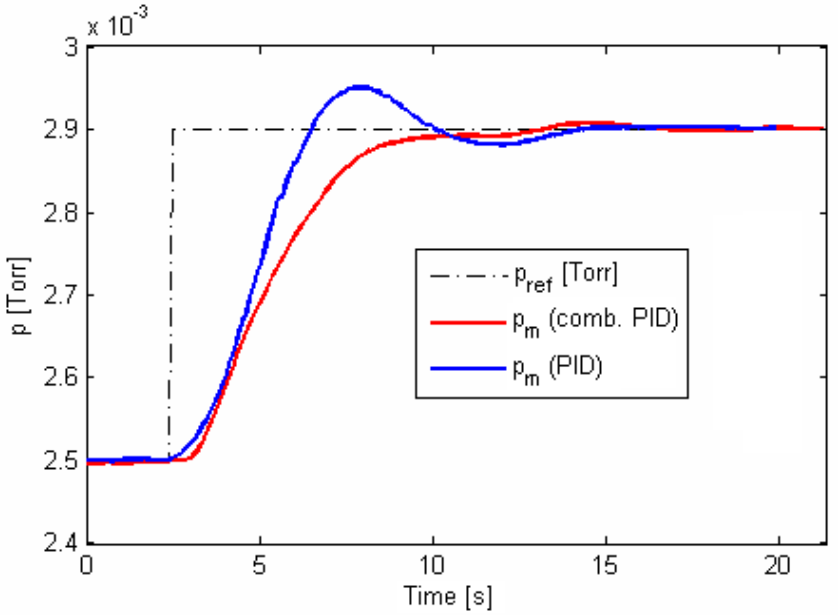

Figure 7: System response with implemented PID and "*combined PID*" control algorithms at set value modification – embedded system

6. Conclusion

As a result we managed to develop an embedded system for the control of the dynamic pressure. Throughout the study with proper deduction we obtained three analytical models of the partial pressures of the inert and reactive gases used in the sputtering process. It is important to emphasize that the modeling process is indispensable in designing, tuning and implementing the control algorithms. With the presented methodology and the developed Matlab applications the modeling process and the control unit can be used for other experimental equipments with similar structure. Based on simulation result we identified the need of a "*combined PID control algorithm*" which improved the control quality. In conclusion we can state that the developed system fulfills all the predefined requirements.

Acknowledgements

The authors thank Mr. Domokos BÍRÓ, András KELEMEN, Mrs. Katalin GYÖRGY and István SZÖLLÖSI from Sapientia University for their helpful support. This works was partially supported by KPI-EMTE Sapientia.

References

[1] Fekete, A. Zs., Papp, S., "Modeling of dynamic and partial pressures in reactive sputtering processes", in *Proceedings The 6th Edition of the Interdisciplinarity in Engineering International Conference*, University of Tîrgu-Mureş Romania, 2012, pp. 249-253.

[2] György, K., Kelemen, A., Papp, S., "Modeling and stability analysis of the nonlinear reactive sputtering process", in *Proceedings The 5th Edition of the Interdisciplinarity in Engineering International Conference*, University of Tîrgu-Mureş 2011, Romania, pp. 11-15.

[3] Berg, S., Nyberg, T., "Fundamental understanding and modeling of reactive sputtering processes", *Science Direct*, Thin Solid Films 476, 2005, pp. 215-235

[4] Papp, S., Jakab-Farkas, L., Bíró, D., Szabó, W., "Modeling and identification of study of the variation of dynamic pressure in reactive sputtering process", in *Proceedings The 5th Edition of the Interdisciplinarity in Engineering International Conference*, University of Tîrgu-Mureş, Romania, 2011, pp. 16-19

[5] Bíró, D., "Straturi subțiri nanostructurate", Editura Universității Petru Maior, Tîrgu-Mureş, Romania, 2004

[6] Lantos, B., "Irányítási rendszerek elmélete és tervezése", Akadémiai kiadó, Budapest, 2005

[7] Márton, L., "Irányítástechnika", Scientia Kiadó, Kolozsvár, 2009

[8] Martin, N., Sanjinés, R., Takadoum, J., Lévy, F., "Enhanced sputtering of titanium oxide, nitride and oxynitride thin films by the reactive gas pulsing technique", Surface and Coatings Technology 142-144, 2001, pp. 615-620

Acta Universitatis Sapientiae
Electrical and Mechanical Engineering, 4 (2012) 45-57

Bicycle Anti-Lock Braking System Prototype Development

Krisztian ENISZ, Istvan SZALAY, Denes FODOR,
Klaudia NAGY, Robert JAKAB

Department of Automotive Mechatronics,
University of Pannonia, Veszprém, Hungary
e-mail: fodor@almos.uni-pannon.hu

Manuscript received June 14, 2013; revised August 15, 2013

Abstract: The passive and also the active safety systems of the vehicles evolved in the last decades. Beside the safety system of cars and trucks the smaller vehicles like the motorbikes, scooters, e-bikes and bicycle's systems evolved as well. The aim of the project was to create and develop a prototype bicycle that uses a hydraulic type anti-lock braking system.

The paper presents shortly the dynamics of the bicycle and steps of development of the prototype and the developed control algorithm with experimental results.

Keywords: vehicle safety, vehicle dynamics, bicycles, motion control, modeling, simulation

1. Introduction

Nowadays more and more efforts are taken to make the road traffic safer. On the traffic side not even for the cars and trucks, but also for the motorbikes and bicycles there are extra safety products as well to avoid or at least to reduce the harms and injuries.

The most of the new cars are equipped with active safety-systems like anti-lock braking system (ABS), electronic stability program (ESP) [1]. For motorbikes there are also active protective systems such as anti-lock braking system, rear wheel lift off protection etc.

Bicycle is a much simpler construction there is no need to have a driving license to use one thus it is reachable easily as means of traffic. In the last years more and more people choose to use bicycle and high number of accidents

caused by bicyclists and suffered by bicyclists [2, 3]. A lot of people use it without the minimum protection, for example helmet, knee- or elbow-protector [4]. A simple fall can cause serious injuries. One solution to protect the rider is to have the safety function on the bicycle itself. This is the reason why a new project was started for examining the bicycle dynamics and developing hydraulic ABS for a bicycle.

The aim of the research was to create and develop a prototype bicycle that uses hydraulic type anti-lock braking system, and make a proof-of-concept development and test to prove, it is possible to develop an efficient dynamics based anti-lock braking system algorithm for bicycles. Also to get information what main difficulties can occur during development of a new, optimized bicycle anti-lock braking system.

2. Existing methods

Results of the research survey in the bicycle ABS field shows that there is no widespread active safety product for bicycles nowadays [5]. For electric motor aided or hybrid bicycles are already present, but regular bicycles are still not supported. There are some simple solutions by modifying the brake-pad shape, using springs in the brake wires and also exist more complex methods such as brake force distribution or balancing. Scanning the literature [5] a few proof of concepts could be found but any ready to buy product that uses some kind of intelligence does not exist. The idea to apply some intelligent decision aiding mechanism is relatively new. In the list below a few of them can be seen:

- Mechanical brake force distribution;
- Pneumatic aided ABS;
- ABS realization with electronic stepper motor.

From the list can be seen that many attempts have been initiated to solve the problem; but none of them use a hydraulic anti-lock braking system on both wheels. To elaborate the full wheel anti-lock braking system the development of a bicycle dynamic model has been started.

3. The Bicycle model

Some vehicle and bicycle dynamics based model was examined [6, 7, 8, 9] and a longitudinal dynamics based model was created to test the ABS control methods (*Fig. 1*). The main equations of the model can be seen below. The symbols of the equations can be found in (I).

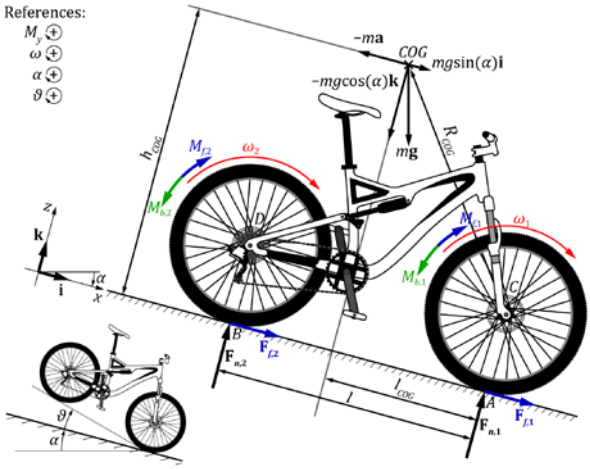

Figure 1: The forces, moments, references and geometry.

$$\sum F_x = ma_x = m\frac{dv_x}{dt} = F_{f,1} + F_{f,2} + mg\sin(\alpha) \tag{1}$$

$$\sum F_z = ma_z = m\frac{dv_z}{dt} = F_{n,1} + F_{n,2} - mg\cos(\alpha) \tag{2}$$

Table 1: Applied symbols for the bicycle model

Symbol	Description
M	the overall mass of the bicycle
a_x, v_x	the longitudinal acceleration and velocity of center of gravity (CoG)
$F_{f,1}$, $F_{f,2}$	the friction forces acting on front and rear wheels, respectively
a_z, v_z	the vertical acceleration and velocity of CoG
$F_{n,1}$, $F_{n,2}$	the normal forces acting on front and rear wheels, respectively
$\Theta_y^{(C)}$	the moment of inertia of overall bicycle about point C (the front wheel axle)
A	the slope angle of the road surface (considered as constant)magnetization
βy, ωy, ϑ	the pitch angular acceleration, velocity and pitch angle
L	the wheelbase of the bicycle
l_d, h_d	the lever arms
Θ_w	the moment of inertia of the wheels
B_1, β_2	the angular accelerations of the wheels
R	the radius of the wheels
$M_{b,1}$, $M_{b,2}$	the brake torques applied on front and rear wheels, respectively
Ω_1, ω_2	the angular speeds of the wheels
μ_1, μ_2	the friction coefficients of front and rear wheels, respectively
s_1, s_2	the relative slips of front and rear wheels, respectively

$$\sum M_y^{(C)} = \Theta_y^{(C)} \beta_y = \Theta_y^{(C)} \frac{d\omega_y}{dt} = \Theta_y^{(C)} \frac{d^2\vartheta}{dt^2} = \\ mg\sin(\alpha)h_d - mg\cos(\alpha)l_d - ma_x h_d - ma_y l_d + F_{n,2}l \tag{3}$$

Lever arms l_d, and h_d depend on pitch angle ϑ:

$$l_d = l_{COG}\cos(\vartheta) - (h_{COG} - R_{CoG})\sin(\vartheta) \tag{4}$$

$$h_d = l_{COG}\sin(\vartheta) + (h_{COG} - R_{CoG})\cos(\vartheta) \tag{5}$$

The equations below show the dynamics of the wheels:

$$\Theta_w \beta_1 = \Theta_w (d\omega_1 / dt) = F_{f,1}R + M_{b,1} \\ \Theta_w \beta_2 = \Theta_w (d\omega_2 / dt) = F_{f,2}R + M_{b,2} \tag{6}$$

The relations between the friction forces and normal forces are calculated based on (7).

$$F_{f,1} = \mu_1(s_1)F_{n,1} \\ F_{f,2} = \mu_2(s_2)F_{n,2} \tag{7}$$

Definitions of tire slips:

$$s_1 = (R\omega_1 - v_x)/v_x \\ s_2 = (R\omega_2 - v_x)/v_x \tag{8}$$

The torques produced by front and rear brake systems are denoted with M_1 and M_2. These are the available maximum torques, not the actually applied brake torques. These torques ($M_{b,1}$ and $M_{b,2}$) can only decelerate the front and rear wheels, their sign is always the opposite of the corresponding wheel speeds. The brake torques can block the braked wheels. Therefore if on the front wheel ω1 (on the rear wheel ω_2) is not zero, then:

$$M_{b,1} = -\mathrm{sgn}(\omega_1)M_1 \\ M_{b,2} = -\mathrm{sgn}(\omega_2)M_2 \tag{9}$$

If the wheel speed is zero, then the amplitude of the applied brake torque is equal to the minimum of M_i and the absolute value of the torque produced by the tire friction force, and acts against the torque produced by the tire friction force:

$$M_{b,1} = -\mathrm{sgn}(F_{f,1}R)\min(M_1, |F_{f,1}R|) \\ M_{b,2} = -\mathrm{sgn}(F_{f,2}R)\min(M_2, |F_{f,2}R|) \tag{10}$$

The longitudinal acceleration and speed are defined by (11) and (12). The pitch angular velocity are given by (13) and (14):

$$a_x = F_{f,1} + F_{f,2} + mg\sin(\alpha)/m \tag{11}$$

$$v_x = \int_0^t a_x d\tau + v_0 \tag{12}$$

$$\omega_y = \left(\int_0^t \sum M_y^{(C)} d\tau + \omega_0 \right) / \Theta_y^{(C)} \tag{13}$$

$$\vartheta = \int_0^t \omega_y d\tau + \vartheta_0 \tag{14}$$

The vertical acceleration and the relation between the normal forces are the following:

$$a_z = \beta R_{CoG} \cos(\vartheta + \vartheta_{CoG}) - \omega^2 R_{CoG} \sin(\vartheta + \vartheta_{CoG}) \tag{15}$$

$$F_{n,1} = ma_z + mg\cos(\alpha) - F_{n,2} \tag{16}$$

The torque caused by gravitational and inertial forces about point C is given by (17).

$$M_y = mg\sin(\alpha)h_d - mg\cos(\alpha)l_d - ma_x h_d - ma_z l_d \tag{17}$$

Normal force $F_{n,2}$ is non-negative. If the pitch angle ϑ is zero, than pitch angular acceleration cannot be negative. Therefore, if ϑ is zero and M_y is negative, then:

$$F_{n,2} l = mg\sin(\alpha)h_d - mg\cos(\alpha)l_d - ma_x h_d - ma_z l_d \tag{18}$$

Otherwise it results:

$$\Theta_y^{(C)} \beta_y = M_y = mg\sin(\alpha)h_d - mg\cos(\alpha)l_d - ma_x h_d - ma_z l_d \tag{19}$$

The model was implemented in Matlab/Simulink (*Fig. 2*) and was tested with our ABS control algorithm. On the *Fig. 3* there is the result of an emergency braking maneuver from 18 km/h. During these maneuver only the rear wheel speed is shown to be comparable with the implemented version of the algorithm.

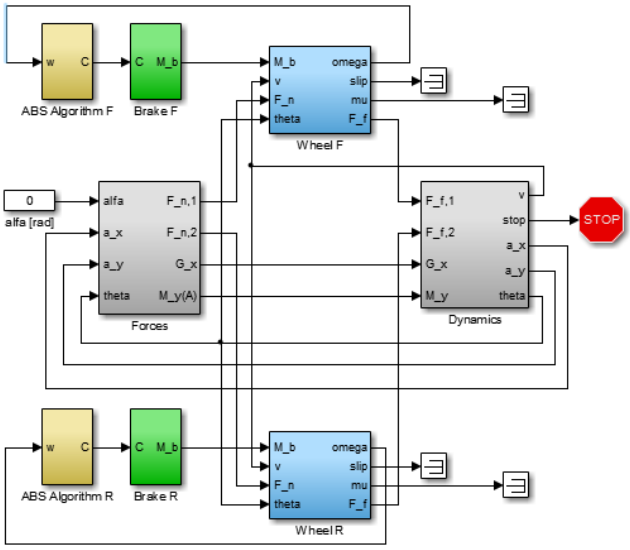

Figure 2: The Matlab/Simulink implementation of the vehicle dynamics based model.

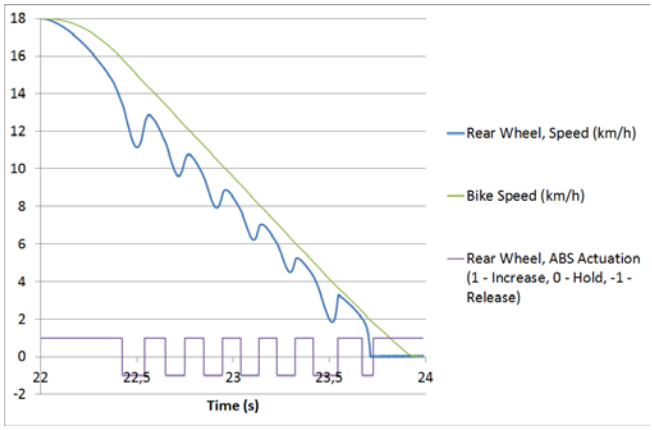

Figure 3: The result of a simulation (emergency braking with the rear wheel from 18 km/h, on dry asphalt).

4. The implemented control algorithm

The results of the simulations were in concordance with the expectations; it is possible to implement the model for an electronic control unit (ECU) of an ABS. Based on the experiences and knowledge from vehicle dynamics based model an ABS control algorithm was implemented in parallel in Matlab/Simulink and NI LabVIEW. The algorithm based on the comparison of the wheel speed and a calculated reference speed (the algorithm is the same for rear and front wheel, only the parameters are different).

A. Signal filtering

The incoming wheel speed is smoothed by a filter to decrease the noise in the signal (5):

$$v_{\text{filtered}}(n) = \left(\sum_{i=n-K_{\text{filter}}}^{n} v_{\text{unfiltered}}(i) \right) / (K_{\text{filter}} + 1) \tag{20}$$

where v_{filtered} is the filtered wheel speed, the $v_{\text{unfiltered}}$ is the unfiltered wheel speed and the K_{filter} is the filtering level which can be changed dynamically.

B. Road surface determination

The task of this part is to select the road surface from a look-up table according to the behavior of the wheels and the anti-lock braking system. The current algorithm chooses the road surface (and a friction coefficient value) from a look-up table, but a new method is under development which estimates this value by approximation methods.

C. Reference speed calculation

The calculation of the reference speed is based on a linear function defined by a speed slope value and the initial speed value (21):

$$v_{\text{ref}}(n) = S(n)N(n) + v_{\text{init}}(n) \tag{21}$$

where v_{ref} is the reference speed value defined by linear function, S is the speed slope, N is the elapsed time from measurement of the initial speed and v_{init} is the initial speed (the last valid speed value, before the actuation). The defined speed slope is dynamically changing during the braking by the changing of the road surface and the algorithm the v_{init} value is calculated in every loop based on (22):

$$v_{init}(n) = \begin{cases} v_{filtered}(n) & \text{if} \quad v_{ref}(n) \le v_{filtered}(n) \\ v_{init}(n) & \text{if} \quad v_{ref}(n) > v_{filtered}(n) \end{cases} \tag{22}$$

D. ABS state selection

The choice between the different states is based on the comparison of speed and the calculated reference speed (the states will be specified in details at the description of the prototype). The brake pressure at the wheel be reduced if

$$v_{\text{ref}}(n) / v_{\text{filtered}}(n) \ge K_{\text{release}}(n) \text{ and } v_{\text{ref}}(n) > v_{\text{limit}}(n). \tag{23}$$

The brake pressure will be hold if

$$\begin{aligned} &v_{\text{ref}}(n) / v_{\text{filtered}}(n) \ge K_{\text{hold}}(n) \text{ and} \\ &v_{\text{ref}}(n) / v_{\text{filtered}}(n) < K_{\text{release}}(n) \text{ and } v_{\text{ref}}(n) > v_{\text{limit}}(n) \end{aligned} \tag{24}$$

else the brake pressure will be increased.

In the equations K_{release} is the limit for the release state K_{hold} is the limit for the hold state and v_{limit} is the speed limit for ABS actuation.

E. State override

After the state selection there is a state override part. This is a safety function to prevent the actuation if some errors are detected or to prevent the overheating of the ABS hydraulic and electronic control unit (HECU).

5. The prototype

To test and validate the new ABS control algorithms a prototype bicycle was developed. The prototype is based on a professional mountain bicycle, equipped with high quality hydraulic brake system. The bike was not modified only the hydraulic brake pipes were cut (*Fig. 4*).

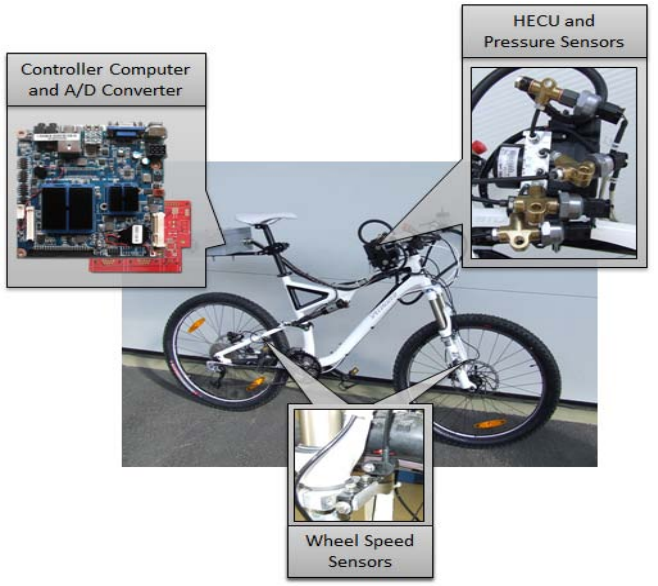

Figure 4: The hardware architecture of prototype.

A. ABS HECU block

The ABS HECU (Hydraulic and Electronic Control Unit) is a modified motorbike HECU. It consists of two main parts; one is the ECU (Electronic Control Unit) that is the electronic control part for the HCU (Hydraulic Control Unit) that modulates the flow of the brake fluid. The flow can be modulated from the brake-lever to the brake-pad, this is the inflowing part into the HCU, and also in the other direction that is the effluent part. The control unit currently works without a control algorithm and operates only as an actuator, the control algorithm function is disabled and an external controller has to send the control messages and states to the ECU. The active ABS has three different pressure modulation phases, and can actuate valves independently for the front and rear brake circuits: increase, hold, release.

The pressure on the brake pads that is modulated by the system is gained from the applied squeezing force on the hand-lever by the bicycle rider.

In the increase phase the pressure is let applied by the rider, not modulated by the HCU.

In the hold phase the oil flow is stopped from the inflowing (hand-lever) and the effluent (brake-pad) side also. Thus the pressure that is present on the brake-pads is hold.

In the release phase the pressure is stopped from the inflowing part, and the effluent part is open, so the pressure will be decreased on the brake-pads. In this

state the rider's squeeze-force does not matter, it has no effect to the pressure on the brake-pads.

To create the connection of the hydraulic system of the motorbike ABS and the brake system of the bicycle was difficult, because these parts were designed for different pressure intervals and filling methods.

B. The wheel speed sensors

On the bicycle there are four different active wheel speed Hall-sensors to test which one is the most suitable in different conditions. Two sensors are mounted for each wheel. One of the sensors measures the polarity of magnetic tape slices which are stuck on the rim of the wheels with changing polarity. The other sensor is mounted to sense the holes on the brake disc.

The bicycle is equipped with pressure sensors as well. These sensors are connected to the hydraulic block with an adapter block. In the brake system there are four pressure sensors, two for each brake circuit. The test system can measure the pressure applied by the rider from the levers, and also can measure the pressure to the brake-pads.

C. The external controller computer

The external computer is a nano ITX sized SBC (Single Board Computer). It is small PC with, standard interfaces and Windows Embedded Standard 2009 operating system. This computer runs the control algorithm and collects the data from the ECU.

D. Internal and external communication

The controller computer is extended with a high speed CAN interface to communicate with the ECU and the A/D converter of the pressure sensors (*Fig. 5*).

The external communication is implemented as a standard IEEE802.11b/g wireless LAN. For monitoring the behavior of the system and the algorithm, a standard remote desktop connection or a special own, server-client architecture software can be used. With the special software it is possible to monitor the whole CAN communication and data can be displayed and logged in different file formats.

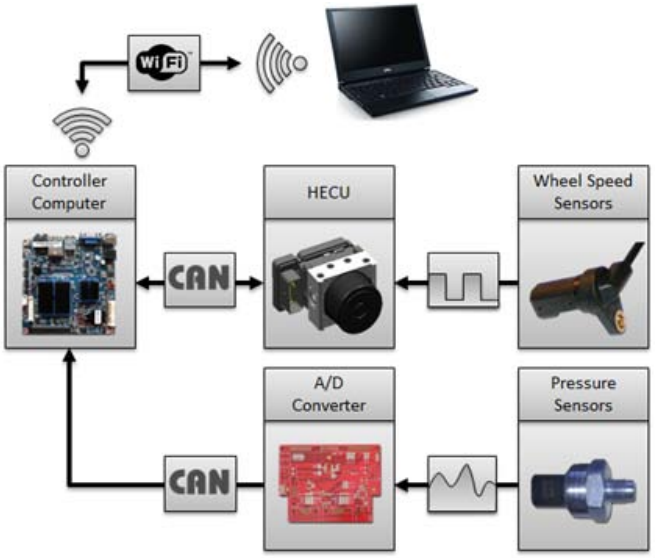

Figure 5: The communication architecture of prototype.

6. The results

The prototype control algorithm was tested on a test track on different surfaces, like asphalt, grassy ground, etc. On the first tests were some efficiency problems but after some fine-tuning of the parameters of the control algorithm (the limits) the results were in concordance with the expectations (*Fig. 6*).

7. The experiences

The current brake system is not capable to support the too often and big pressure changes that are common for motorbikes. For a bicycle brake system this leads to an early wearing of the parts. Thus either the bicycle brake pistons have to be strengthened or an ABS system should be developed that uses analogue valves and applies less pressure “jumps”. As the aim is to keep the original brake system on the bicycle as much as possible the second option is reasonable

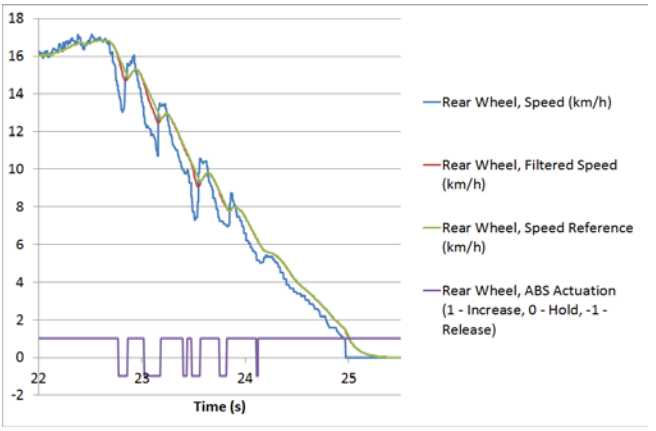

Figure 6: The result of a test (emergency braking with the rear wheel from 18 km/h, on dry asphalt).

8. Conclusion

In many countries in the world a lot of people use bicycle not just for free time activity but also as part of their everyday life to commute to their workplace. During these times accidents can happen to anybody, so it is important to prevent the bicycle riders from injuries. With this prototype the aim of the project team is to show that the ABS technology is also a solution for bicycles. After testing and further improvements of the software should be realized that can help the riders in dangerous situations to mitigate collision or just to stop in a safe way.

The introduction of ABS in car industry at the beginning has some skepticism and now it is a compulsory supplement in every car produced in Europe and America also. The theory of anti-lock braking system is the same for cars and bicycles the circumstances are really different. The point of later development shall be to keep the focus on the helping the rider to run in a safe way. In the future if the development of the bicycle brake assist system evolves as the brake systems for the car, in some-ten years the ABS for high-end bicycles or mopeds will be compulsory also.

The first concept of electrical and hydraulic components are mounted on the bicycle, the control model can be tuned now. In automotive industry the ABS system tuning for a vehicle is a long process based on the experience of the drivers and engineers. For the bicycle it is even more specific because there is no previous test result.

In a later development phase beside ABS other safety and comfort control functions can be added to the system (e.g.: lift-off protection, hold-and-go

function, brake-by-wire) and the development of a smaller more efficient ABS HECU, specialized for bicycles (with new hydraulic, sensor and control unit) was started.

References

[1] Rieth, P. E., Drumm, S. A., Harnishfeger, M., "Electronic Stability Program", in *Electronic Stability Program: The brake that steers*, Landsberg/Lech, Germany, 2002, pp. 54-82.

[2] U.S. Department of Transportation, (2010), Traffic Safety Facts 2009: A Compilation of Motor Vehicle Crash Data from the Fatality Analysis Reporting System and the General Estimates System, National Highway Traffic Safety Administration, Washington, DC 20590, [Online], Available: http://www-nrd.nhtsa.dot.gov/Pubs/811402.pdf

[3] Bauer, R., Steiner, M., (2009, November), Injuries in the European Union: Statistics Summary 2005 – 2007, Kuratorium für Verkehrssicherheit (KfV, Austrian Road Safety Board), Vienna, Austria, [Online], Available: http://ec.europa.eu/health/healthy_environments/docs/ 2009-idb-report_screen.pdf

[4] SWOV, (2012, September), Bicycle helmets. SWOV, Leidschendam, the Netherlands, [Online], Available: http://www.swov.nl/rapport/Factsheets/UK/FS_Bicycle_helmets.pdf

[5] Winck, R., Marek, K., Ngoo, C., (2010), Active Anti-lock Brake System for Low Powered Vehicles Using Cable-Type Brakes, SAE . Warrendale, USA

[6] Astrom, K. J., Klein, R. E., Lennartsson, A., "Bicycle Dynamics and Control: adapted bicycles for education and research," *IEEE Control Systems Magazine*, vol. 25, no. 4, pp. 26-47, Aug., 2005.

[7] Limebeer, D. J. N., Sharp, R. S., "Bicycles, motorcycles, and models," *IEEE Control Systems Magazine*, vol. 26, no. 5, pp. 34-61, Oct., 2006.

[8] Cerone, V., Andreo, D., Larsson, M., Regruto, D., "Stabilization of a Riderless Bicycle," *IEEE Control Systems Magazine*, vol. 30, no. 5, pp. 23-31, Oct., 2010.

[9] Frezza, R., Beghi, A., "A virtual motorcycle driver for closed-loop simulation," *IEEE Control Systems Magazine*, vol. 26, no. 5, pp. 62-77, Oct., 2006.

Acta Universitatis Sapientiae
Electrical and Mechanical Engineering, 4 (2012) 58-69

Development of FPGA Based CAN Bus Error Generator System

Krisztian ENISZ[1], Denes FODOR[1], Balazs NEMETH[2], Ferenc SPEISER[1]

[1] Department of Automotive Mechatronics,
Faculty of Engineering,
University of Pannonia, Veszprem, Hungary,
e-mail: eniszk@almos.uni-pannon.hu
[2] Continental Automotive Hungary Ltd., Veszprem, Hungary

Manuscript received March 15, 2013; revised May 15, 2013

Abstract: This paper introduces the development and architecture of an FPGA based communication error generator system for CAN (Controller Area Network) networks. The created test-system is able to receive and interpret the frames on the network and capable to modify the user specified part of these messages on bit level in real-time. Beside of these modifications the environment has to be feasible to generate physical level error.

Keywords: automotive, CAN, FPGA, error generation

1. Introduction

In a modern vehicle there are more than 40 Electronic Control Units (ECUs) and there are countless sensors and actuators. The communication between these devices is implemented on different types of networks and protocols [1] [2]. In an ordinary car 2-3 different kinds of communication protocols are applied [3]. Most of the electronic control units including the safety critical systems are connected by Controller Area Network (CAN). These safety systems like the anti-lock braking system (ABS) and the electronic stability program (ESP) help to preserve the stability of the vehicle [4]; therefore it is indispensable to test these systems in every respect; including the validation and verification tests of communication.

On an average CAN bus more than 2000 signals and more than 200 frames are transmitted with even 1 Mbit/s baudrate. Hence it can be observed that even a short disturbance or error in the communication can cause large amount of

data loss or corruption. The corrupted or missed data can determine the malfunction of safety critical system that can cause an accident if the ECU is not fault-tolerant.

A standard communication test generally includes the physical and logical test of the transceiver modules of the CAN nodes. The main point of these tests is to examine that the CAN nodes are able to properly create and process the CAN frames and signals and that they can handle the disturbances and errors. If there is no hardware error at CAN nodes, it is not so complicated to test the communication because it is enough to measure the transmission and reception time of the frames and compare the structure and contents of the frames with the expected data. However, the fault insertion is not so simple. The simulation and test environment has to create errors and disturbances in real-time (e.g.: wire break, short circuit, bit level errors) in a reproducible way.

2. Existing systems

There are a few special devices (e.g.: GEMAC (CAN-Bus Tester), IXXAT (CANcheck)) on the market, which make it possible to implement similar tests. These are mostly network testers and analyzers for physical diagnostic of CAN line and communication (e. g. bus state, bus load, monitoring); a few of them are capable to generate network and physical level errors. One of the most popular devices that solves these problems is produced by the Vector company.

The Vector CANstressDR modulates the state of the bus by software tunable electronic components. It is able to emulate bus line errors, disturb the CAN transceiver, create short circuit and wire break etc. This device is a good choice to facilitate the development of ECUs. With these tools it is easy to create a communication test system, but there are some disadvantages e.g. the price of these devices is relatively high and it is hard to adapt these “closed” systems to special tests.

That was the reason why the development of a new communication test system has been started. The creation of a new hardware and software environment is not time and cost efficient [5].

3. Concept

In the modern ECU development methods the cost efficient and thorough testing is very important in order to decrease the possibility of errors. One of the testing procedures is the Hardware In the Loop (HIL) test, which is widely used in different levels of the development to validate the functionalities. For the HIL tests the tested device are generally connected to a high performance real-time system. The main function of the HIL environment is to provide the signals

which are necessary for the ECU to be able to operate and receive the data and signals from the tested device.

The modern multi-functional test environment has different kinds of analog and digital input and output ports and communication interfaces. It can be beneficial to use the existing interfaces to create a communication test system from general purpose test environment, in order to minimize the hardware investment. The other advantage of this concept is that it makes possible to customize the software for special tasks and that it and can be integrated into the different types of tests.

The elaborated test system is based on the PXI platform of National Instruments which is originally built for HIL testing of ECU's. The system is equipped with an x86 (x64) processor that is able to execute simulation steps with 1ms cycle time thanks to the Phar Lap real-time operating system.

The special high speed real-time controlling, data acquisition, signal processing tasks are executed by the FPGA based analogue and digital I/O modules. These modules are freely reconfigurable using the NI LabVIEW graphical programming environment and the FPGA is able to act as an individual processing unit. The system is also equipped with CAN, LIN, FlexRay and other automotive communication interfaces.

Since it was not the point to develop a generic device like the above mentioned Vector CANstressDR, it was possible to introduce several restrictions in the design phase of the communication test-system. The only requirement was to be able to freely modify the communication both on hardware and software level.

The error-generator environment should meet the following requirements:

- it should be sufficient to modify the messages going towards the tested device;
- the interaction should be invisible for the tested device;
- the message modification, the state change of the communication line should happen in near real-time;
- the collision of the messages before and after the modification is not allowed, the two messages should appear as two separate lines;
- it should be possible to modify any of the bits of the messages;
- it should be able to produce line-cut on any of the CAN lines.

For the error generation on the CAN bus it is necessary to connect the error generator unit to the bus. If the error generator unit is connected in parallel to the bus as a node of the network, then it is not possible to fully manipulate the state of the bus without a special hardware. It is not possible to overwrite the dominant state to recessive in this configuration, because of the structure of the physical layer [1]. Bearing in mind the requirements, a new architecture has

been designed, which is different from the Vector system. While in this case the goal was the communication between the two devices, the solution was to insert the error generator between the devices as a special gateway (*Fig. 1* and *Fig. 2*).

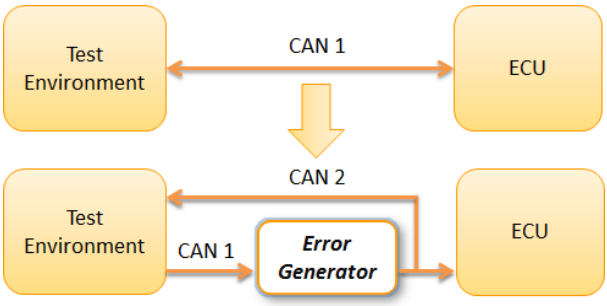

Figure 1: The main concept of the error generator system.

This architecture ensures that the original and the modified messages are available during the test and sending of the original message is not influenced by the error generator system. It is one of the main requirements in respect of the system to realize the message processing and error generation in near real-time. This can be managed by the special FPGA module of the system.

The maximum transmission speed of the CAN bus is 1 Mbit/s. This means that is 1 µsec to receive the actual bit, modify it according to the user demands, store the necessary data and the modifications of it, and transmit it to the tested device.

The computing performance of a general system with x86 (x64) architecture is not enough for the task; only a special, high performance microcontroller, DSP or FPGA is able to manage this complex problem.

4. Implementation

Fig. 2 shows the architecture of the error generator system. The controller of the system is an NI PXIe-8133 embedded controller with extension modules in an NI PXIe-1062Q 8-slot chassis. The NI PXI 8513/2 NI-XNET CAN interface module is responsible for the CAN communication, but the low level frame processing and the error generation is running on a Virtex-5 LX30 high-performance FPGA unit; integrated into a 7851R R series multifunctional reconfigurable I/O module.

Because of the application of the FPGA-based card for the fast processing and pre-processing (e.g.: filtering, signal-level interpretation) it is worth to use the own digital I/O interfaces of the card instead of using the analogue I/O

interfaces with sampling-based signal-level detection. In this way these tasks are managed by the card. The digital I/O interfaces use standard TTL signal levels (0-5V), while the CAN applies differential voltage based physical layer. A CAN transceiver module (ADM3053EBZ) produced by Analog Devices was used to resolve this problem. This device is supposed to do the voltage-level transformation and the galvanic isolation.

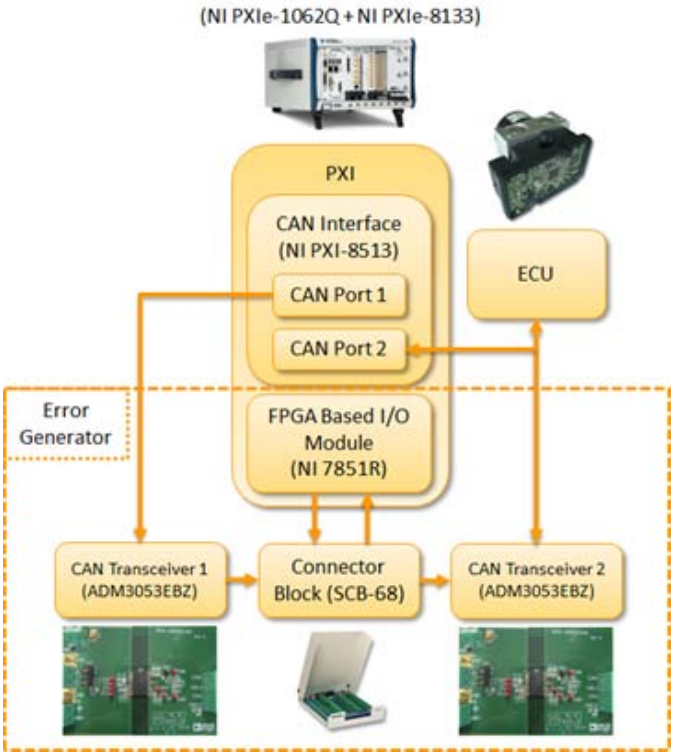

Figure 2: The structure of the error generator system.

At the early stage of development the error generator algorithm was embedded into a LabView FPGA project. The program structure is a kind of state machine that is composed of three main parts. After execution it waits, until the CAN bus comes into idle state, namely there is no communication between the devices on the network. The algorithm starts from this standby state and waits for a valid Start bit of a CAN frame. After the reception of the Start bit, the algorithm steps into the processing and modification state.

For every part of the CAN frame (*Fig. 3*) there are different sub-states (there are 10 different states for the standard frames and 3 additional states for the extended frames). In these sub-states the program receives and processes the

incoming bits, modifies them if it is necessary and forwards the bit. When the reading of all of the bits of the actual frame-state is finished, the program switches to the next state. After the last state the program reinitializes the variables and returns to the waiting state at the beginning. There is a special sub-state, the acknowledgement that is necessary for the smooth communication. During the acknowledgement the sender device releases the bus (sets it to recessive state), and the receiver devices set the bus to dominant state for on bit time long if the frame was read successfully (in case of errorless communication).

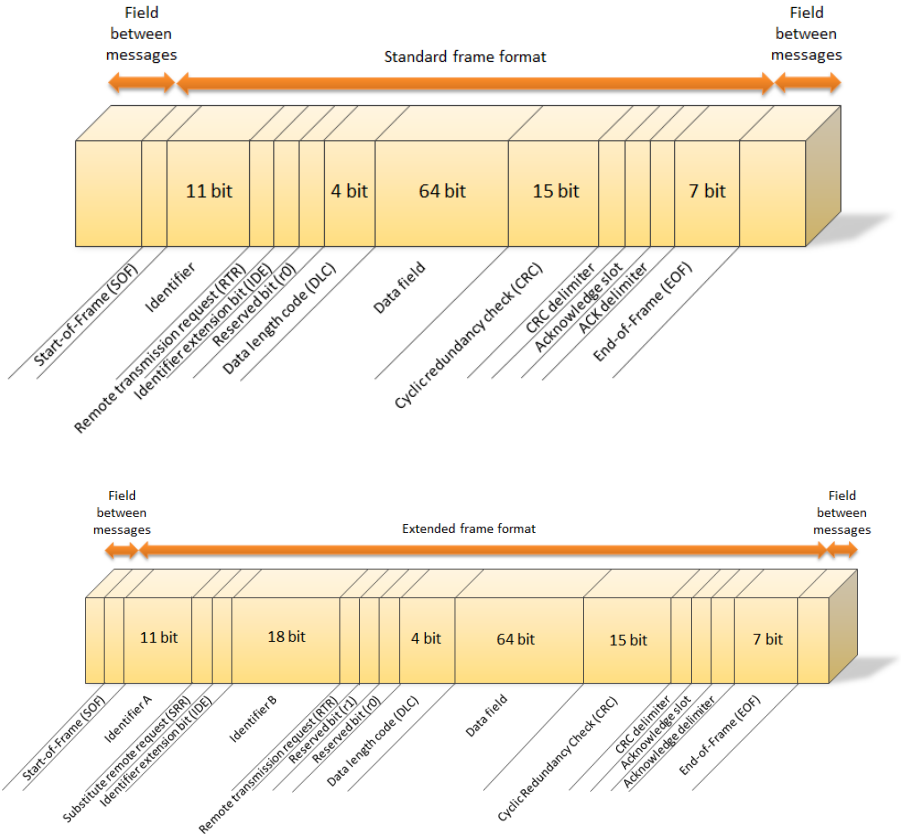

Figure 3: The structure of the standard and of the extended CAN frame.

The exact timing of the sampling point and of the start and end of program states is indispensable for the appropriate operation of the program. This can be managed by the FPGA with a resolution given by its clock period. The control program is complicated because of the applied synchronization process of the

CAN (bit-stuffing). If five bits arrive with identical value, then a bit must be inserted with an opposite value during the transmission. The program is able to identify these inserted bits and throws them away.

Furthermore, in order to meet the preliminary specifications, the program is able to generate physical error (line cut) by cutting both of the lines of the CAN bus separately with the help of a NI 9485 8 channel solid state relay module (placed into the system with the help of an NI 9151 extension chassis).

Fig. 4 below shows the simplified flow-diagram of the program.

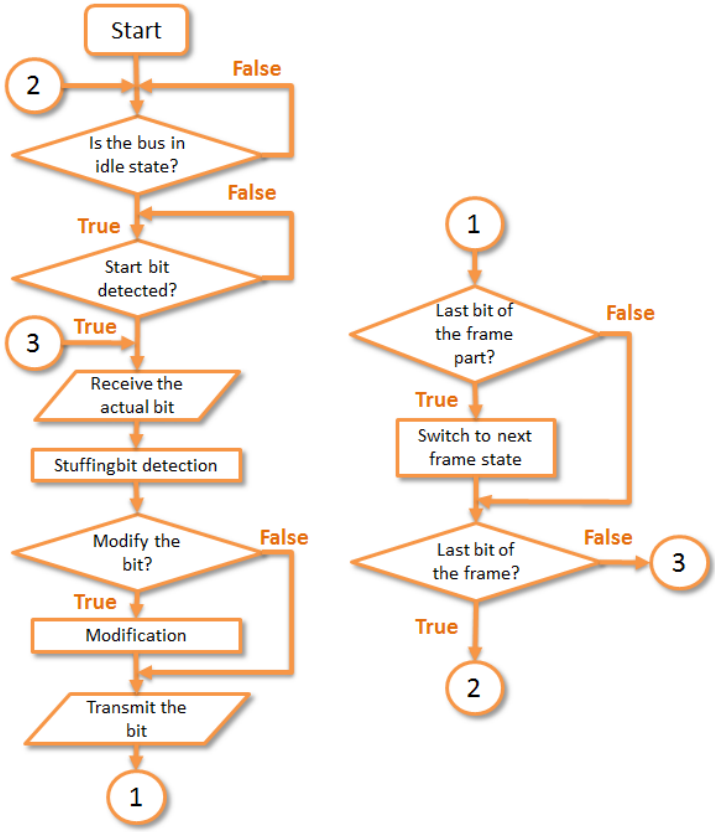

Figure 4: The flow-chart of the error generator program.

In the final development stage, after successful development and implementation of the basic algorithm, the FPGA program was integrated into a higher application layer using National Instruments' VeriStand. The VeriStand is a software interface for real-time testing and simulation applications. VeriStand gives the possibility to make the frame modifications not just

manually but automatically, controlled by a host PC with predefined stimulus-profiles from different test cases. *Fig. 5* shows the final system architecture.

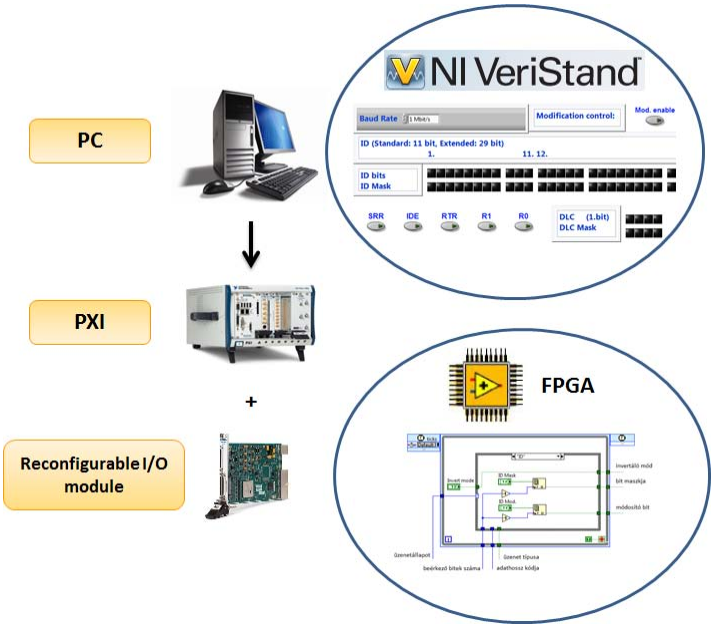

Figure 5: The structure of the system.

The error generator software runs on the reconfigurable FPGA module in the PXI that is controlled by an interface in a VeriStand project on the host PC. The NI VeriStand Real-Time engine implements the communication between the host PC and FPGA module in the PXI.

5. Measurements

One of the main requirements for the system was that it has to be able to modify the CAN frame in a near real-time manner. In order to verify this condition, measurements were made using the elaborated test-system during the development cycle. The goal of the measurements was to define the signal delay that arises from the normal operation of the error generator system. The reason of this delay is that processing and modification of the original frame take some time and the system is able to forward the message only with a small time delay. By minimizing of this latency the near real-time error generation can be achieved. For the CAN protocol the bit-timing is divided into specific sections and the possible place of sampling is also defined.

In order to determine the value of a bit, every CAN device on a network takes samples between the 50% and 80% of the bit-time [6]. It is therefore important to partly overlap the sampling ranges of the bidirectional devices for the shift in-between the signals. In this case the length of the time-shift should be smaller than the half of the bit-time; and the transfer of the bits should be near real time.

During the described measurement, the measurement system consisted of:

- the elaborated error generator system;
- IXXAT Automation GmbH USB-to-CAN Compact (USB-CAN interface);
- Tektronix MSO4054B oscilloscope.

The IXXAT USB-CAN external interface helped with the transmission of the messages intended to be modified. The original and the modified messages were compared by using an oscilloscope to validate the results of the modification and to measure the parameters of the signals.

Fig. 6 shows the modification of the original normal frame message with 71D(hex) identifier to 5D(hex) identifier at the transfer speed of 500 Kbit/s. In the picture the state of the receiver side of the CAN bus (original message) is displayed as yellow, the state of the tested device side CAN bus as cyan (modified message). The VeriStand based user interface is shown as well.

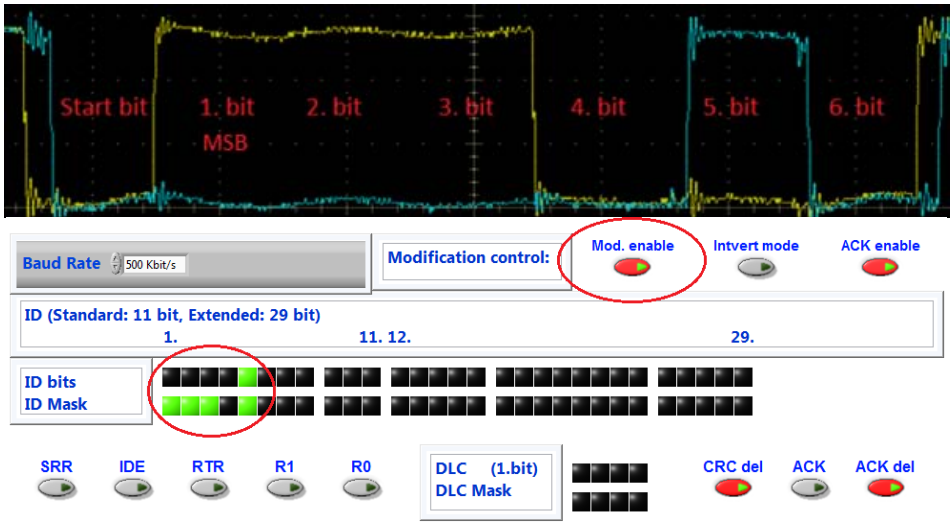

Figure 6: Modification of the message with 71D (hex) identifier.

Table 1 presents the average delays of five measurements resulted at different transfer speeds (the coefficient variation is always smaller than 3%).

Table 1: Signal delay as a function of transfer speed

Transfer speed [Kbit/s]	Signal delay [ns]	Bit-time [ns]	(Signal delay/ Bit-time)·100 [%]
1000	360	1000	36
800	380	1250	30.4
500	440	2000	22
250	526	4000	13.15
125	534	8000	6.675
50	516	20000	2.58
20	526	50000	1.052
10	532	100000	0.532

Based on the data of the table above, it appears that the system meets the requirements for the signal delay [7], while the signal delay is only 36% of the full bit time at 1 Mbit/s transfer speed. Furthermore *Fig. 7* and *Fig. 8* show the oscilloscope screenshots of the signal delays during the measurements at 125 and 500 Kbit/s transfer speeds. The CAN high and CAN low line of the transmitter device (IXXAT) are shown as yellow and blue. The high and low lines of the bus on the output side of the error generator system are shown as purple and blue.

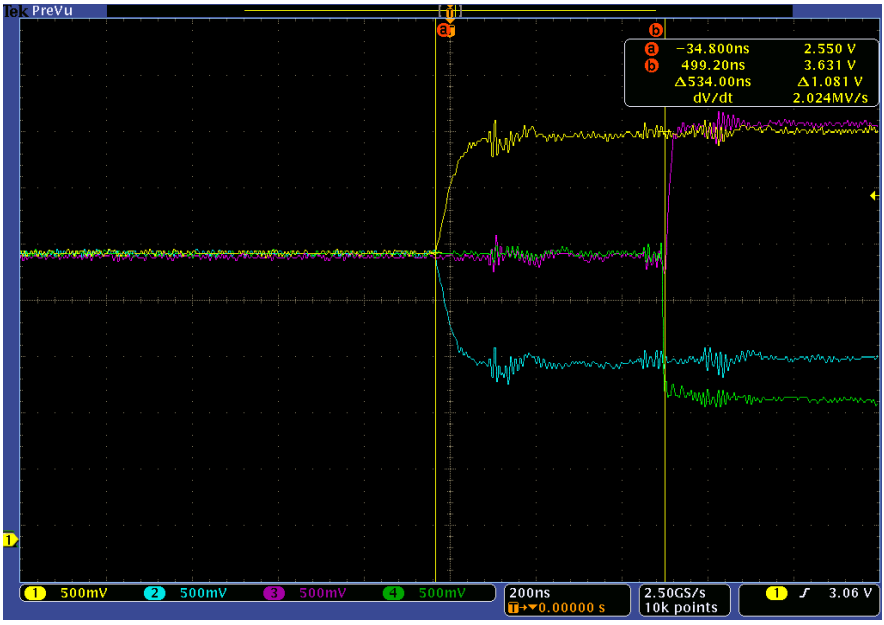

Figure 7: Signal delay at 125 Kbit/s transfer speed (yellow and cyan are the original, magenta and the green are the modified CAN-H and CAN-L lines).

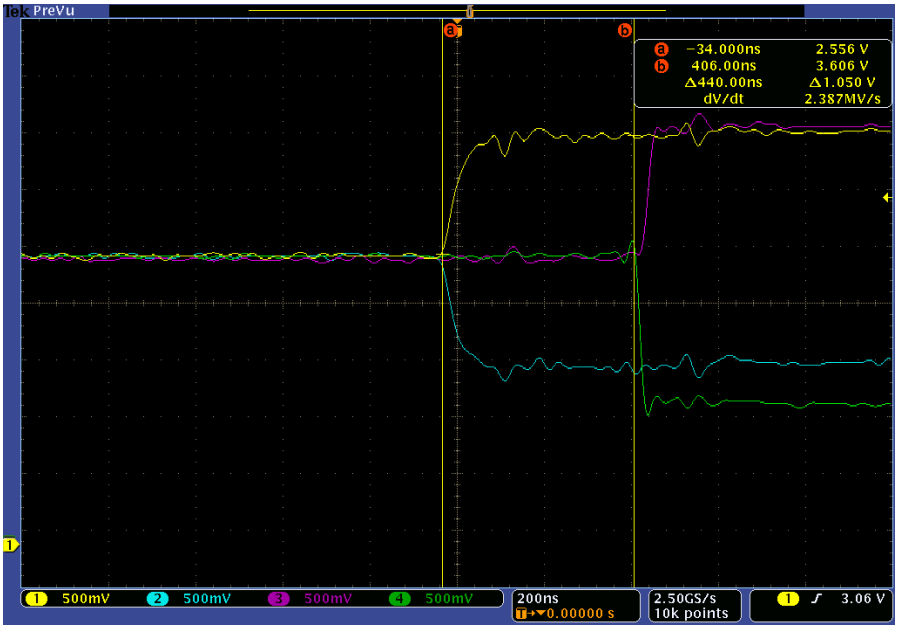

Figure 8: Signal delay at 125 Kbit/s transfer speed (yellow and the cyan are the original, magenta and green are the modified CAN-H and CAN-L lines).

3. Conclusion

During the implementation of the project it had been proven, that a general purpose simulator – thanks to its special features – only by making minimal hardware changes on it can, be suitable to replace a possibly expensive test device.

Furthermore the project came up with a system that is able to receive CAN messages with normal and extended frames in real-time. Any of the bits of the received frames can be inverted or set to a predefined value, while the system bus-speed can be set to the eight most commonly used transmission speeds from 10 Kbit/s up to 1 Mbit/s. According to the test results obtained using a GM ABS ECU, it can be stated that the elaborated system meets the specified requirements.

References

[1] CAN specification version 2.0. Robert Bosch GmbH, Stuttgart, Germany, 1991.
[2] Etschberger, K., "Controller Area Network", in *IXXAT Press*, Weingarten, Germany, 2001.
[3] Nolte, T., Hansson, H., Bello, L. L., G., "Automotive communications-past, current and future", in *IEEE Conference on Emerging Technologies and Factory Automation*, 2005.
[4] Johansson, K. H., Torngren, M., Nielsen, L., "Vehicle Applications of Controller Area Network", in *Springer Control Engineering*, 2005, pp. 741-765.
[5] Novak, J., Fried, A., Vacek, M., "CAN Generator and Error Injector", in *Proceedings of IEEE International Conference on Electronics, Circuits and Systems*, Dubrovnik, Croatia, September 2002, pp. 967-970.
[6] Philips Electronics N. V., "Determination of Bit Timing Parameters for the CAN Controller SJA 1000", in *Application Note AN97046*, 1997.
[7] Novak, J., "New measurement method of sample point position in controller area network nodes", in *Elsevier Measurement*, Vol. 41, Issue 3, April 2008, pp. 300-306

Acta Universitatis Sapientiae
Electrical and Mechanical Engineering, 4 (2012) 70-82

Finite Difference Modeling of Orthotropic Materials

Katalin HARANGUS[1], András KAKUCS[2]

[1]Faculty of Technical and Human Sciences,
Sapientia Hungarian University of Transylvania, Tg. Mureş,
[2]Department of Mechanical Engineering,
Faculty of Technical and Human Sciences,
Sapientia Hungarian University of Transylvania, Tg. Mureş,
e-mail: {katalin; kakucs}@ms.sapientia.ro

Manuscript received March 15, 2013; revised May 15, 2013

Abstract: This paper presents a finite-difference computational method for the integration of differential equations with partial derivatives which describe the plane state of displacement or stress of the anisotropic, orthotropic and isotropic materials. The paper examines the anisotropic case, and the relations can be particularized for isotropic materials.

We start from the classic idea of the Airy stress function. The second order partial derivatives of this describe the stress field, but with the help of the stresses, and with the equations of the material the specific strains can be determined. The disadvantage of using the Airy function is that all the boundary conditions must be given in stresses, because the displacement cannot be expressed in a direct way.

We discovered through analogy, that a "potential function" of the displacement can be used, which makes the prescription of the mixed boundary conditions possible. The partial derivatives of this function give the displacement in the direction of the coordinate axes. The derivatives of the displacement, namely the derivatives of superior order of the function of the displacement give the specific strains, and through the application of the material equations, these derivatives of superior order will lead to the stress field. This, points to the fact that the description of the boundary conditions under the form of prescribed stresses (of the load distribution on the boundary) becomes possible, because there is a direct relation (differential equations) between the displacements and stresses. These relations are estimated with finite differences. The disadvantage of the method is that we can have body forces only in one direction.

Keywords: finite-difference method, plane stress and strain, orthotropic materials

1. Introduction

In the linear elasticity theory it is assumed that the relations between stress and strain are linear. Using matrix formulation, this can be described by the formula (Hooke's law):

$$\{\boldsymbol{\sigma}\} = [\boldsymbol{E}] \cdot \{\boldsymbol{\varepsilon}\}, \tag{1}$$

where $\{\boldsymbol{\sigma}\} = [\sigma_x \ \sigma_y \ \sigma_z \ \tau_{xy} \ \tau_{yz} \ \tau_{zx}]^{\mathrm{T}}$ and $\{\boldsymbol{\varepsilon}\} = [\varepsilon_x \ \varepsilon_y \ \varepsilon_z \ \gamma_{xy} \ \gamma_{yz} \ \gamma_{zx}]^{\mathrm{T}}$ contain each 6 components of the stress, respectively of the strain, and $[\boldsymbol{E}]$ is the 6-by-6 elasticity matrix, which contains material constants [9].

For orthotropic materials in plane stress state, the matrix value $[\boldsymbol{E}]$ has the following form [5], [6]:

$$[\boldsymbol{E}] = \begin{bmatrix} \dfrac{E_x}{1-\mu_{xy}\cdot\mu_{yx}} & \dfrac{\mu_{xy}\cdot E_y}{1-\mu_{xy}\cdot\mu_{yx}} & 0 \\ \dfrac{\mu_{yx}\cdot E_x}{1-\mu_{xy}\cdot\mu_{yx}} & \dfrac{E_y}{1-\mu_{xy}\cdot\mu_{yx}} & 0 \\ 0 & 0 & G_{xy} \end{bmatrix}, \tag{2}$$

and for plane strain state, as follows:

$$[\boldsymbol{E}] = \begin{bmatrix} \dfrac{E_x\cdot(1-\mu_{yz}\cdot\mu_{zy})}{\delta} & \dfrac{E_x\cdot(\mu_{yx}+\mu_{zx}\cdot\mu_{yz})}{\delta} & 0 \\ \dfrac{E_y\cdot(\mu_{xy}+\mu_{xz}\cdot\mu_{zy})}{\delta} & \dfrac{E_y\cdot(1-\mu_{xz}\cdot\mu_{zx})}{\delta} & 0 \\ 0 & 0 & G_{xy} \end{bmatrix}, \tag{3}$$

where

$$\delta = 1-\mu_{xy}\cdot\mu_{yx}-\mu_{yz}\cdot\mu_{zy}-\mu_{zx}\cdot\mu_{xz}-\mu_{xy}\cdot\mu_{yz}\cdot\mu_{zx}-\mu_{yx}\cdot\mu_{zy}\cdot\mu_{xz}. \tag{4.a}$$

In these formulae E_i are the Young's moduli and μ_{ij} are the Poisson's ratios, each defined in the directions of the used coordinate system. The shear modulus can be expressed as

$$G_{xy} = G_{yx} = \frac{E_x \cdot E_y}{E_x \cdot (1+\mu_{yx}) + E_y \cdot (1+\mu_{xy})}, \tag{4.b}$$

and there exists a compatibility equation

$$\mu_{yx} \cdot E_x = \mu_{xy} \cdot E_y, \tag{4.c}$$

so in the plane case we have only three independent material constants and both (2) and (3) are symmetric.

The two elasticity matrices $[\boldsymbol{E}]$ of above are valid only if the directions of orthotropy coincide with the directions of the coordinate axes. Otherwise, these must be rotated with the angle θ, that is measured from the first direction of the orthotropy 1 to the used x axis. This transformation leads to a full matrix [5]:

$$[\boldsymbol{E}] = \begin{bmatrix} \overline{E}_{11} & \overline{E}_{12} & \overline{E}_{13} \\ \overline{E}_{21} & \overline{E}_{22} & \overline{E}_{23} \\ \overline{E}_{31} & \overline{E}_{32} & \overline{E}_{33} \end{bmatrix}, \tag{5}$$

of which components are:

$$\begin{aligned}
\overline{E}_{11} &= E_{11} \cdot \cos^4\theta + E_{22} \cdot \sin^4\theta + (E_{12} + E_{21} + 4 \cdot E_{33}) \cdot \sin^2\theta \cdot \cos^2\theta, \\
\overline{E}_{12} &= E_{12} \cdot \cos^4\theta + E_{21} \cdot \sin^4\theta + (E_{11} + E_{22} - 4 \cdot E_{33}) \cdot \sin^2\theta \cdot \cos^2\theta, \\
\overline{E}_{13} &= (E_{11} - E_{12} - 2 \cdot E_{33}) \cdot \sin\theta \cdot \cos^3\theta + (E_{21} - E_{22} + 2 \cdot E_{33}) \cdot \sin^3\theta \cdot \cos\theta, \\
\overline{E}_{21} &= E_{12} \cdot \sin^4\theta + E_{21} \cdot \cos^4\theta + (E_{11} + E_{22} - 4 \cdot E_{33}) \cdot \sin^2\theta \cdot \cos^2\theta, \\
\overline{E}_{22} &= E_{11} \cdot \sin^4\theta + E_{22} \cdot \cos^4\theta + (E_{21} + E_{12} + 4 \cdot E_{33}) \cdot \sin^2\theta \cdot \cos^2\theta, \\
\overline{E}_{23} &= (E_{11} - E_{12} - 2 \cdot E_{33}) \cdot \sin^3\theta \cdot \cos\theta + (E_{21} - E_{22} + 2 \cdot E_{33}) \cdot \sin\theta \cdot \cos^3\theta, \\
\overline{E}_{31} &= (E_{11} - E_{21} - 2 \cdot E_{33}) \cdot \sin\theta \cdot \cos^3\theta + (E_{12} - E_{22} + 2 \cdot E_{33}) \cdot \sin^3\theta \cdot \cos\theta, \\
\overline{E}_{32} &= (E_{11} - E_{21} - 2 \cdot E_{33}) \cdot \sin^3\theta \cdot \cos\theta + (E_{12} - E_{22} + 2 \cdot E_{33}) \cdot \sin\theta \cdot \cos^3\theta, \\
\overline{E}_{33} &= (E_{11} - E_{12} - E_{21} + E_{22} - 2 \cdot E_{33}) \cdot \sin^2\theta \cdot \cos^2\theta + E_{33} \cdot (\sin^4\theta + \cos^4\theta),
\end{aligned} \tag{6}$$

where E_{ij} are the members of the $[\boldsymbol{E}]$ elasticity matrix (eq. 2 or 3).

Therefore, when the directions of orthotrophy do not coincide with the use coordinate axes, the elasticity matrix contains nine nonzero elements (but only three independent ones) and it is symmetric ($\overline{E}_{ij} = \overline{E}_{ji}$). In the general case of plane anisotropy, the elasticity matrix is also full and symmetric, but now it contains six independent elements.

2. Formulation for finite-difference solution

Starting from the idea of Airy stress function, let us suppose that in the case of orthotropic materials there is a function $\Psi(x,y)$ of which partial derivatives give the projections of the displacement as it follows [7]:

$$\begin{aligned} u &= \alpha_1 \cdot \frac{\partial^2 \Psi}{\partial x^2} + \alpha_2 \cdot \frac{\partial^2 \Psi}{\partial x \cdot \partial y} + \alpha_3 \cdot \frac{\partial^2 \Psi}{\partial y^2}, \\ v &= \alpha_4 \cdot \frac{\partial^2 \Psi}{\partial x^2} + \alpha_5 \cdot \frac{\partial^2 \Psi}{\partial x \cdot \partial y} + \alpha_6 \cdot \frac{\partial^2 \Psi}{\partial y^2}, \end{aligned} \tag{7}$$

where u is the projection on the x axis, respectively v on the y axis, and the α_i are some coefficients to be determined. It can be shown that the (7) relations satisfy the compatibility equations of the strains

$$\frac{\partial^2 \varepsilon_x}{\partial y^2} + \frac{\partial^2 \varepsilon_y}{\partial x^2} - \frac{\partial^2 \gamma_{xy}}{\partial x \cdot \partial y} = 0\,. \tag{8}$$

We transcribe the

$$\frac{\partial \sigma_x}{\partial x} + \frac{\partial \tau_{xy}}{\partial y} + f_x = 0, \qquad \frac{\partial \sigma_y}{\partial y} + \frac{\partial \tau_{yx}}{\partial x} + f_y = 0 \tag{9}$$

equilibrium equations using Hooke's law in strains, considering that the $\boldsymbol{f}$ body force has only vertical component ($f_x = 0$):

$$\begin{aligned} &\frac{\partial (E_{11} \cdot \varepsilon_x + E_{12} \cdot \varepsilon_y + E_{13} \cdot \gamma_{xy})}{\partial x} + \frac{\partial (E_{31} \cdot \varepsilon_x + E_{32} \cdot \varepsilon_y + E_{33} \cdot \gamma_{xy})}{\partial y} = 0, \\ &\frac{\partial (E_{21} \cdot \varepsilon_x + E_{22} \cdot \varepsilon_y + E_{23} \cdot \gamma_{xy})}{\partial y} + \frac{\partial (E_{31} \cdot \varepsilon_x + E_{32} \cdot \varepsilon_y + E_{33} \cdot \gamma_{xy})}{\partial x} + f_y = 0. \end{aligned} \tag{10}$$

Then with the

$$\varepsilon_x = \frac{\partial u}{\partial x}, \quad \varepsilon_y = \frac{\partial v}{\partial y}, \quad \gamma_{xy} = \frac{\partial v}{\partial x} + \frac{\partial u}{\partial y}, \tag{11}$$

geometrical equations, using the (7) expressions of the displacements, we obtain the followings:

$$
\begin{aligned}
&(\alpha_1 \cdot E_{11} + \alpha_4 \cdot E_{13}) \cdot \frac{\partial^4 \Psi}{\partial x^4} + \\
&+(\alpha_1 \cdot E_{13} + \alpha_1 \cdot E_{31} + \alpha_2 \cdot E_{11} + \alpha_4 \cdot E_{12} + \alpha_4 \cdot E_{33} + \alpha_5 \cdot E_{13}) \cdot \frac{\partial^4 \Psi}{\partial x^3 \cdot \partial y} + \\
&+(\alpha_1 \cdot E_{33} + \alpha_2 \cdot E_{13} + \alpha_2 \cdot E_{31} + \alpha_3 \cdot E_{11} + \\
&\quad +\alpha_4 \cdot E_{32} + \alpha_5 \cdot E_{12} + \alpha_5 \cdot E_{33} + \alpha_6 \cdot E_{13}) \cdot \frac{\partial^4 \Psi}{\partial x^2 \cdot \partial y^2} + \\
&+(\alpha_2 \cdot E_{33} + \alpha_3 \cdot E_{13} + \alpha_3 \cdot E_{31} + \alpha_5 \cdot E_{32} + \alpha_6 \cdot E_{12} + \alpha_6 \cdot E_{33}) \cdot \frac{\partial^4 \Psi}{\partial x \cdot \partial y^3} + \\
&+(\alpha_3 \cdot E_{33} + \alpha_6 \cdot E_{32}) \cdot \frac{\partial^4 \Psi}{\partial y^4} = 0,
\end{aligned}
\tag{12}
$$

$$
\begin{aligned}
&(\alpha_1 \cdot E_{31} + \alpha_4 \cdot E_{33}) \cdot \frac{\partial^4 \Psi}{\partial x^4} + \\
&+(\alpha_1 \cdot E_{21} + \alpha_1 \cdot E_{33} + \alpha_2 \cdot E_{31} + \alpha_4 \cdot E_{23} + \alpha_4 \cdot E_{32} + \alpha_5 \cdot E_{33}) \cdot \frac{\partial^4 \Psi}{\partial x^3 \cdot \partial y} + \\
&+(\alpha_1 \cdot E_{23} + \alpha_2 \cdot E_{21} + \alpha_2 \cdot E_{33} + \alpha_3 \cdot E_{31} + \\
&\quad +\alpha_4 \cdot E_{22} + \alpha_5 \cdot E_{23} + \alpha_5 \cdot E_{32} + \alpha_6 \cdot E_{33}) \cdot \frac{\partial^4 \Psi}{\partial x^2 \cdot \partial y^2} + \\
&+(\alpha_2 \cdot E_{23} + \alpha_3 \cdot E_{21} + \alpha_3 \cdot E_{33} + \alpha_5 \cdot E_{22} + \alpha_6 \cdot E_{23} + \alpha_6 \cdot E_{32}) \cdot \frac{\partial^4 \Psi}{\partial x \cdot \partial y^3} + \\
&+(\alpha_3 \cdot E_{23} + \alpha_6 \cdot E_{22}) \cdot \frac{\partial^4 \Psi}{\partial y^4} + f_y = 0.
\end{aligned}
\tag{13}
$$

We wish to determine the α coefficients in such manner to get all multipliers of the partial derivatives of the first equation equal to zero. In this case any function Ψ is a solution of the first equation (12):

$$
\begin{aligned}
&\alpha_1 \cdot E_{11} + \alpha_4 \cdot E_{13} = 0 \\
&\alpha_1 \cdot E_{13} + \alpha_1 \cdot E_{31} + \alpha_2 \cdot E_{11} + \alpha_4 \cdot E_{12} + \alpha_4 \cdot E_{33} + \alpha_5 \cdot E_{13} = 0 \\
&\alpha_1 \cdot E_{33} + \alpha_2 \cdot E_{13} + \alpha_2 \cdot E_{31} + \alpha_3 \cdot E_{11} + \alpha_4 \cdot E_{32} + \alpha_5 \cdot E_{12} + \alpha_5 \cdot E_{33} + \alpha_6 \cdot E_{13} = 0 \\
&\alpha_2 \cdot E_{33} + \alpha_3 \cdot E_{13} + \alpha_3 \cdot E_{31} + \alpha_5 \cdot E_{32} + \alpha_6 \cdot E_{12} + \alpha_6 \cdot E_{33} = 0 \\
&\alpha_3 \cdot E_{33} + \alpha_6 \cdot E_{32} = 0.
\end{aligned}
\tag{14}
$$

Since six coefficients cannot be determined from these five equations, we must prescribe one of the values [1]. Therefore, we assign $\alpha_2 = 1$, and the five

remaining coefficients are found by solving the system of equations (14). This can be resolved using numerical methods. With the obtained α coefficients the second equilibrium equation (13) became:

$$\beta_1 \cdot \frac{\partial^4 \Psi}{\partial x^4} + \beta_2 \cdot \frac{\partial^4 \Psi}{\partial x^3 \cdot \partial y} + \beta_3 \cdot \frac{\partial^4 \Psi}{\partial x^2 \cdot \partial y^2} + \beta_4 \cdot \frac{\partial^4 \Psi}{\partial x \cdot \partial y^3} + \beta_5 \cdot \frac{\partial^4 \Psi}{\partial y^4} = \beta_0 \cdot f_y, \quad (15)$$

of which solution is the potential function sought by us. The coefficients of this equation are:

$$\begin{aligned}
\beta_1 &= \alpha_1 \cdot E_{31} + \alpha_4 \cdot E_{33}, \\
\beta_2 &= \alpha_1 \cdot (E_{21} + E_{33}) + \alpha_2 \cdot E_{31} + \alpha_4 \cdot (E_{23} + E_{32}) + \alpha_5 \cdot E_{33}, \\
\beta_3 &= \alpha_1 \cdot E_{23} + \alpha_2 \cdot (E_{21} + E_{33}) + \alpha_3 \cdot E_{31} + \alpha_4 \cdot E_{22} + \alpha_5 \cdot (E_{23} + E_{32}) + \alpha_6 \cdot E_{33}, \\
\beta_4 &= \alpha_2 \cdot E_{23} + \alpha_3 \cdot (E_{21} + E_{33}) + \alpha_5 \cdot E_{22} + \alpha_6 \cdot (E_{23} + E_{32}), \\
\beta_5 &= \alpha_3 \cdot E_{23} + \alpha_6 \cdot E_{22}, \\
\beta_0 &= -1.
\end{aligned} \quad (16)$$

When the orthotropy directions coincide with the x and y axes, the expressions of coefficients β_i are simpler: if the angle θ is an integer multiple of the right angle, the coefficients β_2 and β_4 are equal to zero. In case of isotropic materials the relations will be more simplified. For isotropic materials, when $f_y = 0$, the equation (13) becomes biharmonic.

The problem is ultimately reduced to solving the equation (15): we propose a method using finite differences. If the partial derivatives of the equation are replaced by centered finite differences, we achieve the molecule presented in *Fig. 1*. Therefore, in the (i, j) node of the grid we can write the following equation:

	$-2 \cdot h$	$-h$	0	h	$2 \cdot h$
$2 \cdot k$		$-\frac{\beta_4}{4 \cdot h \cdot k^3}$	$\frac{\beta_5}{k^4}$	$\frac{\beta_4}{4 \cdot h \cdot k^3}$	
k	$-\frac{\beta_2}{4 \cdot h^3 \cdot k}$	$\frac{\beta_2}{2 \cdot h^3 \cdot k} + \frac{\beta_3}{h^2 \cdot k^2} + \frac{\beta_4}{2 \cdot h \cdot k^3}$	$-2 \cdot \frac{\beta_3}{h^2 \cdot k^2} - 4 \cdot \frac{\beta_5}{k^4}$	$-\frac{\beta_2}{2 \cdot h^3 \cdot k} + \frac{\beta_3}{h^2 \cdot k^2} - \frac{\beta_4}{2 \cdot h \cdot k^3}$	$\frac{\beta_2}{4 \cdot h^3 \cdot k}$
0	$\frac{\beta_1}{h^4}$	$-4 \cdot \frac{\beta_1}{h^4} - 2 \cdot \frac{\beta_3}{h^2 \cdot k^2}$	$6 \cdot \frac{\beta_1}{h^4} + 4 \cdot \frac{\beta_3}{h^2 \cdot k^2} + 6 \cdot \frac{\beta_5}{k^4}$	$-4 \cdot \frac{\beta_1}{h^4} - 2 \cdot \frac{\beta_3}{h^2 \cdot k^2}$	$\frac{\beta_1}{h^4}$
$-k$	$\frac{\beta_2}{4 \cdot h^3 \cdot k}$	$-\frac{\beta_2}{2 \cdot h^3 \cdot k} + \frac{\beta_3}{h^2 \cdot k^2} - \frac{\beta_4}{2 \cdot h \cdot k^3}$	$-2 \cdot \frac{\beta_3}{h^2 \cdot k^2} - 4 \cdot \frac{\beta_5}{k^4}$	$\frac{\beta_2}{2 \cdot h^3 \cdot k} + \frac{\beta_3}{h^2 \cdot k^2} + \frac{\beta_4}{2 \cdot h \cdot k^3}$	$-\frac{\beta_2}{4 \cdot h^3 \cdot k}$
$-2 \cdot k$		$\frac{\beta_4}{4 \cdot h \cdot k^3}$	$\frac{\beta_5}{k^4}$	$-\frac{\beta_4}{4 \cdot h \cdot k^3}$	

Figure 1: The approximation with finite-difference method of the equation (15).

$$\frac{\beta_4}{4\cdot h\cdot k^3}\cdot\Psi(i-1,j-2)+\frac{\beta_5}{k^4}\cdot\Psi(i,j-2)-\frac{\beta_4}{4\cdot h\cdot k^3}\cdot\Psi(i+1,j-2)+$$
$$+\frac{\beta_2}{4\cdot h^3\cdot k}\cdot\Psi(i-2,j-1)-\left(\frac{\beta_2}{2\cdot h^3\cdot k}-\frac{\beta_3}{h^2\cdot k^2}+\frac{\beta_4}{2\cdot h\cdot k^3}\right)\cdot\Psi(i-1,j-1)-$$
$$-\left(2\cdot\frac{\beta_3}{h^2\cdot k^2}+4\cdot\frac{\beta_5}{k^4}\right)\cdot\Psi(i,j-1)+\left(\frac{\beta_2}{2\cdot h^3\cdot k}+\frac{\beta_3}{h^2\cdot k^2}+\frac{\beta_4}{2\cdot h\cdot k^3}\right)\cdot\Psi(i+1,j-1)-$$
$$-\frac{\beta_2}{4\cdot h^3\cdot k}\cdot\Psi(i+2,j-1)+\frac{\beta_1}{h^4}\cdot\Psi(i-2,j)-\left(4\cdot\frac{\beta_1}{h^4}+2\cdot\frac{\beta_3}{h^2\cdot k^2}\right)\cdot\Psi(i-1,j)+$$
$$+\left(6\cdot\frac{\beta_1}{h^4}+4\cdot\frac{\beta_3}{h^2\cdot k^2}+6\cdot\frac{\beta_5}{k^4}\right)\cdot\Psi(i,j)-\left(4\cdot\frac{\beta_1}{h^4}+2\cdot\frac{\beta_3}{h^2\cdot k^2}\right)\cdot\Psi(i+1,j)+ \qquad (17)$$
$$+\frac{\beta_1}{h^4}\cdot\Psi(i+2,j)-\frac{\beta_2}{4\cdot h^3\cdot k}\cdot\Psi(i-2,j+1)+$$
$$+\left(\frac{\beta_2}{2\cdot h^3\cdot k}+\frac{\beta_3}{h^2\cdot k^2}+\frac{\beta_4}{2\cdot h\cdot k^3}\right)\cdot\Psi(i-1,j+1)-\left(2\cdot\frac{\beta_3}{h^2\cdot k^2}+4\cdot\frac{\beta_5}{k^4}\right)\cdot\Psi(i,j+1)-$$
$$-\left(\frac{\beta_2}{2\cdot h^3\cdot k}-\frac{\beta_3}{h^2\cdot k^2}+\frac{\beta_4}{2\cdot h\cdot k^3}\right)\cdot\Psi(i+1,j+1)+\frac{\beta_2}{4\cdot h^3\cdot k}\cdot\Psi(i+2,j+1)-$$
$$-\frac{\beta_4}{4\cdot h\cdot k^3}\cdot f(i-1,j+2)+\frac{\beta_5}{k^4}\cdot\Psi(i,j+2)+\frac{\beta_4}{4\cdot h\cdot k^3}\cdot\Psi(i,j+2)=-f_y(i,j).$$

At each node of the finite-difference grid, excepting those on the boundary, we write this equation. In these appear the values of the Ψ function taken in the neighbouring nodes, resulting in a system of equations to be solved in the $\Psi(i,j)$ nodal values.

For the boundary points we can't apply the molecule from *Fig. 1*, because in (17) appear values of Ψ in some non-existing external nodes. These values also appear when we apply (17) for the nodes next to the boundary ones: these external nodes define a new virtual boundary beyond the physical one, increasing the number of the unknowns to be determined. It is to note, that the external grid points, situated in the diagonally opposite convex corners, do not belong to this virtual boundary (*Fig. 2*).

The system of equations can be solved only by writing boundary conditions: we will give these conditions in all boundary nodes, as prescribed displacements and loading forces.

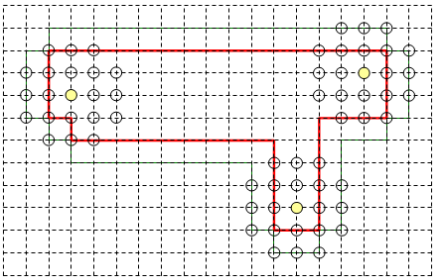

Figure 2: The virtual boundary that appears due to finite-difference approximation.

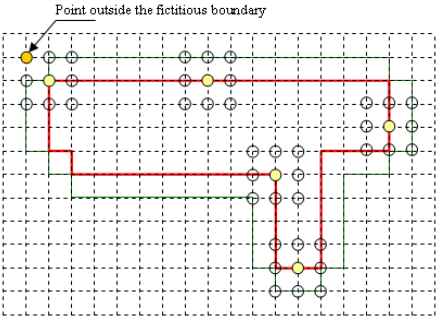

Figure 3: Cells used in approximation of u and v with centered differences.

3. The boundary conditions as prescribed displacements

For easier application of this method, let's approximate the physical boundary with one which is made from horizontal and vertical lines adapted to the grid. In this case we define the boundary conditions as the projections of the displacement, as prescribed values of u and v. According to the relations (7) these projections are obtained by deriving the function Ψ. If we express u from the relation (7) with centered differences, we obtain the molecule from *Fig. 4.* and the following equation:

$$\frac{\alpha_2}{4\cdot h\cdot k}\cdot\Psi(i-1,j-1)+\frac{\alpha_3}{k^2}\cdot\Psi(i,j-1)-\frac{\alpha_2}{4\cdot h\cdot k}\cdot\Psi(i+1,j-1)+$$
$$+\frac{\alpha_1}{h^2}\cdot\Psi(i-1,j)-\left(2\cdot\frac{\alpha_1}{h^2}+2\cdot\frac{\alpha_3}{k^2}\right)\cdot\Psi(i,j)+\frac{\alpha_1}{h^2}\cdot\Psi(i+1,j)- \qquad (18)$$
$$-\frac{\alpha_2}{4\cdot h\cdot k}\cdot\Psi(i-1,j+1)+\frac{\alpha_3}{k^2}\cdot\Psi(i,j+1)+\frac{\alpha_2}{4\cdot h\cdot k}\cdot\Psi(i+1,j+1)=u(i,j).$$

	$-h$	0	h
k	$-\frac{\alpha_2}{4\cdot h\cdot k}$	$\frac{\alpha_3}{k^2}$	$\frac{\alpha_2}{4\cdot h\cdot k}$
0	$\frac{\alpha_1}{h^2}$	$-2\cdot\frac{\alpha_1}{h^2}-2\cdot\frac{\alpha_3}{k^2}$	$\frac{\alpha_1}{h^2}$
$-k$	$\frac{\alpha_2}{4\cdot h\cdot k}$	$\frac{\alpha_3}{k^2}$	$-\frac{\alpha_2}{4\cdot h\cdot k}$

Figure 4: The approximation of the displacements with centered differences.

For v we obtain the same scheme and formula, the index of the α-s have to be increased by 3.

We can observe that applying the molecule for a grid node positioned on the boundary, it will be based on three points that are on the imaginary boundary. Straight edges and concave corners will not raise issues or difficulties, however in the convex corners this scheme would include a point that does not belong to the virtual boundary (*Fig. 3*). In this case instead of centered difference approximation, we apply the derivatives' approximations with the help of forward or backward differences, depending on the corner position (*Fig. 5.* - in this figure **X** denotes the position of the node that does not belong to the virtual boundary).

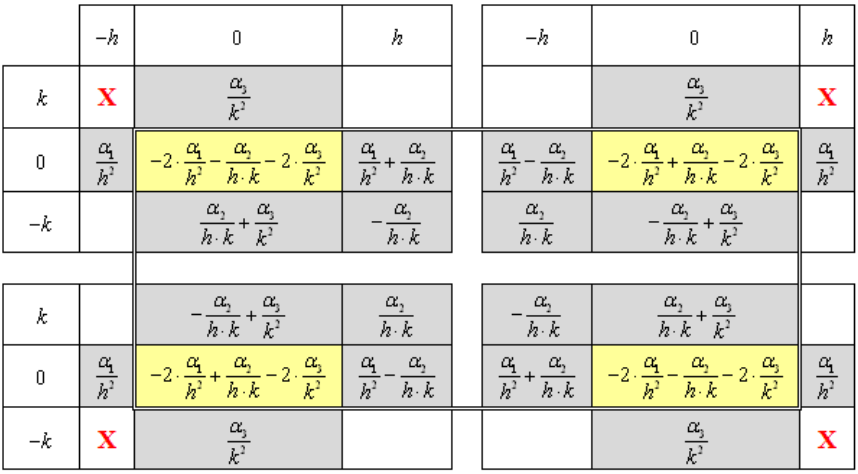

Figure 5: The approximation of displacements in the convex corners (upper left, upper right, lower left and lower right corners; the double line shows the boundary).

4. The boundary conditions as loading

Distributed stress, that loads the boundary is defined by its projections according to *x* and *y* directions, noted as p_x and p_y. These projections generally are described by arbitrary functions. During the grid generation, these functions are replaced by step functions. Concentrated loads also will be replaced by constant distributed loads (*Fig. 6*).

On the loaded sides, we can write some equilibrium equations, those give some relations between external loads and internal stresses (*Fig. 7*).

Using Hooke's law, stresses can be expressed using strains (1), then using the (11) definitions of the strains and the (7) expressions of the displacements we obtain some equations giving stresses as functions of the derivatives of Ψ, e.g. we can write:

$$\begin{aligned}
&\sigma_x = E_{11}\cdot\varepsilon_x + E_{12}\cdot\varepsilon_y + E_{13}\cdot\gamma_{xy} = \\
&= E_{11}\cdot\frac{\partial u}{\partial x} + E_{12}\cdot\frac{\partial v}{\partial y} + E_{13}\cdot\frac{\partial u}{\partial y} + E_{13}\cdot\frac{\partial v}{\partial x} = \\
&= E_{11}\cdot\left(\alpha_1\cdot\frac{\partial^3\Psi}{\partial x^3} + \alpha_2\cdot\frac{\partial^3\Psi}{\partial x^2\cdot\partial y} + \alpha_3\cdot\frac{\partial^3\Psi}{\partial x\cdot\partial y^2}\right) + \\
&+E_{12}\cdot\left(\alpha_4\cdot\frac{\partial^3\Psi}{\partial x^2\cdot\partial y} + \alpha_5\cdot\frac{\partial^3\Psi}{\partial x\cdot\partial y^2} + \alpha_6\cdot\frac{\partial^3\Psi}{\partial y^3}\right) + \\
&+E_{13}\cdot\left(\alpha_1\cdot\frac{\partial^3\Psi}{\partial x^2\cdot\partial y} + \alpha_2\cdot\frac{\partial^3\Psi}{\partial x\cdot\partial y^2} + \alpha_3\cdot\frac{\partial^3\Psi}{\partial y^3}\right) + \\
&+E_{13}\cdot\left(\alpha_4\cdot\frac{\partial^3\Psi}{\partial x^3} + \alpha_5\cdot\frac{\partial^3\Psi}{\partial x^2\cdot\partial y} + \alpha_6\cdot\frac{\partial^3\Psi}{\partial x\cdot\partial y^3}\right) = \\
&= (E_{11}\cdot\alpha_1 + E_{13}\cdot\alpha_4)\cdot\frac{\partial^3\Psi}{\partial x^3} + \\
&+(E_{11}\cdot\alpha_2 + E_{12}\cdot\alpha_4 + E_{13}\cdot\alpha_1 + E_{13}\cdot\alpha_5)\cdot\frac{\partial^3\Psi}{\partial x^2\cdot\partial y} + \\
&+(E_{11}\cdot\alpha_3 + E_{12}\cdot\alpha_5 + E_{13}\cdot\alpha_2 + E_{13}\cdot\alpha_6)\cdot\frac{\partial^3\Psi}{\partial x\cdot\partial y^2} + \\
&+(E_{12}\cdot\alpha_6 + E_{13}\cdot\alpha_3)\cdot\frac{\partial^3\Psi}{\partial y^3}.
\end{aligned} \tag{19}$$

These derivatives can be replaced by finite differences. We will exemplify such boundary conditions for the vertical edge on the left side, as follows:

$$\begin{aligned}
&-\frac{c_4}{2\cdot k^3}\cdot\Psi(j-2,i) - \left(\frac{c_2}{2\cdot h^2\cdot k} + \frac{c_3}{2\cdot h\cdot k^2}\right)\cdot\Psi(j-1,i-1) + \\
&+\left(\frac{c_2}{h^2\cdot k} + \frac{c_4}{k^3}\right)\cdot\Psi(j-1,i) - \left(\frac{c_2}{2\cdot h^2\cdot k} - \frac{c_3}{2\cdot h\cdot k^2}\right)\cdot\Psi(j-1,i+1) +
\end{aligned}$$

$$+\frac{c_3}{h\cdot k^2}\cdot\Psi(j,i-1)-\frac{c_1}{h^3}\cdot\Psi(j,i)+\left(\frac{3\cdot c_1}{h^3}-\frac{c_3}{h\cdot k^2}\right)\cdot\Psi(j,i+1)- \tag{20}$$

$$-\frac{3\cdot c_1}{h^3}\cdot\Psi(j,i+2)+\frac{c_1}{h^3}\cdot\Psi(j,i+3)+\left(\frac{c_2}{2\cdot h^2\cdot k}-\frac{c_3}{2\cdot h\cdot k^2}\right)\cdot\Psi(j+1,i-1)-$$

$$-\left(\frac{c_2}{h^2\cdot k}+\frac{c_4}{k^3}\right)\cdot\Psi(j+1,i)+\left(\frac{c_2}{2\cdot h^2\cdot k}+\frac{c_3}{2\cdot h\cdot k^2}\right)\cdot\Psi(j+1,i+1)+$$

$$+\frac{c_4}{2\cdot k^3}\cdot\Psi(j+2,i)=-p_x,$$

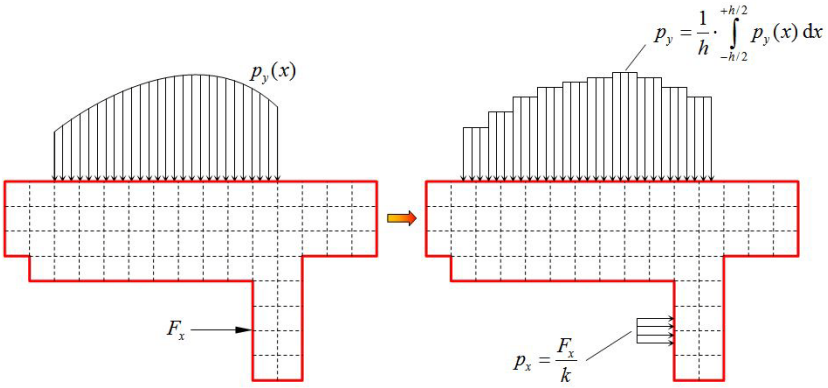

Figure 6: Load replaced by step functions.

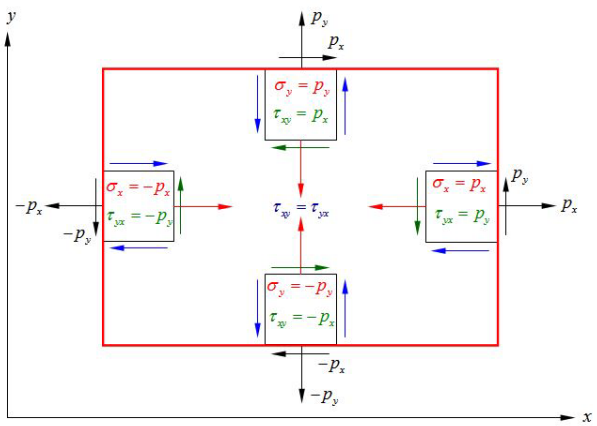

Figure 7: Equilibrium conditions on the boundary.

where

$$\begin{aligned} c_1 &= E_{11}\cdot\alpha_1 + E_{13}\cdot\alpha_4, \\ c_2 &= E_{11}\cdot\alpha_2 + E_{12}\cdot\alpha_4 + E_{13}\cdot\alpha_1 + E_{13}\cdot\alpha_5, \\ c_3 &= E_{11}\cdot\alpha_3 + E_{12}\cdot\alpha_5 + E_{13}\cdot\alpha_2 + E_{13}\cdot\alpha_6, \\ c_4 &= E_{12}\cdot\alpha_6 + E_{13}\cdot\alpha_3. \end{aligned} \tag{21}$$

The corresponding molecule is shown in *Fig. 8.*

	$-h$	0	h	$2\cdot h$	$3\cdot h$
$2\cdot k$		$\frac{c_4}{2\cdot k^3}$			
k	$\frac{c_2}{2\cdot h^2\cdot k}-\frac{c_3}{2\cdot h\cdot k^2}$	$-\frac{c_2}{h^2\cdot k}-\frac{c_4}{k^3}$	$\frac{c_2}{2\cdot h^2\cdot k}+\frac{c_3}{2\cdot h\cdot k^2}$		
0	$\frac{c_3}{h\cdot k^2}$	$-\frac{c_1}{h^3}$	$\frac{3\cdot c_1}{h^3}-\frac{c_3}{h\cdot k^2}$	$-\frac{3\cdot c_1}{h^3}$	$\frac{c_1}{h^3}$
$-k$	$-\frac{c_2}{2\cdot h^2\cdot k}-\frac{c_3}{2\cdot h\cdot k^2}$	$\frac{c_2}{h^2\cdot k}+\frac{c_4}{k^3}$	$-\frac{c_2}{2\cdot h^2\cdot k}+\frac{c_3}{2\cdot h\cdot k^2}$		
$-2\cdot k$		$-\frac{c_4}{2\cdot k^3}$			

Figure 8: The approximation with finite differences method of the equation (20).

If we replace the elements of the matrix of elasticity in relations (21), we obtain the molecules of the stresses σ_y and τ_{xy}, leading to the equations in finite differences of the boundary conditions.

Corner nodes must be treated in different manner: because of the Cauchy-duality of the tangential stresses ($\tau_{xy}=\tau_{yx}$), external loads must be rearranged in such manner as this duality to be satisfied.

5. Conclusions

This paper presents a finite-difference computational method for the integration of differential equations with partial derivatives describing the plane state of displacement or stress of the anisotropic materials. As shown in the paper, the problem can be expressed in stress leading to Airy function, which describes the second order partial differential stress field. With stress and material equations we can determine the specific strains. This method has the disadvantage of the impossibility to express directly the displacements.

By analogy with the Airy function, we used a "potential function" of the displacement, which made it possible to write mixed boundary conditions. The partial derivatives of this function are equal with the displacements in the directions of coordinate axes. Displacement derivatives, as in the derivatives of superior order displacement function give specific strains and by using material equations these superior order derivatives will lead to the stress field. Therefore becomes possible to write outline conditions as distributed load shape, there is a direct relationship (differential equations) between displacements and stresses. These relationships are approximated by finite differences.

In approximation with finite differences the real boundary was replaced by a boundary consisting of horizontal and vertical straight lines and the boundary conditions as prescribed loading led to some equivalence relations between loads and stresses. The denser the grid is, the more accurate the modeling of the load will be and the negative effects of the approximations made in the corner points will be more reduced. The disadvantage of this method is the fact that we can have body forces only in one direction.

References

[1] Ahmed, S. R., Hossain, M. Z., Eddin, M. W., "A general mathematical formulation for finite-difference solution of mixed-boudary-value problems of anisotropic materials", Computer and Structures vol. 83, pp. 35-51, August 2005.

[2] Curtu, I., Ghelmeziu, N., "Mecanica lemnului şi materialelor pe bază de lemn." Bucureşti, Ed. Tehnică, 1984.

[3] Gálfi, B., Száva, I., Kakucs, A., Harangus, K., "Experimental investigation combined with analytical calculus for orthotropic materials mechanical behaviors evaluation." *Ovidius University Annals of Mechanical, Industrial and Maritime Engineering*, vol. 10, tom. 1, pp. 187, 2010.

[4] Kakucs, A., "A végeselem módszer a szerkezetek számításában", Editura Universității Transilvania, 2007.

[5] Kakucs, A., "A végeselem módszer alapjai", Editura Scientia, 2007.

[6] Kakucs, A., Harangus, K., Gálfi, B., "Experiment planning using artificial neural networks", International Conference on Material Science and Engineering, Transilvania University of Braşov, Romania, Bulletin of Transilvania University of Braşov, Supliment BRAMAT, Transilvania University Press, pp. 27, 2007.

[7] Mazilu, P., Țopa, N., Ieremia, M., "Teoria şi calculul plăcilor ortotrope", Editura Tehnică, Bucureşti, 1983.

[8] Szeidl, Gy., Gáspár, Zs., Bojtár, I., "A short introduction to the boundary element method", Braşov, May 5-7, 2010.

[9] Timoshenko, D., Goodier, J. N., "Theory of elasticity", 3rd ed. New York, NY: McGraw-Hill Book Company; 1979.

Acta Universitatis Sapientiae
Electrical and Mechanical Engineering, 4 (2012) 83-95

Electrorheological Fluid Based Brake for Active Physiotherapy Systems

Beniamin CHETRAN, Dan MÂNDRU, Simona NOVEANU,
Olimpiu TĂTAR, Gelu RĂDUCANU

Department of Mechatronics and Machine Dynamics,
Faculty of Mechanics,Technical University of Cluj Napoca,
e-mail: {Dan.Mandru; Beniamin.Chetran; Simona.Noveanu; Olimpiu.Tatar}@mdm.utcluj.ro
e-mail: raducanu.gelu@gmail.com

Manuscript received December 13, 2012; revised May 15, 2013.

Abstract: The paper presents an electrorheological brake developed with the purpose to be used into the structure of rehabilitations wrist systems. A short overview of smart fluids used in systems for physiotherapy is presented to reveal the interest, at global level, for the possibilities of using electro-rheological fluids in such applications. The electrorheological fluid brake design is based on the hydraulic clutch equations and on the previous experimental results. After developing the brake it was tested with commercially available and laboratory developed electrorheological fluids. Results, the control modality and the implementation possibilities into a wrist exerciser are presented.

Keywords: electro-rheological fluids, rehabilitation systems, brake, clutch

1. Operation principle of electro-rheological fluids

The electro-rheological fluids (ERF) are characterized by fast, reversible and controllable changes in rheological properties upon the application of an electric field [1], [2], exhibiting a tunable transition from a liquid state to a solid state. Practically, ERF respond mechanically to an electrical stimulus. This specific behavior gives numerous applications of these fluids in several areas, such as active vibration suppression, motion control and robotic systems, and justifies their framing in the category of so-called smart materials.

Usually, the ERF are suspensions that contain an insulating fluid and particles from one-tenth to hundreds of microns in size, the volume fraction of the particles being from 20% to 80% [3]. According to Fig. 1, the particles arrange themselves as chains along the applied electric field lines, due to an

induced dipole moment. As a consequence, the fluid viscosity and its yield stress change on the order of milliseconds.

The exterior applied electric field leads the transition from a Newtonian liquid (characterized by a linear relationship between shear stress and shear rate) to a non-Newtonian Bingham fluid (characterized by the fact that the yield stress is a function of the electric field) [4].

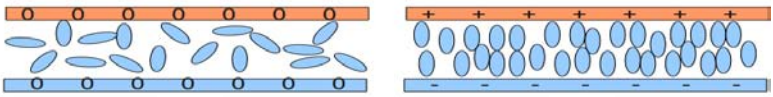

a b

Figure 1: Operation principle of electro-rheological fluids: a – without an applied electric field, b – when an electric field is applied (solid-like state)

Here following fluids are used as dielectric carrier liquid: mineral oil, castor oil, fluoro-silicone oil and silicon oil. The semiconducting solid particles are made of polymer particles, dried aluminosilicate powder, zeolites, $C_6H_{10}O_5$, TiO_2-CeCl3 and $SrTiO_3$/PANI (polyaniline) particles. The inter-electrode gaps are ranged from 0.25 mm to 2.0 mm and placed into an electric field with a strength in the range from 1 kV/mm to 4 kV/mm. This is limited by the breakdown of the dielectric characteristics of the fluid. Maximum yield stress magnitude is typically from 1 to 5 kPa [2].

The most remarkable advantages of ERF are low current density for activation, fast response, long life and wide temperature range of operation, nontoxic and nonpolluting components while the most important disadvantages are: nonlinearity of their behavior, complexity, high voltage to control an ERF based devices and thus high risk concerning safety, high cost and narrow variety of commercially available ERF.

The research of ERF has been in great progress, as well as their applications developed especially for damping and creation of resistive force. By a large variety of exercisers used in rehabilitation processes, the need of greatest interest consists in applying very high resistive forces and torques electrically controlled using small sized and low weighted brakes. The ERF based brakes respond quite well to these requirements.

2. Analysis of some intelligent rehabilitation devices

In order to provide an efficient rehabilitation process, *Rehabilitation Engineering,* that is a component of Biomedical Engineering, proposes simple devices or complex systems, such as prosthetic and orthotic devices, mobility aids, visual and hearing aids, rehabilitation robotics, and others, for a fast and as

more fully reintegration of disabled in family and society [5]. Kinetotherapy is defined as an ensemble of procedures, which promote motion as a basic element of rehabilitation treatment. Often, this kind of rehabilitation approach (that includes walking, running, gym, games, training) must be aided by technical systems and requires different exercisers to support active and passive mobilizations of body segments. Thus, a lot of exercising devices were investigated and many of them are already in use. Some representative examples are presented below.

The device presented in *Fig. 2a* is an exerciser for hand rehabilitation. It is compatible with Functional Magnetic Resonance Imaging Systems (fMR) and uses an ERF brake in order to obtain variable resistance during the kinetic exercises [6].

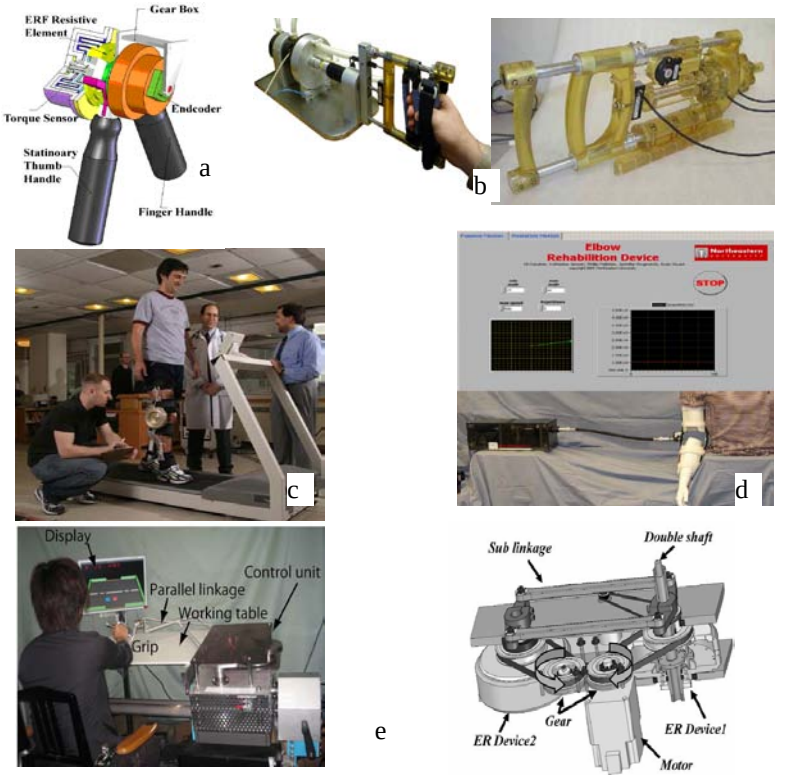

Figure 2: Smart fluids based rehabilitations\devices

According to [7], a hand rehabilitation system combines robotics and interactive gaming for repetitive exercises specific to patients with neurological motor deficits (*Fig. 2b*). It has two degree of freedom for forearm pronation-supination and prehension. Two ERF based actuators drive the system. One

version of this rehabilitation system was developed in order to be fMR compatible [8].

Fig. 2c shows a knee orthotic-type, wearable exerciser equipped with an ERF based variable resistance brake. It is dedicated to iso-inertial, isokinetic and isometric exercising as well as gait retraining [9], [10]. The straps, rigid components, the central hinge mechanism with a connected gear systems and a variable damper are the main components in the structure of this rehabilitation exerciser. Based on the electrically controlled rheological properties of ERF, the brake supplies high resistive and controllable torques.

The transportable elbow rehabilitation device given in *Fig. 2d* responds to passive, active and bracing operation. A DC motor, gearbox, encoder, clutch and brake are located in a portable unit that is attached through a flexible shaft to the elbow brace. This device acts as a smart continuous passive motion machine as well as controlled active rehabilitation system due to the variable resistance applied using the brake based on smart fluids [11].

The active-passive rehabilitation system, called Hybrid-PLEMO is presented in *Fig. 2e* [12]. It is equipped with force sensors on the handle and incremental encoders to determine the handle position. Its user graphical interface enables a visual feedback.

3. Design of ER based brake

The hydraulic clutches are mechanical devices, which use the fluid shear stress in order to transmit rotational movement from the input to the output of the clutch. Basically the hydraulic clutch has two circular parallel discs with a fluid film between them. Depending of the fluid viscosity and the contact areas between discs and fluid, a specific torque can be transmitted. By using an ERF in such structures, the viscosity can be adjusted and with it the transmitted torque, without changing the mechanical structure (*Fig. 3*). New brake types can be designed; using hydraulic clutches structures and smart fluids. The basic configuration is done by fixing the clutch output shaft.

Regarding the practical construction and the torque maximization method, the most desirable structure of an ER fluid brake is the stack discs structure, (*Fig.3c*). The complex electrorheological phenomenon and the complex variable structure of an activated ERF do not permit a practically usable mathematical model. The most devices that imply ERF are developed by means of specific ERF experimental result.

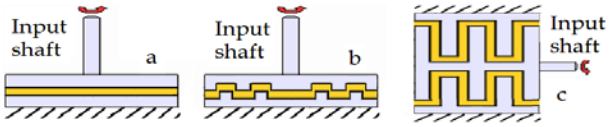

Figure 3: Hydraulic clutch construction types: a-simple discs, b-comb discs, c-stack discs

Assuming that the activated ERF viscosity, at certain field intensity, can be experimentally determined, we propose a simple method to determine the braking torque of a stack discs ERF brake type.

The structure of a stack discs ERF brake (*Fig. 4)* can be characterized by thickness *h*, inner radius R_0 and outer radius R_1. The calculus starts form the shear stress expression of a volume of fluid situated in the gap formed by two parallel plates, one fixed on the rotor and the other welded to the stator body:

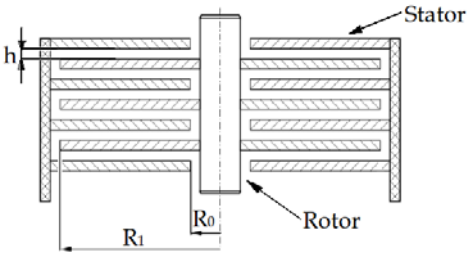

Figure 4: Stack ER fluid brake.

$$\tau = \eta \frac{dv}{dy}. \tag{1}$$

In the following calculus the hypothesis of the Newtonian fluid is accepted. The stream velocity at a radius ρ, $R_0 \le \rho \le R_1$, in dependence with the angular velocity ω can be expressed as $dv = \omega\rho$. Considering the disc gap $dy = h$ the formula (1) of the shear stress becomes:

$$\tau = \eta \frac{\omega\rho}{h}, \text{ where} \tag{2}$$

η is the dynamic viscosity.

For an infinitesimal ring shaped area element built on the circle with the radius ρ, of width dρ, the elementary viscous force expression can be written as

$$\mathrm{d}F = \tau\,\mathrm{d}A = \eta \frac{\omega\rho}{h} 2\pi\rho\,\mathrm{d}\rho = 2\pi\eta \frac{\omega}{h}\rho^2\,\mathrm{d}\rho. \tag{3}$$

With this, the elementary resistant torque developed by the fluid becomes:

$$\mathrm{d}M = \rho\,\mathrm{d}F = 2\pi\eta\frac{\omega}{h}\rho^3\,\mathrm{d}\rho\,. \tag{4}$$

Integrating (4) on the interval of common radiuses the fluid developed torque at one surface of the rotating disc will be:

$$M = \int_{R_0}^{R_1} 2\pi\eta\frac{\omega}{h}\rho^3\,\mathrm{d}\rho = \frac{\pi\eta\omega(R_1{}^4 - R_0^4)}{2h}\,. \tag{5}$$

The average value of the dynamic viscosity can be found from the expression of shear stress (2):

$$\eta = \frac{\tau\cdot h}{\omega\cdot(R_1 - R_0)}\,. \tag{6}$$

The fluid torque developed by all structure theoretically can be computed by multiplying expression (5) with the double of the rotating discs. In the case presented in (*Fig. 3*) the number of surfaces is $2\cdot 3 = 6$.

For a more general consideration equation (5) will turn into:

$$M_{total} = Y\cdot\frac{\pi\eta\omega(R_1{}^4 - R_0^4)}{h} \tag{7}$$

where "*Y*" represents the number of discs in the structure [4].

For developing an ER fluid brake with possibilities to be incorporated into an upper limb exerciser some particularities must be considered:

- Used materials must be excellent dielectrics, in order to electrically isolate the exterior medium by the high voltage inside the brake;
- Miniaturization possibilities;
- The ER fluid brake chassis must be compatible with the exerciser;
- Brake structures must be oil sealed;
- The ER fluid activating electrodes are constituted from the stator discs and rotor discs;
- The rotor shaft is used as electricity charger for rotor discs;
- A boost converter is used as voltage generator in order to activate the fluid.

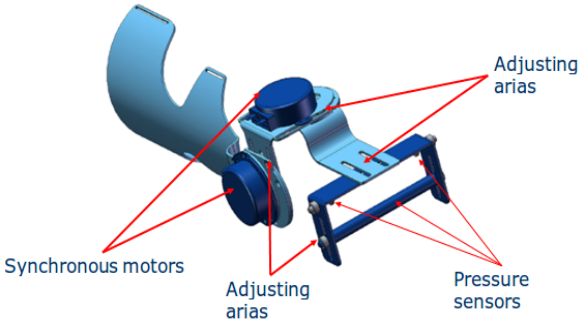

Figure 5: The previous developed wrist exerciser

In our previous work [13], we presented a developed wrist trainer exerciser, with anthropometric adjustment elements, actuated by two 24AC synchronous motors, angular sensors and force sensors (*Fig. 5*).

4. Implementation of the brake on a portable wrist exerciser

The ERF activation is obtained by placing it between two electrostatically charged electrodes. A common method to charge the electrodes is to connect them at a DC voltage source. The required intensity of the electrostatic field that activates the fluid is situated between 2-6 [kV/mm]. The required current depends on the stabilizers used at the fluid composition but because its dielectric nature the current needed has the order of tens of micro-Amperes. In case of overvoltage the fluid dielectric strength is reached, the current starts to flow through the fluid and the electrodes are discharging canceling the particles polarization phenomenon.

When designing voltage sources to activate the ERF some aspects must be considered:

- fluids breaking voltage;
- the electrostatic intensity needed to activate the fluid;
- the gap between the activation electrodes;
- the current should be always continuous;
- the electronic components should be well electric isolated between each other and from exterior medium.

In our previous work we presented a collection of voltage sources that can raise the voltage at the required ERF activation voltage [14].

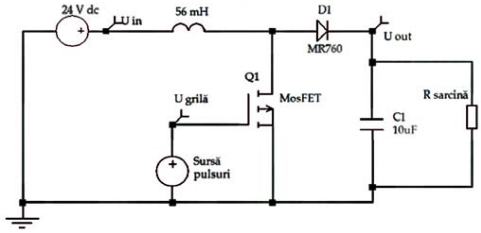

Figure 6: The Boost-Converter

Another modality to obtain the activation required voltage is the boost-converter (*Fig. 6*). This electric source is often utilized into the common step up sources or converters. The electronic components needed to make a boost-converter are: a coil, a power transistor, a high voltage diode and a high voltage capacitor. The components should be chosen for the needed specific voltage. A reliable advantage that boost-converter has it, is represented by the adjustment possibilities. This supply source can be adjusted by modifying the input voltage, the transistor input frequency or by modifying the transistor frequency duty cycle. The calculation of this device is not presented here because it is well treated in different bibliographic sources [15].

In order to control this circuit, between the control circuit board and the boost-converter a galvanic separation stage should be interpolated. This stage is an electronic board including a galvanic separated source, an optotransistor 6N136 and a power transistor driver. This stage is fully adapted for a Pulse Width Modulation control of the power transistor gate. *Figure 7* shows the results of the boost converter output voltage simulations realized in the following variants: adjusting the input voltage (*Fig. 7a*), the transistor frequency for a constant supply voltage (*Fig. 7b*) and the transistor frequency duty cycle also for a constant supply voltage (*Fig. 7c*).

In order to incorporate the structure of ERF brake described at the section 3 (*Fig. 4*) onto the developed exerciser (*Fig. 5*) some aspects were taken into account: the ER brake overall dimension should be compatible with the developed wrist exerciser; the maximum contact surface between the ERF and the activation electrodes should be at least 0.026 [m^2]; the distance between activation electrodes 2 [mm]; the outer brake shell must provide a galvanic separation; avoiding the fluid leakage onto the shaft bearings. The *Fig. 8a* presents an inside view of the developed ERF brake and *Fig. 8b* presents the experimental setup in order to measure the output ERF brake torque. The activation electrodes gap and the contact surface between the electrodes and the ERF were experimentally determined in our previous work by aid of a specially designed experimental stand for ERF study, [16].

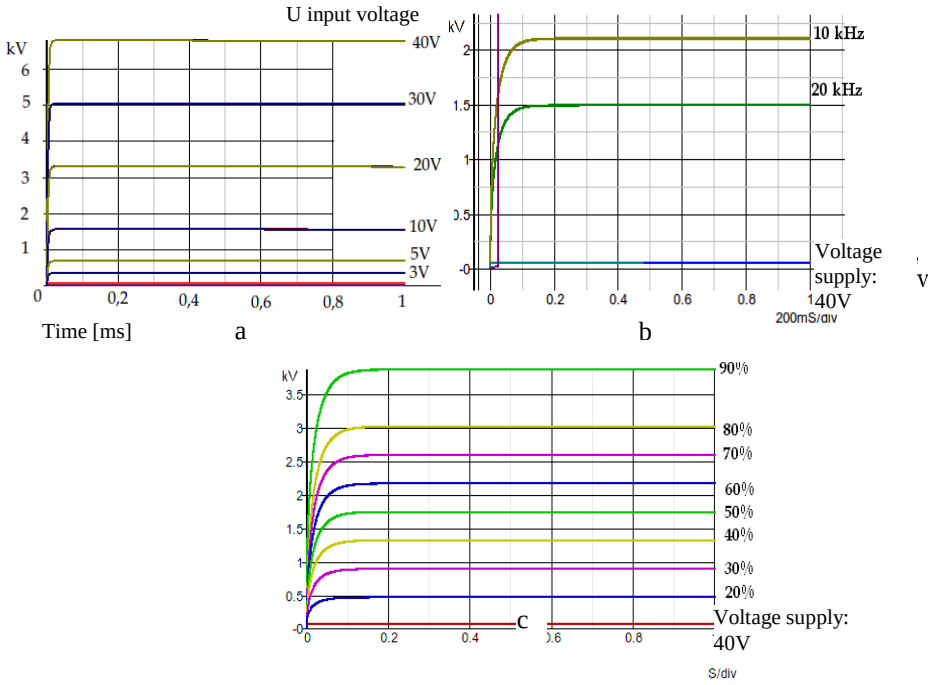

Figure 7: Output voltage by: a – modifying the input voltage; b – modifying the frequency; c – modifying the duty cycle

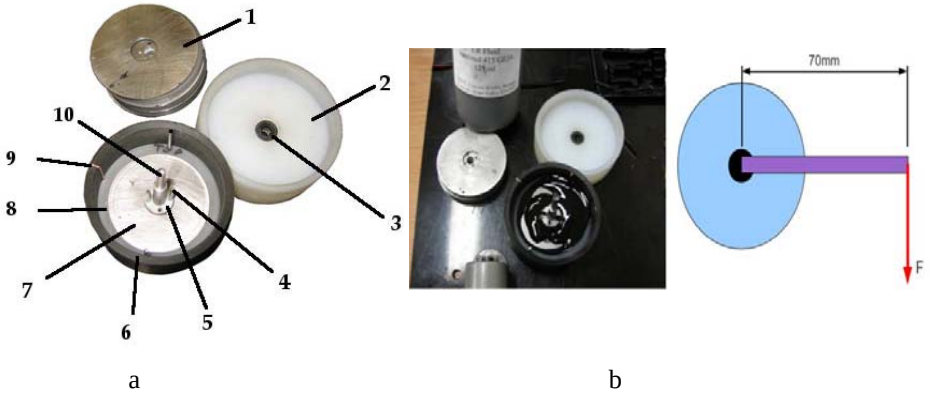

Figure 8: a – The ERF brake: 1-fixed electrodes; 2-top cap; 3-lip sealing; 4-pin; 5-shaft; 6-body; 7-sinning electrodes; 8- fixed spacers; b – ERF brake testing setup

After the practical development of the ERF brake, it was filled with Reslinol 415/GE16 ERF and tested for determining the maximum available torque. The activation voltage was rised at 6.6 [kV], the force was measured with a force sensor and the experimental data was recorded.

The maximum braking torque determined form the measured force is 177.45 [mNm]. This value was compared with the medium torque developed for wrist flexion movement and it was found that the ERF brake torque is big enough to be used in rehabilitation purposes.

The ERF brake was tested also with laboratory developed ERF. These fluids were made up from corn starch and HLP46 hydraulic oil, in different concentrations and the output brake developed forces for different activation voltage were recorded as shown in Table *1.*

Following the forces measurement (*Fig. 9*) the torque was computed and for the 30% corn starch ERF the developed torque at zero field intensity is 45.6 [mNm] and the maximum torque obtained is 74 [mNm] for 1000 [V] activation voltage. For the 80% corn starch ERF the computed torque is 342 [mNm] for zero field intensity and 926 [mNm] for 900 [V] activation voltage, [4].

The developed wrist exerciser can be used in rehabilitation for passive exercises if its elements are actuated by the synchronous motors mounted on the structure or for active with resistance movements if the synchronous motors are replaced with the developed ERF brake *(Fig. 10).* Because the input shaft is used to electrostatically charge the rotor disks it is necessary a galvanic separation between the wrist exerciser structure and the brake shaft. This galvanic separation consists from a dielectric coat that wears the metallic brake shaft.

Table 1: The brake measured values for different corn starch concentrations

Corn starch [%]	Voltage applied [V]	Output Force [N]	Corn starch [%]	Voltage applied [V]	Output Force [N]
30	0	0.8	80	0	6
	450	0.9		450	13.75
	600	1.3		600	16.25
	700	1		700	13.25
	830	1.2		830	15
	900	0.95		900	15.5
	1000	0.9		-	-

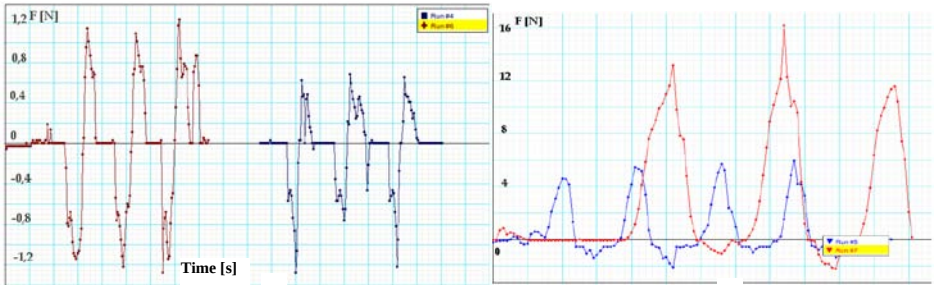

a b

Figure 9: ERF brake output forces for: a-30%; b-80% corn starch fluid

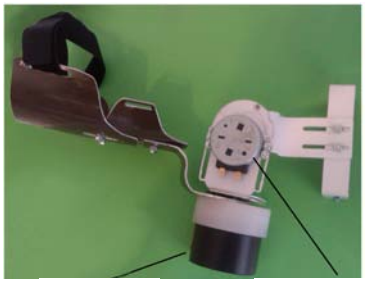

Figure 10: The ERF brake compatibility with the wrist exerciser

5. Conclusions

Due to their property that consists of electroactive changing of their viscosity, the electrorheological fluids have attracted the interest of engineers. These fluids act as simple and rapid-response interfaces between electronic controls and mechanical hardware structures. Besides some explored commercial applications (shock absorbers, clutches, seat dampers, variable flow pumps, earthquake-resistant structures, positioning structures), innovative variable-resistance exercisers were investigated. There is a real need for smart exercising devices whose functional parameters can be rigorously controlled, what it can get through ERF based brakes.

Rotational ERF brakes are developed as the simplest structure of hydraulic clutches and by fixing one of the shafts. The benefit gained is that the ERF clutch or brake has a variable transmitted torque related with the activation

voltage. These ERF clutches/brake stack structure can be easily dimensioned by aid of relations described if the ERF viscosity at different voltages and the maximum torque needed at the output shaft are known.

The most reliable method to control the ERF structures is by using a boost-converter as a power supply. Despite its simplicity this power supply has a control compliance that makes it easy to use for the ERF control.

Based on the described relations and on the previously ERF measurements an ERF brake was developed. The brake was tested with commercially available and laboratory developed ERF. In case of commercially ERF the braking torque domain is reaching the value of 177.45 [mNm] sufficient for wrist physiotherapy exercises. By using laboratory developed ERF the braking domain is smaller and is well influenced by the particles proportion. These laboratories developed ERF can develop necessary braking torques for rehabilitation exercises but need to be changed in accordance with the torque that can be achieve by the patient. The main advantage of the laboratory ERF is the cost price despite of their low torque domain. Usage of commercially ERF extends the torque domain but is more expensive.

ERF brake experimental results shows that the developed structure can be used for active with resistance exercises and its possibility to be incorporated into the structure of the previously developed wrist exerciser.

Acknowledgement

This work is supported by Collaborative Applied Research Project PCCA 180/2012: A hybrid FES - exoskeleton system to rehabilitate the upper limb in disabled people – *EXOSLIM*.

References

[1] Zhang Jian-hua, Design and Preparation of Electrorheological Fluid Materials and Their Rheological Properties and Performance Characteristics, *Journal of Shanghai University*, Vol. 4, No. 3 (Sep. 2000), pp. 243-245.

[2] Pons, Jose L., Emerging actuator technologies – A micromechatronic approach, John Wiley and Sons Ltd, 2005.

[3] Pfeiffer, C., Mavroidis, C., Bar-Cohen, Y., Dolgin, B., "Electrorheological fluid based force feedback device', Proceedings of the 1999 SPIE Telemanipulator and Telepresence Technologies Conference, Boston, 1999, Vol. 3840, pp. 88-99.

[4] Chetran, B., "Studies And Researches Regarding Kinetoterapy Smart Systems", PhD Thesis, Technical University of Cluj-Napoca, 2012.

[5] Mândru, D., Rusu, C., Teuțan, E., Lungu, I., "Development of Robotic Systems for Upper and Lower Limbs Kinetotherapy", Acta Electrotehnica, vol. 48, nr. 4, pp. 13-18, 2007.

[6] Khanicheh, A., Muto, A., Triantafyllou, C., Weinberg, B., Astrakas, L., Tzika, A. and Mavroidis, C., "MR Compatible ERF Driven Hand Rehabilitation Device", *Proceedings of the 2005 IEEE 9th International Conference on Rehabilitation, USA*, pp. 8-12, 2005.

[7] Unlurhisarcikli, Ozer et al., "A Robotic Hand Rehabilitation System with Interactive Gaming Using Novel Electro-Rheological Fluid Based Actuators", *IEEE Int Conf on Robotics and Automation, Anchorage*, pp. 1846-1851, 2010.

[8] Khanicheh, A., Mintzopoulos, D., Weinberg, B., Tzika, A. and Mavroidis, C., "MR_CHIROD v.2: Magnetic Resonance Compatible Smart Hand Rehabilitation Device for Brain Imaging", *IEEE Transactions On Neural Systems And Rehabilitation Engineering*, Vol. 16, Nr. 1,pp. 91- 98, 2008.

[9] Weinberg, B., Nikitczuk, J., Patel, S., Patritti, B., Mavroidis, C., Bonato, P., Canavan, P., "Design, Control and Human Testing of an Active Knee Rehabilitation Orthotic Device", *IEEE International Conference on Robotics and Automation*, pp. 4126-4133, 2007.

[10] Vishal. J., "Design and control of active knee rehabilitation orthotic device (AKROD)", Mechanical Engineering Master's Theses, Department of Mechanical and Industrial Engineering, Northeastern University, 2009.

[11] Mavrodis, C., Nikitczuk, J., Weinberg, B., Danaher, G., Jensen, K., "Smart portable rehabilitation devices", *Journal of NeuroEngineering and Rehabilitation*, DOI:10.1186/ 1743- 0003-2-18, 2005.

[12] Kikuchi, T., Jin, Y., Fukushima, K., Akai, H., Furusho, J., "Study on Development of Active-Passive Rehabilitation System for Upper Limbs: Hybrid-PLEMO", 11th Conference on Electrorheological Fluids and Magnetorheological Suspensions, Journal of Physics: Conference Series 149, IOP Publishing, DOI: 10.1088/1742-6596/149/1/012016, 2009.

[13] Chetran, B**,** Szelitzky, E., Aluţei, A. M., Mândru, D., "Movement control of active/passive exercisers", *Journal of Vibroengineering*, vol. 14, ediția 1, pp. 7-15, Kaunas, Lituania, ISSN 1392-8716, 2012.

[14] Chetran, B., Szelitzky, E, Aluţei, A. M., Mândru, D., "High Voltage Systems For Driving Electrorheological Fluids In Rehabilitation Systems", The 3rd International Conference on Recent Achievements in Mechatronics, Automation, Computer Sciences and Robotics (MACRo2011), Automation, Computer Science and Robotics, Tîrgu Mureş, Editura Poublishing House, ISBN: 978-973-1970-54-7, 2011.

[15] Hauke, B., "Basic Calculation of a Boost Converter's Power Stage", Texas Instruments Application Report: SLVA372B–November 2009–Revised July 2010, online at: http://www.ti.com/lit/an/slva372b/slva372b.pdf.

[16] Chetran, B., "Experimental stand for determining the flow of electrorheological fluids between two parallel disks", Conference for Students and Young Researchers "Mechatronics for Hi-Tech Devices", Kaunas, Lithuania, 2011.

Acta Universitatis Sapientiae
Electrical and Mechanical Engineering, 4 (2012) 96-102

Epicycloidal Gear Shaping Machine

Mihai ZAH, Daniel LATES, Sorin BESOIU, Vencel CSIBI

Department of Mechatronics and Machine Dynamics,
Technical University of Cluj-Napoca,
e-mail: zahmihai58@yahoo.com, daniellates@yahoo.fr
e-mail: sorinbesoiu@yahoo.com, csibiven@yahoo.com

Abstract: In order to manufacture epicycloidal gears used in cycloidal drives, a machine was designed to generate the epicycloidal and equidistant profiles of the shortened epicycloid. The designed machine mainly consists of two interchangeable gears, whose division diameters are equal to the diameters of the epicycloid generators. The shortened epicycloid generator point is materialized by the shaft of the shaft mill, while the circle whose center is the generating point and materializes the equidistant to the shortened epicycloid is represented by either the shaft mill or the mill. The piece execution required movements are the cutting motion (shaft mill spin), non-slip rolling motion, and circular feed motion. These motions are accomplished through a kinematic chain composed from a feeder box, a gearbox, and an eccentricity adjustment mechanism.. The adjustment of the feed gain, of the generating gear radius ratios, and of the eccentricity of the generator point are accomplished manually with the aid of sliding sled devices equipped with graded drums. The feeder box and the gearbox are driven by two DC motors, their required power alongside the cutting parameters being determined according to the included formulae.

Keywords: epicycloidal gear, equidistant profile, design, manufacture machine, materialization

1. General information

The current solution of epicycloidal gear design represents the materialization of the theoretical definition of the epicycloid.

The epicycloid is a planar curve [1, 2, 4, 5] generated in the plane of a base circle C_b by a point G attached to the generating circle C_g which is rotating without slipping on the exterior circumference of the fixed base circle C_b (*Fig. 1*).

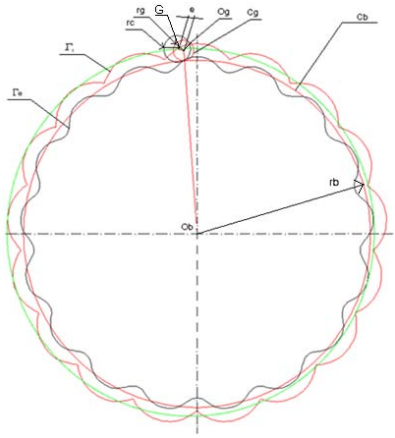

Figure 1: Generating the shortened epicycloid and the equidistant profiles

Gears with an epicycloidal profile are employed in bolt cycloidal speed reducers [3, 4, 5] (also called cycloidal drives) in which the satellite gear with a number of z teeth with an epicycloidal profile engages with $z+1$ bolts. This way, the generator point G that is attached to the generating circle C_g, situated inside it at a distance of e from its center O_g will produce z branches of the shortened epicycloid Γ_t. If in point G we fasten a bolt of radius r_c, this will envelop an equidistant to the shortened epicycloid Γ_e, which, if materialized (*Fig.2*), represents the satellite gear of the speed reducer.

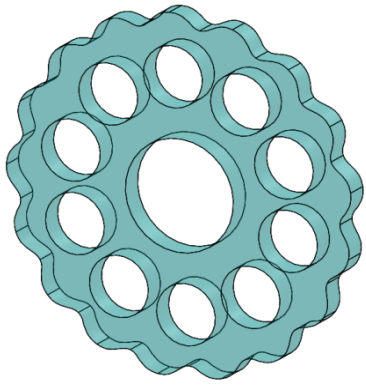

Figure 2: Epicycloid gear (isometric view)

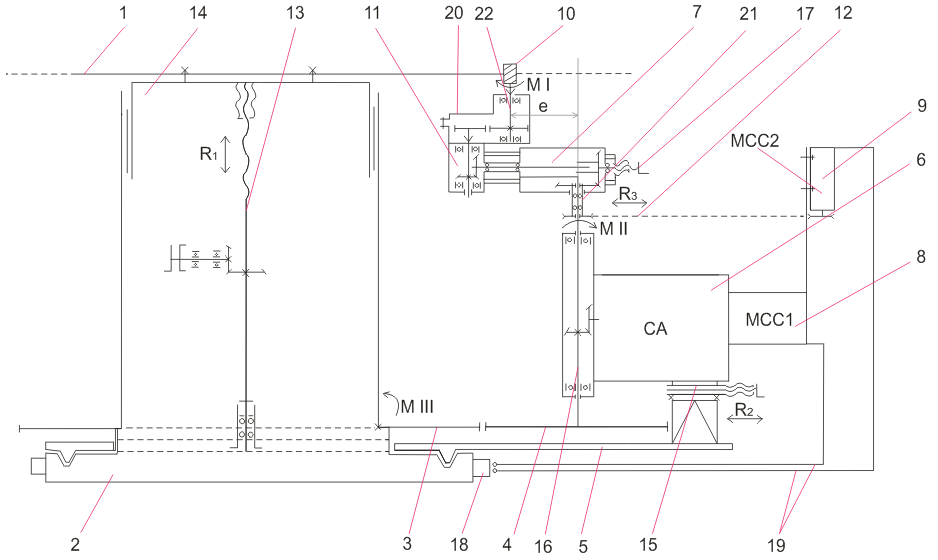

Figure 3: Machine that performs the toothed planetary gear

The machine that can manufacture the epicycloidal gear is described below (*Fig.3*) and has the following components:

1 - Workpiece blank;
2 - Circular guide frame;
3 - Fixed gear (rack), materializing circle $C_{b;}$
4 - Rolling gear, materializing circle C_g;
5 – Sledge with Circular guide;
6 - Cutting box advance (milling or grinding);
7 - Cutting box gearbox;
8 - DC motor for advance (MCC1);
9 - DC motor for cutting (MCC2);
10 - Grinding bit or abrasive disc;
11 - Shaft mill spindle;
12 -Transmission belt;
13 - Workpiece raising-lowering mechanism (R_1);
14 - Plate;
15 - Slide adjustment mechanism (R_2);
16 - Vertical spindle for rolling movement (MII);
17 - Slide adjustment mechanism for eccentricity **e (**R_3);
18 - Ring rail for DC power supply;

19 - Power cable with collector brushes;
20 - Shaft mill spindle adapter for small eccentricities;
21 - Belt wheel bloc – conical gear;
22 - Shaft mill spindle for small dimensions.

Certain elements of this machine are able to perform the technological motions as follows:

- M_I - shaft mill rotation (cutting);
- M_{II} - no-slip rotation;
- M_{III} - circular feed;
- R_1 - manual adjustment for penetration feed;
- R_2 - manual adjustment of radius of generating circles radius ratio;
- R_3 - manual adjustment of eccentricity **e.**

Frame 2 supports all the other mechanisms which compose the gear-making machine, has around it a V-shaped guide and a central round guide in which plate 14 slides, on which the workpiece blank is fastened.

Gear 4 is the one doing the rolling motion (MII) and drives sled 5 through its circular advance motion (MIII), which supports other mechanisms.

The motion of the rolling gear 4 is provided by the MCC1 DC motor through the feed box 6, a conical gear with output on shaft 16, held by two radial thrust bearings. The exchangeable rolling gear 4 is fastened at the extremity of this spindle. The other extremity contains a flange that supports gearbox 7, spindle 16, gear 4, feedbox 6 and the DC motors 8 and 9.

The sliding of the plate is performed with mechanism 13, composed of a nut fastened to the plate, a trapezoidal thread screw supported by a spherical thrust bearing, with radial and axial ball bearings. The rotation of the screw is accomplished by an assembly of bevel gears driven from outside the bearing pedestal through a crank wheel with a graded drum to measure the penetration feed.

On the outside of the frame is fastened gear 3. It materializes through its nominal diameter the base circle C_b given by the epicycloid definition. Control sled 15 is guided by the circular guide 5.

Gearbox 7 receives motion from DC motor 9 through the bloc 21 consisting of transmission belt 12 and a conical gear. This bloc 21 is attached to shaft 16 via two radial thrust bearings but rotates independently from it. The conical pinion gear from bloc 21 engages with the conical gear in gearbox 7 fitted with a grooved sleeve through which a grooved shaft slides (when adjusting R_3), transmitting motion to the conical gear on the shaft of shaft mill 11.

The adjustment control R_3 ensures the realization of dimension ***e***. In order to allow small values, we can mount of the shaft of shaft mill 11 a housing, 20, which supports a spur gear drive of the same diameter, the shaft of shaft mill 10 becoming in this case spindle 22. In such a way we can manufacture epicycloids

with a generating circle C_g of radius r_g < 15mm. The shaft mill's center represents the generator point G from the epicycloid definition, whereas dimension ***e*** represents the eccentricity of the generating point G, and the exterior diameter of the shaft mill is equal to the diameter of the circle that generates the equidistant to the shortened epicycloid.

Adjustment of the eccentricity e of the generating point G is accomplished through the sled mechanism 17 fastened to the side of gearbox 7, which engages only shaft 11, respectively housing 20 in its manual adjustment of R_3.

In order to manufacture different epicycloid profile gears, gears 3 and 4 will be exchanged with others of different dimensions, materializing the generating circles C_b and C_g of the proposed epicycloid.

Power supply of the DC motors 8 and 9 is realized using the ring rail 18 through the collector brushes and cable 19.

The adjustment of the cutting parameters (cutting speed and feed) is achieved by modifying the speed of the DC motors, parameters which will be selected after the optimal cutting regime is computed. For the same purpose we also draw the plot of the speed for the gearbox.

2. Theoretical setting technological parameters milling machine with toothed planetary gears

The M_I motion is the shaft mill rotation which executes a slot in the workpiece which is identical to the profile of the shortened epicycloid's equidistant.

The M_{II} movement is the feed.

Cutting speed v is calculated by equation (1)

$$v = \frac{c_v d_f^q}{T^m t_l^x s_d^y t^n z^p} k_v \quad \text{[m/min], where} \tag{1}$$

- c_v – a constant characterizing the milling conditions;
- T – economic sustainability of the shaft mill bit [min];
- t_l – contact length [mm];
- t – cutting depth [mm];
- k_v – speed correction coefficient;
- d_f – shaft mill diameter [mm];
- s_d – feed per tooth [mm];
- q, m, x, y, n, p – exponents.

The feed per minute s_m is determined by equation (2)

$$s_m = s_d \, z \, n \quad \text{[mm/min], where} \tag{2}$$

- s_d – advance per tooth [mm];
- z – number of teeth on the shaft mill;
- n – shaft mill's rotation speed determined by relation (3) based on cutting speed v and the shaft mill diameter d_f.

$$n = \frac{1000\,v}{\pi\, d_f} \quad \text{[rot/min]} . \tag{3}$$

Substituting equation (3) into equation (2) we get:

$$s_m = \frac{1000\,v\,s_d\,z}{\pi\, d_f} \quad \text{[mm/min]} . \tag{4}$$

Calculating transmission ratio of the feedbox i_{CA}:

$$i_{CA} = \frac{n_1}{n_{Cg}} \text{, where} \tag{5}$$

- n_1 – average speed of DC motor M_{CC1};
- n_{Cg} – speed of the generating gear C_g calculated with formula (6).

$$n_{Cg} = \frac{s_m}{2\pi\, r_g} \quad \text{[rot/min]} . \tag{6}$$

Calculation of the transmission ratio i from the engine MMC to milling:

$$i = \frac{n_2}{n} = i_{CV}\, i_c \text{, where} \tag{7}$$

- n_2 – average speed of DC motor M_{CC2} [rot/min];
- n – shaft mill speed [rot/min];
- i_{CV} – transmission ratio CV;
- i_c – belt transmission ratio.

The required power P_e [kW] must be at least:

$$P_e \geq P_n\, \eta \text{, where} \tag{8}$$

P_n- nominal power [kW], η - device efficiency coefficient.
Depending on the cuting parameters the expression of the cutting power is [6]

$$P_e = k\, d_f^{\,x}\, t_l^{\,n}\, s_m\, s_d^{\,y}\, t^{w} \quad \text{[kW], where} \tag{9}$$

- d_f – shaft mill diameter [mm],
- t_1 – contact length [mm],
- s_m – advances per minute [mm/min],
- t – cutting depth [mm],
- s_d – advance per tooth [mm],
- x, n, y, w – exponents.

3. Conclusions

Gears with epicycloidal tooth profiles are components of bolt cycloidal speed reducers.

Their implementation can be accomplished through shaping with an adequate cutting blade, milling with a worm hob of appropriate profile, or milling on a CNC machine.

Using the presented gear shaping machine, we can create epicycloidal tooth profile gears according to the generating scheme of the equidistant to the shortened epicycloid in a wide range of products. This is ensured by the possibility of modifying the generating gears, the equidistant e, and the shaft mill's diameter.

References

[1] Csibi, V. I., "Angrenaje elicoidale cu profiluri special", Editura Gloria Cluj-Napoca, 1999.
[2] Csibi, V. I., Popa, M., Mătieş, V., "Maşini şi Instalaţii de Prelucrat în Mecanica Fină", Editura Gloria, Cluj-Napoca, 1999.
[3] Csibi, V. I., Teutan, E., Barbu, D., Botiz, E., "Angrenaj cicloidal cu bolţuri cu joc radial reglabil" , PRASIC'02, Braşov, 2002.
[4] Filipoiu, I. D., Tudor, A., "Proiectarea transmisiilor mecanice", Ed. BREN, Bucureşti, 2006.
[5] Petrescu, F. N., "Contribuţii la Studiul Frecării şi Uzării la Angrenajele Reductoarelor Speciale Folosite la Mecanismsle Maşinilor de Construcţii" , Teza de Doctorat, Institutul de Construcţii Bucureşti, Bucureşti 1987.
[6] Picos, C., "Calculul adaosului de prelucrare şi a regimurilor de aşchiere", Ed. Tehnică, Bucureşti, 1974.
[7] Szekely, I., Dali, A., "Mecanisme" , Litografia UTCN, Cluj-Napoca 1992.
[8] Ta-Shi Lai, "Desing and machining of the epicycloids planet gear of cycloid drives", Springer-Verlag London Limited, 2005.

Acta Universitatis Sapientiae
Electrical and Mechanical Engineering, 4 (2012) 103-110

Thermal Calculation for Planetary Cycloidal Gears with Bolts

Mihai ZAH, Daniel LATES, Vencel CSIBI

Technical University of Cluj-Napoca,
Department of Mechatronics and Machine Dynamics
e-mail: zahmihai58@yahoo.com
e-mail: daniellates@yahoo.fr
e-mail: csibiven@yahoo.com

Manuscript received March 15, 2013; revised July 15, 2013

Abstract: Cycloidal speed reducers are special high ratio transmissions developed to reduce speed. They are able to transmit and high power also. The applicability is in almost all operations of machinery, particularly where positioning accuracy is required (medical equipment, instrumentation and control, robotics, etc.). During function power loss occurs due to the friction between the contacting elements of this gear (elements of gearing, bearings, bearing on eccentric rollers on the pins) The power lost due to friction in kinematic couplings turns into heat, phenomenon that heats the reduction gears. A quantity of the heat is released into the atmosphere through the housing while another part is taken by the lubricating oil. The amount of heat produced in reducer during operation is determined considering its overall performance, respectively computing power losses of kinematic couplings. From the condition of thermal equilibrium (quantity of heat equal to the amount of heat released) the operating temperature is computed. If temperature exceeds the admitted maximum value it must be decreased by increasing the reduction gear housing's surface and the oil amount.

Keywords: cycloidal speed reducer, friction, power, heat

1. Description of cycloidal speed reducers with bolts

Cycloidal speed reducers with bolts are special gears obtained as a particular case of cycloidal planetary gears, for which the engaging line is represented by a circle arc, and the angle of pressure is variable [1,5]. The cycloidal speed reducer with bolts is composed of two main functional parts: the actual cycloidal gear with bolts and the transversal homokinetic bolted joint.

The central element of the cycloidal planetary gears with bolts [1], (*Fig. 1*) is the input shaft 1. It holds the eccentric plate 3. On this are mounted – through cylindrical roller bearings 10 – are one, two or more satellite wheels endowed with exterior cycloidal profiled teeth. Through the motion the eccentric plate, due to its eccentricity engages the teeth of the satellites with the central wheel 4 whose inner teeth consist of five circular disposed equidistant embedded bolts.

The transversal homokinetic joint consists of the output shaft 7 (coaxial with the input shaft 1) ending in a flange. The flange sustains the circularly disposed bolts 8 which will take over the motion and the torque from the satellite gears. It interacts through a number of dents equal to the number of pins 8, inscribed in a circle, to the satellites 2 and 2'.

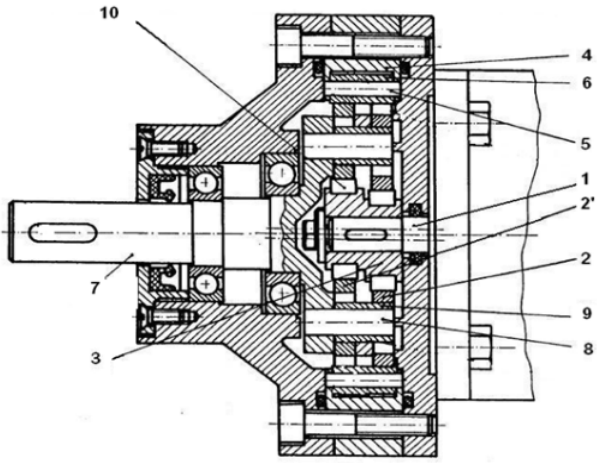

Figure 1: Cycloidal speed reducer with bolts [1]

In order to reduce friction between the satellite wheels 2 and 2' and bolts 5 of the central wheel 4, also between the satellite wheels 2 and 2' and bolts 8 of the homokinetic joint, the bolts are fitted with rollers 6 and 9, which rotate freely about its the bolt's axis.

2. The operational mode of cycloidal gear with bolts

The M_m torque is transmitted from the input shaft 1 to the eccentric 3 and the roller wheels 10 which interact with satellite gears 2 and 2', causing their nearing or distancing from the bolts 5 of the fixed crown 4. Reaction forces created in the rotation couplings formed between the bearings and the satellites tend to rotate the satellites in the direction of rotation of the input shaft 1. The nearing of satellites towards the central wheel causes their interacting with bolts 5 of the fixed wheel 4.

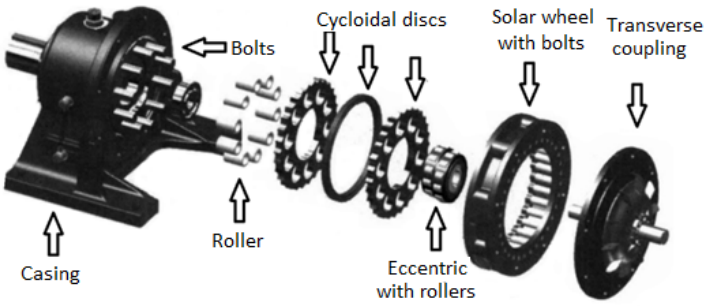

Figure 2: Cycloidal gear with bolts - assembly parts [5]

In the superior coupling, reactions R52 and R52' are created at the application point, tangent to the bolts (bushings 6) with the cycloidal profile of the satellite wheels. They are oriented alongside the common normal of the two tangent profiles in their contact point. Those reactions cause the satellites to rotate in reverse sense compared to the rotation of the input shaft with speed $n = n_m/z_4$, where n_m is the input shaft speed, and z_4 is the number of bolts 5 of fixed wheel 4.

Collection of the motion and torque from the satellite wheels is achieved with the help of the homokinetic joint, and transmitted to output shaft 7.

3. Thermal calculations

In the upper couplings with linear contact (formed by the interaction of bolts 5 with rollers 6, by rollers 6 with the cycloidal profile of satellite gears 2 and 2', by bolts 8 of the homokinetic joint with rollers 9 and of those with the circular profile of pits on satellites 2 and 2'), also through the interaction between the rollers of bearing 10 of the eccentric 3 with satellite gears 2 and 2', friction appear. As a result power losses and the transmission's efficiency decreases. The amount of heat Q released during operation is calculated using the formula (1)

$$Q = 260(1-\eta)N \text{ [kcal/h] where} \tag{1}$$

- N – the driving shaft power in [kW];
- η – the global efficiency of reducer.

The amount of heat released is influenced by the efficiency of the gearbox, whose value is calculated with the equation (2):

$$\eta = \eta_t \eta_u \eta_l \text{ where} \tag{2}$$

- η_t – the efficiency of the gearing;
- η_u – efficiency of the oil, taking into account its bubbling losses;
- η_l – efficiency of bearings.

The oil efficiency η_u is calculated by the relation (3)

$$\eta_u = \frac{1{,}36N - 0{,}082V\,B\sqrt{V\nu\dfrac{200}{z_2 + z_4}}}{1{,}36\,N} \text{ where} \tag{3}$$

- N – the transmitted power [kW];
- B – the total width of the satellites [m];
- V – the peripheral speed of satellites [m/s];
- ν – the viscosity of the oil [cst];
- z_2, z_4 – number of teeth of satellite gears, and the number of bolts.

The transmission efficiency η_t can be calculated according to the specific loss coefficient ψ representing power loss if the gearing is considered an ordinary gear. The relation to calculate the efficiency in this case is [2]:

$$\eta_t = \frac{1-\psi}{1+z_2\psi}. \tag{4}$$

The loss coefficient ψ has three components according to relation (5):

$$\psi = \psi_{26} + \psi_{29} + \psi_{32} \text{ where} \tag{5}$$

- ψ_{26} – the specific loss of engagement of fixed crown gear bolts with the satellite gear;
- ψ_{29} – the specific loss of the coupling of the homokinetic joint;
- ψ_{32} – the specific loss of the coupling between the eccentric and the satellite.

To determine the loss coefficient ψ, three coefficients will be calculated as follows:

a) Specific loss coefficient of cycloidal gearing with bolts:

$$\psi_{26} = K_a\,\mu_a / z_4 \text{ where} \tag{6}$$

- K_a – a coefficient that is chosen in dependence with the correction coefficient ξ according to (*Fig. 3*);
- μ_a – the gearing friction coefficient.

In [2] we recommend for μ_a the highest value of either the coefficient of friction between bolts 5 and rollers 6, μ_{56} , or μ_{26} the friction coefficient between the teeth and roller 6 (*Fig. 4*) [3]. Experimentally it was found that power losses

are to a greater extent influenced by friction between the bolts and rollers (due to different conditions of lubrication) than friction between rollers and the cycloidal profile. The friction coefficient μ_{26} depends on the rolling speed, and is determined according to figure 5.

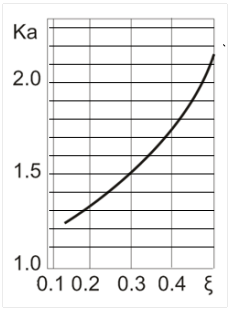

Figure 3: Value of the coefficient K_a, depending of ξ

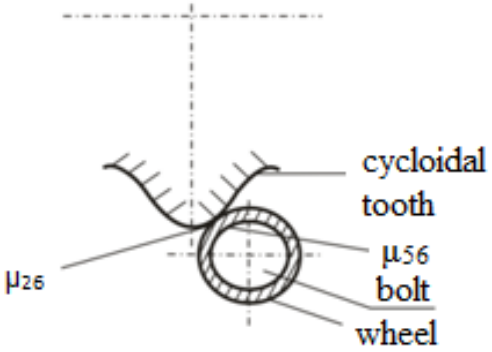

Figure 4: The interaction cycloidal-wheel of profile, wheel-bolt

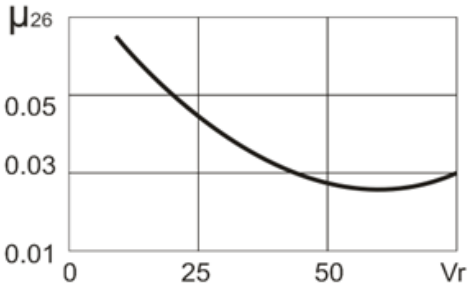

Figure 5: Value of the coefficient μ_{26}, depending of v_r

b) Specific loss coefficient in the transverse coupling with bolts shall be determined by the relation (7)

$$\psi_{29} = \frac{4e\,\mu_v}{\pi\,R_v} \text{ where} \tag{7}$$

- e – the eccentricity of the gear;
- μ_v – the equivalent friction coefficient,
- R_v – the radius of placement of bolts on the transverse coupling.

Identical with those considered under point a), friction occurs between the profile pits of radius r_{ro} on satellite gears 2 and 2' and rollers 9 of radius r_{ro}, and between rollers 9 and bolts 8 (*Fig. 6*). According to [2] the coefficient of friction μ_v is chosen according to (*Fig. 6*) in dependence with the speed of rolling v_r, which is calculated with the equation (8):

$$V_r = (r_v + r_{r0})(\omega_2 + \omega_3)\,[\text{m/s}], \text{ where} \tag{8}$$

- ω_2 – the angular velocity of the satellite wheel [m/s];
- ω_3 – the angular velocity of the eccentric [m/s]
- r_v, r_{r0} – the radius of the pit, respectively the roller 9 [m].

c) Specific loss coefficient in the bearing of the eccentric: according to [2] it is given by:

$$\psi_{32} = 1{,}63\left(1+\frac{D_3}{d_r}\right)\frac{f_r}{r_a}\sqrt{1+\left(\frac{4}{\pi}\frac{r_a}{R_v}-K_y\right)^2}\text{ , where} \tag{9}$$

- D_3 – the diameter of eccentric 3;
- d_r – the diameter of rollers in bearing 7;
- f_r – coefficient of rolling friction;
- r_a – radius of the base cycle used in the satellite profile generation;
- R_v – radius of placement of bolts on the homokinetic joint;
- K_y – coefficient of the correction applied to the gearing (*Fig. 7*).

Considering the three components of the loss coefficient, formula (5) becomes:

$$\psi = \frac{K_a\mu_a}{z_4} + \frac{4e\mu_v}{\pi R_v} + 1{,}63\left(1+\frac{D_3}{d_r}\right)\frac{f_r}{r_a}\sqrt{1+\left(\frac{4}{\pi}\frac{r_a}{R_v}-K_y\right)^2} \tag{10}$$

Using formula (10) formula (4) can be used to determine the global efficiency of the transmission. The efficiency η_l of bearing elements depends on the type of bearing and the peculiarities of the construction of the gearbox.

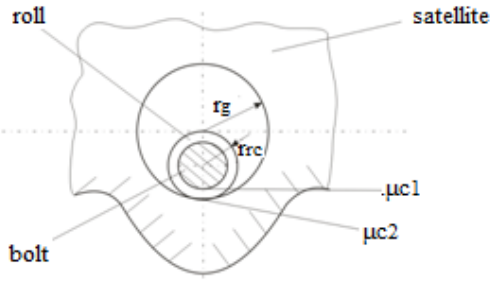

Figure 6: Interaction between coupling and satellite [3]

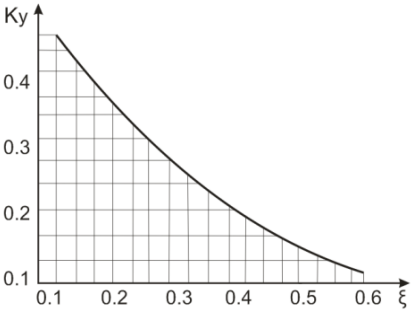

Figure 7: Value of the coefficient K_y, depending on ξ [6]

By example the analyzed type of gearbox uses two types of bearings. Considering that a bearing of high performance ($\eta_{per} = 0{,}99$), [4] is used it results $\eta_l = 0{,}98$. Computing η_u using equation (3), η_t from equations (4) and (10) and considering the previous determined lubrication efficiency coefficient the global efficiency of the transmission becomes possible to be calculated by equation (2). After this, the quantity of heat Q caused by power losses in the speed reducer will be computed using relation (1).

The quantity of heat that can be released in the environment Q_1 by the speed reducer casing is given by [8]:

$$Q_1 = \alpha S\left(t - t_0\right) \text{ [kcal/h], where} \tag{11}$$

- α – the coefficient of heat transmission through the surface S, α =10…18 [kcal/m^2 °C];
- S – the surface of the housing [m^2];
- t – the limit temperature of the transmission [°C];
- t_0 – the ambient temperature [°C] ,(t_0 = 20 °C).

The operating temperature of the speed reducer is determined from the condition of thermal equilibrium, i.e. heat Q produced during the operation of the reducer is equal to the amount of heat exhausted to the environment Q_1:

$$Q = Q_1 . \tag{12}$$

In the case of natural cooling and a long-term operation, operating temperature limit is given by the formula:

$$t = t_0 + \frac{860(1-\eta)}{\alpha S} . \tag{13}$$

For a good operation of the reducer we impose that the normal operating temperature should not exceed the admissible value $t_a = 70 \ldots 85\,°C$ [4]. Increasing the operating temperature above the permissible value causes a large decrease in viscosity of the oil which leads to improper lubrication and therefore the premature destruction of the reducer components [7].

If operating temperatures calculated according to the equation (13) result greater that the admissible limit value, then a fan can be mounted on the input shaft to help cool off portions of some of the reducer housing.

Another solution is to increase the surface S by manufacturing a ribbed outer enclosure.

3. Conclusion

When designing bolted cycloidal speed reducers the condition of thermal equilibrium must be taken into consideration.

If the calculated operating temperature results higher than the permissible temperature, when designing the speed reducer housing, a ribbed model can be selected in order to increase its outer surface, acting as a heat sink.

References

[1] Csibi, V., Teuțean, E., Barbu, D., Bodizs, E, "Angrenaj cicloidal cu bolțuri cu joc radial reglabil", Ed. Universitatea Tehnică, Cluj – Napoca, 2000.
[2] Kudreavțev, V. N., "Plnetarnîe peredaci", Moscova-Leningrad, Maşghiz, 1966.
[3] Petrescu, F. N. "Contribuții la studiul frecării şi uzării la angrenajele special folosite la mecanismele maşinilor de construcții", Teză de doctorat, I. C. Bucureşti, 1987.
[4] Tudor, A., Filipoiu, D. "Proiectarea transmisiilor mecanice", Ed. Bren, Bucureşti, 2006.
[5] Burns, S., "ProQuest Central Cicloidal Sense", Dec.2007, Don Mills, Canada.
[6] Maros, D. "Calcule numerice la mecanismele plane", Ed. Dacia, Cluj-Napoca, 1987.
[7] Pavelescu, D., "Tribologie", Ed. Didactică şi Pedagogică, Bucureşti, 1977.
[8] Pavelescu, D., "Tribotehnică", Ed. Tehnică, Bucureşti, 1983.

Acta Universitatis Sapientiae
Electrical and Mechanical Engineering, 4 (2012) 111-118

Rotational Pneumatic Drive with Radial Jet Action

Ovidiu ŞERDEAN, Vencel CSIBI

Technical University of Cluj-Napoca,
Department of Mechatronics and Machine Dynamics
e-mail: onyx_cj@yahoo.com, csibiven@yahoo.com

Manuscript received March 15, 2013; revised September 15, 2013

Abstract: In this paper authors present a study on a rotational pneumatic drive with radial jet action. Rotational pneumatic drive with radial jet action is a special drive using power of compressed air to produce rotational motion. The rotating motion is generated by jets, generating tangential oriented forces which act on the rotor. This study presents some of the theoretical and experimental results referring the operating parameters of a jet rotation drive.

Keywords: rotation pneumatic drive, jet, radial action, jet action, rotational motion

1. Description of pneumatic drive with radial jet action

Pneumatic drive with radial jet action consists of the following parts that can be found in Fig. 1.

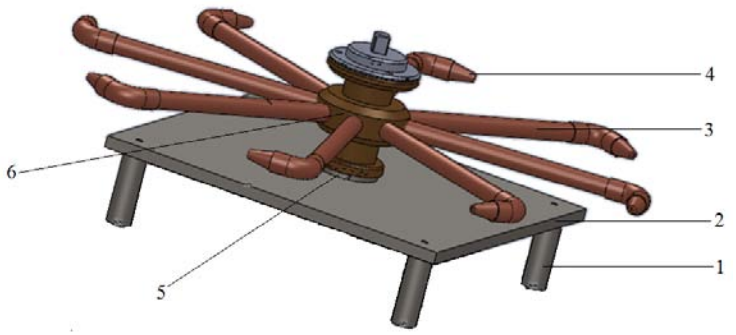

Figure 1: Pneumatic drive with radial jet action.

The feet 1 sustain the plate 2, designed to support the entire engine. In the center of the plate a large diameter threaded hole connects the compressed air network. Body supply 5 is fixed on plate 2 through screws disposed concentrically with the previous hole.

The supply body 5 is made of OL 50construction steel. Geometrically it consists of a tube ended in a shoulder where the main body 6 is fixed. At the top of the supply body another shoulder mounted by thread of the top of supply body serves to fix the top of the main body. On the cylindrical surface of the supply body are channels linking the outside and the inside of it.

The cylindrical shaped main body 6 is mounted on the supply body. It is made of bronze. On the outside of the main body are mounted the tubes 3 of the pneumatic drive that communicate with the inside of the main body through holes.

Pneumatic drive duct 3 were made of copper have a tubular shape, which are glued to the main body at one end and the other end attached to an elbow at 90°. With the elbow positioned nozzle and adjust the angle of 90° jet nozzle produced a pneumatic motor motion having a tangential direction.

The tubular nozzles 4 present variable inner diameters, where the input is greater than the output. More exactly, the inner diameter decreases parabolically. The nozzle's geometry influences mainly the characteristics of the jet propulsion.

2. The operational mode of pneumatic drive with radial jet action

On the lower support plate is mounted a device that connects the pneumatic drive to the compressed air network.

The compressed air enters the device mounted on the lower support plate in the inside of the supply body. The communication channels connect the inner and outer passages of the compressed air. Thus the compressed air passes from supply body in the main body. Due to the specific geometry of the nozzles, the outcoming compressed air is accelerated. At the leave of the nozzle results the jet propulsion force that depends mainly on the flow and density of operating air.

3. Analytical calculation of parameters pneumatic drive

The functional parameters were calculated considering the following values of the operating parameters:

- internal pressure: 5 bar;
- external pressure: 1 bar;
- temperature: 300 K;
- specific mass of O_2: 32kg/kmol;

- k = 1,4– the correction coefficient while the compressed fluid is oxygen;
- air outlet section $A = 7{,}065 \cdot 10^{-6}\ \mathrm{m}^2$.

The value of the critical pressure is given by the following formula [3, 4]:

$$p^* = p_1 \left(\frac{2}{k+1} \right)^{\frac{k}{k-1}} = 5 \cdot \left(\frac{2}{2{,}4} \right)^{3{,}5} = 2{,}64\,\mathrm{bar}. \tag{1}$$

The temperature in the output section will reach the value [2,4]:

$$T_2 = T_1 \left(\frac{p_2}{p_1} \right)^{\frac{k-1}{k}} \cdot \left(\frac{1}{5} \right)^{0.2857} = 189\,\mathrm{K}. \tag{2}$$

The density of the working fluid in the output section is computed by:

$$\rho = \frac{p_2}{RT_2} = 2{,}036\ \frac{\mathrm{kg}}{\mathrm{m}^3}. \tag{3}$$

The outcoming velocity of the fluid in the output section is

$$w_2 = \sqrt{\frac{2k}{k-1} RT_1 \left[1 - \left(\frac{p_2}{p_1} \right)^{\frac{k-1}{k}} \right]} = 448\ \frac{\mathrm{m}}{\mathrm{s}}. \tag{4}$$

Using (4) the volumic flow for a nozzle will be:

$$m = w_2 A = 7{,}065 \cdot 10^{-6} \cdot 448 = 3{,}165 \cdot 10^{-3}\ \frac{\mathrm{m}^3}{\mathrm{s}}. \tag{5}$$

Finally, the total volumic flow for all nozzles becomes:

$$m = 8 A w_2 = 25{,}32 \cdot 10^{-2}\ \frac{\mathrm{m}^3}{\mathrm{s}}. \tag{6}$$

Using results obtained from the equations (1) to (6), the global force produced by all fluid jets can be computed with the formula below:

$$F = m \rho w_2 = 448 \cdot 2{,}036 \cdot 25{,}32 \cdot 10^{-2} = 23{,}095\ \mathrm{N}. \tag{7}$$

4. Experimental determination of parameters of the pneumatic drive

In the proposed experimental determinations, the following equipment components will be used in order to find the values of the functional parameters for pneumatic drive with radial jets (force jets, rotation and drive operating pressure):

- force sensor type 1242 Vichay Tedea-Huntleigh;
- pressure sensor type HBM P3MB of 10 bar pressure;
- data acquisition system type HBM Spider 8;
- pressure source;
- PC unit;
- tachometer type DT 1236L Lutron Electronic;
- pneumatic drive with radial jet.

The configuration of the experimental set-up is presented in *Figure 2*.

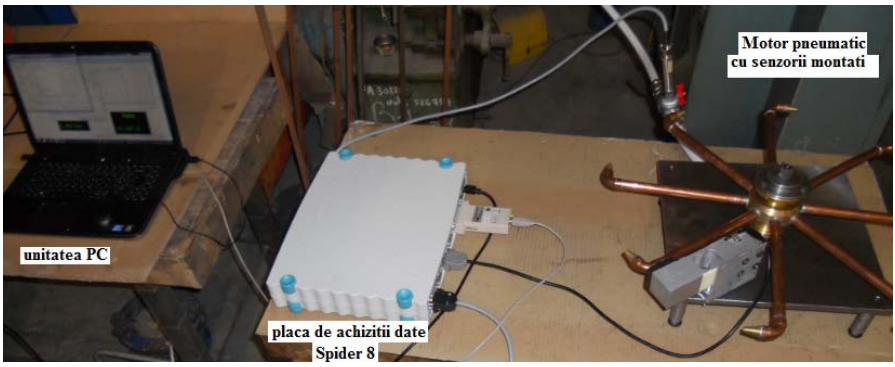

Figure 2: Configuration of experimental set-up

The experimental value of the pressure inside of the pneumatic drive is output on a screen (Fig.3).It can be observed that a pressure of is 3.941 bar is able to produce a the jet force of 24.45 N. It can be concluded that the experimental values are close to the computed values.

Figure 4 shows the measured value for rotation of pneumatic drive with radial jets.

Here it must be noticed that the pneumatic drive is equipped with 8 pipelines, and as a consequence the tachometer records eight values for one complete rotation. Knowing this the computation of the real rotation value will be done using the correction below:

$$n = \frac{n_{registered}}{N_{pipelines}} = \frac{42834}{8} = 5354 \text{ rpm} . \quad (8)$$

Figure 3: Pressure from inside of pneumatic drive and the jets force

Figure 4: Value for maximum rotation

5. The functional diagrams of radial jet engine

The dependence of the force with the rotation is shown in *Figure 5*.

It can be concluded that the variation of the force with the rotation is approximately linear.

The volumic flow variation with the force is shown in Figure 6 which lets us conclude that there is a parabolic dependence.

As shown in (Figure 8), the variation of flow with rotation is also parabolic.

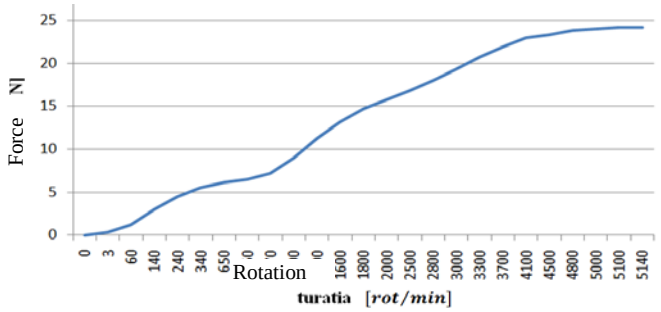

Figure 5: Variation of force with rotation

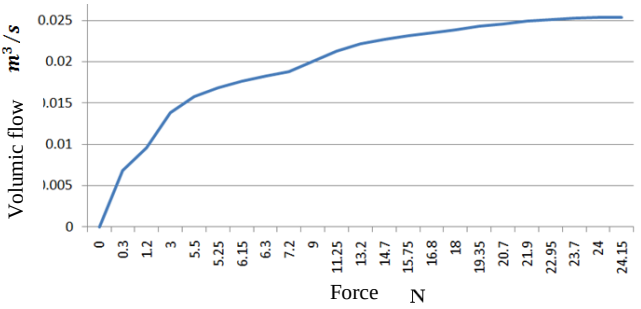

Figure 6: Variation of flow with force

The variation of the force with the pressure is also linear (*Figure 7*):

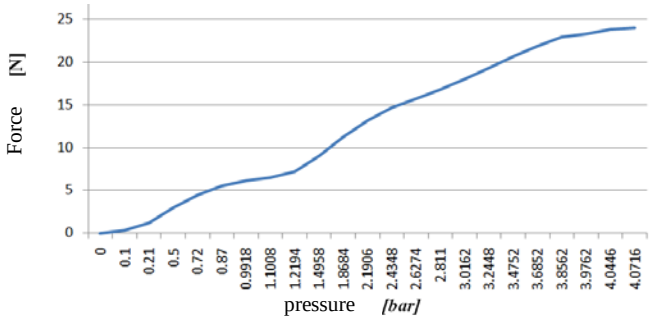

Figure 7: Variation of force with pressure

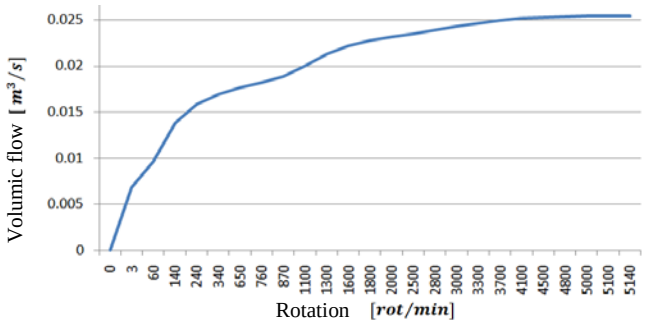

Figure 8: Variation of flow with rotation

6. The estimation of the error given by the formula of the force created by the fluid jet

Comparing the final result of force value given by the formulas (1 to (7) with the measured value, the occurred error percentage is:

$$\varepsilon[\%] = \frac{F_{measured} - F_{computed}}{F_{computed}} \cdot 100 = \frac{24{,}45 - 23{,}095}{24{,}45} \cdot 100 = 5{,}54\ \%\ . \qquad (9)$$

Result (9) allows to conclude that the theoretical model is appropriate.

7. Conclusion

A new type of fluid jet driven pneumatic rotary motor was conceived and realized. The technical peculiarities of this can be summarized as follows:

- Drive power is directly proportional to the length and diameter of the motor arm and motor rotation value;
- The variation of force with rotation is linear;
- The variation of flow with force is parabolic;
- The variation of force with pressure is linear;
- The variation of flow with rotation is parabolic.

References

[1] Călăraşu, D., “Acţionări pneumatice”, Editura POLITEHNIUM, 2010.
[2] Coşoroabă, V., Georgescu Gh., Vişan R., “Acționări pneumatice”, Editura Tehnică, Bucureşti, 1974.
[3] Ionescu, F., “Mecanica fluidelor şi acționări hidraulice şi pneumatice”, Editura Didactică şi Pedagogică, Bucureşti, 1980.
[4] Leonăchescu, N., Termotehnica, Editura Didactică şi Pedagogică, Bucureşti, 1981.
[5] Avram, M., “Acționări hidraulice şi pneumatice, vol I şi II, Editura Printech, Bucureşti, 1999-2000.
[6] Ionescu, E., “Acționări şi automatizări pneumatice”, Editura Universității “Transilvania”, Braşov, 2010.

Acta Universitatis Sapientiae

The scientific journal of Sapientia University publishes original papers and surveys
in several areas of sciences written in English.
Information about each series can be found at
http://www.acta.sapientia.ro.

Acta Universitatis Sapientiae
Electrical and Mechanical Engineering

Sapientia University

Scientia Publishing House

ISSN 2065-5916

http://www.acta.sapientia.ro

Information for authors

Acta Universitatis Sapientiae, Electrical and Mechanical Engineering publishes only original papers and surveys in various fields of Electrical and Mechanical Engineering. All papers are peer-reviewed.

Papers published in current and previous volumes can be found in Portable Document Format (PDF) form at the address: `http://www.acta.sapientia.ro`.

The submitted papers must not be considered to be published by other journals. The corresponding author is responsible to obtain the permission for publication of co-authors and of the authorities of institutes, if needed. The Editorial Board is disclaiming any responsibility.

The paper must be submitted both in MSWord document and PDF format. The submitted PDF document is used as reference. The camera-ready journal is prepared in PDF format by the editors. In order to reduce subsequent changes of aspect to minimum, an accurate formatting is required. The paper should be prepared on A4 paper (210 $\times$ 297 mm) and it must contain an abstract of 200-250 words.

The language of the journal is English. The paper must be prepared in single-column format, not exceeding 12 pages including figures, tables and references.

The template file from http://www.acta.sapientia.ro/acta-emeng/emeng-main.htm may be used for details.

Submission must be made only by e-mail (`acta-emeng@acta.sapientia.ro`).

One issue is offered to each author free of charge. No reprints are available.

Contact address and subscription:
Acta Universitatis Sapientiae, Electrical and Mechanical Engineering
RO 400112 Cluj-Napoca
Str. Matei Corvin nr. 4.
E-mail: acta-emeng@acta.sapientia.ro

Printed by Digital Color Company
www.digitalcolorcompany.ro